

Stony Brook University



OFFICIAL COPY

The official electronic file of this thesis or dissertation is maintained by the University Libraries on behalf of The Graduate School at Stony Brook University.

© All Rights Reserved by Author.

**Search For Gravitons Decaying To Vector Bosons in Hadronic Final States in pp
Collisions at $\sqrt{s} = 8\text{TeV}$ Collected With the ATLAS Detector**

A Dissertation presented

by

Angel Fernando Campoverde Quezada

to

The Graduate School

in Partial Fulfillment of the

Requirements

for the Degree of

Doctor of Philosophy

in

Physics

Stony Brook University

December 2015

Stony Brook University

The Graduate School

Angel Fernando Campoverde Quezada

We, the dissertation committee for the above candidate for the

Doctor of Philosophy degree, hereby recommend

acceptance of this dissertation

Professor Robert McCarthy - Dissertation Advisor
Department of Physics

Professor Jacobus Verbaarschot - Chairperson of Defense
Department of Physics

Professor John Hobbs
Department of Physics

Hooman Davoudiasl
Particle Physicist
Brookhaven National Laboratories

This dissertation is accepted by the Graduate School

Charles Taber
Dean of the Graduate School

Abstract of the Dissertation

**Search For Gravitons Decaying To Vector Bosons in Hadronic Final States in pp
Collisions at $\sqrt{s} = 8\text{TeV}$ Collected With the ATLAS Detector**

by

Angel Fernando Campoverde Quezada

Doctor of Philosophy

in

Physics

Stony Brook University

2015

ATLAS data are used to search for narrow diboson resonances in a dijet final state where each jet is tagged as a boson using jet mass and substructure properties. The data are the 20.3fb^{-1} of pp collisions collected in 2012. A search for $G \rightarrow WW/ZZ$ is performed over the diboson mass range $1.2 < m_{VV} < 3.0\text{TeV}$. The most significant excess is of approximately 2.5σ at around 2TeV. Limits on $\sigma \cdot B$ (the production cross section times branching fraction) for this process are reported as a function of the graviton mass.

Contents

1	Theoretical Framework	2
1.1	Randall Sundrum Model	2
1.1.1	Graviton Modes	4
1.1.2	Localizing SM Fields on the Brane	5
1.2	Extended Gauge Model	6
2	ATLAS Detector	8
2.1	Inner Detector	8
2.1.1	Pixel Detector	8
2.1.2	Semiconductor Tracker	10
2.1.3	Transition Radiation Tracker	10
2.1.4	Track and Vertex Reconstruction	11
2.2	Calorimeter	12
2.2.1	Electromagnetic Calorimeter	12
2.2.2	Hadronic Calorimeter	14
2.3	Muon Spectrometer	19
2.3.1	Monitored Drift Tube Chambers	19
2.3.2	Cathode Strip Chambers	21
2.3.3	Trigger Chambers	21
2.4	Luminosity Measurement	23
2.4.1	LUCID	24
2.4.2	ALFA	25
3	Monte Carlo, Data and Physics Objects	27
3.1	Event Topology	27
3.2	MonteCarlo Samples	28
3.2.1	Graviton Signals	28
3.2.2	Background	28
3.3	Tracks	31
3.4	Jets	31
3.4.1	Split Filtering and Trimming	31
3.5	Systematics	33
3.5.1	Other Sources of Uncertainty	34

3.6	Jet Energy and Mass Calibration	35
4	Event Selection	37
4.1	Event Topology Cuts	37
4.2	Boson Tagging	39
4.2.1	Momentum Balance	40
4.2.2	Ungroomed Jet's Number of Tracks	40
4.2.3	Uncertainty on the efficiency of the cut on the ungroomed jet's number of tracks	41
4.2.4	Filtered Jet's Mass	42
4.3	Event Selection Summary	45
5	Statistical Analysis	47
5.1	Background Estimate	47
5.2	Signal Hypothesis	47
5.3	Dijet Mass Distribution	48
5.4	Model	50
5.5	Limits and p_0	50
5.5.1	Look Elsewhere Effect (LEE)	52
6	Electromagnetic Calibration	54
6.1	Introduction	54
6.2	Calibration Constants	54
6.3	Study of the Calibration Constants in the Barrel	56
6.3.1	Software Related Problems	56
6.3.2	Hardware Related Problems	57
6.4	Study of the Calibration Constants in the End Cap	63
6.5	Search for Outliers	66
6.5.1	Method	66
6.5.2	Results	67
7	Conclusions	70
7.1	Graviton Search	70
7.2	Study of the Calibration Constants of the Electromagnetic Calorimeter's Cells	71
	Bibliography	72
A	Monte Carlo, Data and Physics Objects	75
A.1	Background	75
A.2	Signal	76
B	Event Selection	78
B.1	Filtered Jet Mass Cut Optimization	78

List of Figures

2.1	View of the Inner detector in the $R - z$ plane.	9
2.2	Side view of the pixel detector, End-Cap and Barrel.	9
2.3	SCT module	10
2.4	The figure shows the position of the active and passive materials in the EM calorimeter.	13
2.5	In (a) is shown a module and the barrel once they are all assembled. In (b) one side of the Tile Calorimeter after different tiles have been associated to different channels. In (c) three fibers seen inside the channel, while one is outside and in front of the scintillating tile.	15
2.6	Above (a) shows the arrangement of the absorber plates and the electrodes in the HEC, (b) shows a HEC module and the seven rods used to keep the plates in place.	17
2.7	In the figure above (a) shows the FCal split into its three modules and placed in the cryostat, (b) shows a view in the (x, y) plane of the detector cells.	19
2.8	In the figure above (a) shows the different components of the MS in the bending $(z - R)$ plane. (b) Shows an MDT chamber with its support structure.	20
2.9	The figure shows a resistive plate chamber made of two units.	22
2.10	At the left is a thin gap chamber with three gas chambers, at the right one with two.	23
2.11	(a) shows a cross section of the Roman pot configuration in ALFA. At the right is the detector in a working position, at about 1mm of the beam. At the left the same detector retracted. (b) shows the geometry of the scintillating fibers.	26
3.1	Theoretical prediction of the branching ratio of a WW , WZ and ZZ pair, to fully hadronic, semi-hadronic and fully leptonic final states.	27
3.2	Dijet Mass distributions for both $G \rightarrow WW$ and $G \rightarrow ZZ$ for three different mass points at truth level and after simulation.	29
3.3	In (a) the p_T distribution of the leading jet before re-weighting and in (b) after it.	30
3.4	Different background components compared with data.	30
3.5	Jet grooming and filtering.	32
3.6	34
3.7	(a) shows the energy response for different p_T slices in PYTHIA. (b) shows the same distributions after calibration. (c) and (d) show the same distributions but for the mass response.	36

4.1	Comparison of the distributions of different quantities between data and simulation. The signal was normalized in such a way that the peak of the histogram agrees with the data. The background was fitted to the data.	38
4.2	39
4.3	Comparison of the optimal cut in Δy_{JJ} for a $G \rightarrow WW/ZZ$ and a $W' \rightarrow WZ$ signals.	40
4.4	Distribution of the momentum balance for QCD background and graviton signal.	40
4.5	Figure (a) shows the distribution of the number of tracks associated to the un-groomed jets for a Graviton signal with $m_G = 2\text{TeV}$. Figure (b) shows the same distribution but comparing only QCD background.	41
4.6	Figure (a) shows the fit of the $V + jets$ distribution in data to a Crystal Ball plus third polynomial PDF, (b) shows the same fit but with a fourth degree polynomial PDF.	42
4.7	PDF describing the efficiency of the n_{trk} cut for the BKG3 and BKG4 background parametrizations. Their combination is shown in red.	43
4.8	Figure (a) shows the mass distributions for W jets, Z jets and QCD jets. In (b) the graviton mass distribution is fitted to a Breit-Wigner PDF in order to determine the events that will go into the distribution in (c). From (c) will be obtained the values of the p_T slices used for the mass window optimization.	44
4.9	The figure shows the jet mass distributions for a $G \rightarrow WW$ with $m_G = 2200\text{GeV}$ before and after the systematics were applied.	44
4.10	Figure (a) shows the background yield for many combinations of the higher and lower edge of the mass window. (b) shows the same but for the signal yield. Using (a) and (b) the significance is obtained for each point in (c). Figure (d) shows how the signal and background yields and the significance behave with different half widths and placing the center of the window at the mass of the W boson.	45
4.11	In (a) is shown the efficiency related to the event topology cuts for both a $W' \rightarrow WZ$, a $G \rightarrow WW$ and a $G \rightarrow ZZ$ signal and for different mass points. Figure (b) shows the efficiency after the boson tagging cuts are additionally applied.	46
5.1	Figure (a) shows the background estimate in blue, the data in black and three different W' signal hypotheses in red, yellow and green. Figures (b) and (c) contain the same information but after applying the WW and ZZ selection cuts with $G \rightarrow WW$ and $G \rightarrow ZZ$ signal hypotheses respectively.	49
5.2	51
5.3	53
6.1	Diagram of a LAr calorimeter cell. RLC circuit that models the detector cell, followed by a transmission line, an amplifier (triangle) and a shaper (rectangle).	55
6.2	$M_{\text{phys}}/M_{\text{cal}}$ distribution in function of η in the front layer of the LAr barrel. The seven slots of the front layer (from 2 to 8) can be clearly distinguished.	57
6.3	Values of various calibration constants for the front layer of the Side A of the Barrel of the LAr calorimeter	58

6.4	$Q^2(\omega)$ corresponding to many T_{tail} values (see (6.7)), increasing in steps of 20ns from 150ns, for $t_{start} = 20ns$ and where the uppermost curve corresponds to a sum with $t_{end} = 750ns$.	59
6.5	$Q^2(\omega)$ from slot 2 (a) to slot 6 (f) for Feedthrough=11 and $\phi = 2.3$ radians.	60
6.6	$Q^2(\omega)$ showing many minima.	61
6.7	Distributions of ω_0	61
6.8	Distributions of M_{phys}/M_{cal}	62
6.9	Distribution of M_{phys}/M_{cal} before and after the corrections are applied in function of η .	63
6.10	In (a) $Q^2(\omega)$ for channels in $2 < \eta < 2.4$, in the front layer of the End Cap. In (b) $Q^2(\omega)$ for channels in $1.4 < \eta < 2.5$ in the back layer of the End Cap.	64
6.11	In (a) old and new values (setting $\omega_0 = 0.27GHz$) for M_{phys}/M_{cal} for the front layer of the End Cap, Side A. In (b) the same values for the back layer	64
6.12	In (a) $Q^2(\omega)$ curves for the middle layer of the side A of the End Cap. In (b) Comparison of default and modified values of M_{phys}/M_{cal} in the same part of the detector.	65
6.13	Ratio of M_{phys}/M_{cal} between the front and middle layer. The subscript $1/2$ is used to symbolize the ratio between the quantities in layer 1 and layer 2.	65
6.14	Representation of real outliers and channels within 2σ .	66
6.15	The black and the blue squares represent outliers in two different campaigns, the red channels are their intersection.	67
6.16	Intersection of outliers for 13 campaigns in the Barrel in (a) and in the End Cap in (b) fitted to a superposition of two exponentials.	68
6.17	Plots of outlier cells in a given calibration constant.	69
B.1	(a), (b) show the background and signal efficiencies as well as the gain in significance with respect to the $60 < m_{JJ} < 110GeV$ mass window for the 1.8TeV and 2.2TeV W' mass points.	79
C.1	Figures (a) and (b) show the ω_0 distributions for the side A of the barrel for low gain, before and after the correction respectively. Figures (c) and (d) show the corresponding distributions for M_{phys}/M_{cal} .	81
C.2	Figures (a) and (b) show the ω_0 distributions for the side A of the barrel for medium gain, before and after the correction respectively. Figures (c) and (d) show the corresponding distributions for M_{phys}/M_{cal} .	82

List of Tables

2.1	Tracking accuracy in the Barrel and End-Cap for the different parts of the Inner Detector.	8
3.1	Cuts applied to data and MC before optimization studies.	30
3.2	Different parameters used to build and groom the jets used here.	33
3.3	Systematics on the scales and resolutions of the jet's p_T , mass and momentum balance.	33
3.4	Additional systematics associated to the luminosity, generator settings and the efficiency on the n_{trk} cut.	35
4.1	Event Selection Summary	46
5.1	Impact of different sources of systematics on the signal normalization uncertainty.	48
A.1	Cross-sections of different p_T slices for the PYTHIA dijet QCD MC.	75
A.2	Cross-sections of different p_T slices for the POWHEG dijet QCD MC.	75
A.3	Cross-sections of different p_T slices for the PYTHIA $W + jets$ and $Z + jets$ samples.	76
A.4	Cross-sections times branching ratios and widths for different mass points for a graviton decaying in the WW and ZZ channels.	77
B.1	Cross-sections of different p_T slices for the PYTHIA $W + jets$ MC.	78
B.2	Optimal values for the half window size for a vector boson, deduced from many W' signal samples.	79

Chapter 1

Theoretical Framework

The large gap between the Electroweak scale (10^2GeV) and the Planck scale (10^{18}GeV) known as the hierarchy problem, is one of the main motivations for the formulation of many physical models postulating the existence of extra spatial dimensions. However the size of any extra spatial dimension is constrained by measurements of the gravitational and electroweak interactions. The constraints set by the latter measurements[1] are much more stringent than the former ones [2]. If the extra dimensions are large, then we must assume that gravity is the only force that can live in the extra dimension and the other forces can only propagate in our 4D spacetime. This can allow the possibility that the real Planck scale in the $4 + n$ dimensional space can be of the order of the electroweak interactions and the apparent weakness of the gravitational interactions is due to the fact that gravity is able to probe these extra dimensions and therefore it *dilutes* while the other SM interactions cannot escape the 4 dimensional space-time [3].

1.1 Randall Sundrum Model

An alternative to the large extra dimensions scenario is the Randall Sundrum Model (RS), which postulates the existence of a single extra compactified dimension. This dimension can be parametrized as a circumference whose opposite points are identified. In this theory the extra dimension does not have to be large because gravity is not attenuated by the size of the new dimension but by a *warp factor*.

In what follows a brief summary of the original paper that proposes an extra warped dimension [4] is given. Assuming that the extra dimension is compactified and that the angle ϕ parametrizes it, one can write the action as (1.1)

$$\begin{aligned}
S &= S_{grav} + S_{vis} + S_{hid} \\
S_{grav} &= \int d^4x \int_{-\pi}^{\pi} d\phi \sqrt{-G} (-\Lambda + 2M^3 R) \\
S_{vis} &= \int d^4x \sqrt{-g_{vis}} (\mathcal{L}_{vis} - V_{vis}) \\
S_{hid} &= \int d^4x \sqrt{-g_{hid}} (\mathcal{L}_{hid} - V_{hid})
\end{aligned} \tag{1.1}$$

where R and M are the Ricci scalar and Planck scale in 5D respectively, V_{hid} and V_{vis} are the vacuum energy densities in each brane (i.e. their cosmological constants) and:

$$\begin{aligned}
g_{\mu\nu}^{vis}(x^\mu) &\equiv G_{\mu\nu}(x^\mu, \phi = \pi) \\
g_{\mu\nu}^{hid}(x^\mu) &\equiv G_{\mu\nu}(x^\mu, \phi = 0)
\end{aligned}$$

Plugging this action into the 5D Einstein equations one gets (1.2).

$$\begin{aligned}
\sqrt{-G}(R_{MN} - \frac{1}{2}G_{MN}R) &= -\frac{1}{4M^3} [\Lambda \sqrt{-G} G_{MN} + V_{vis} \sqrt{-g_{vis}} g_{\mu\nu}^{vis} \delta_M^\mu \delta_N^\nu \delta(\phi - \pi) \\
&+ V_{hid} \sqrt{-g_{hid}} g_{\mu\nu}^{hid} \delta_N^\nu \delta(\phi)]
\end{aligned} \tag{1.2}$$

The non-factorizable metric (1.3) respects Poincare invariance in four dimensions, can be consistent with the $\phi \rightarrow -\phi$ symmetry and can therefore be used as an ansatz to solve (1.2).

$$ds^2 = e^{-2\sigma(\phi)} \eta_{\mu\nu} dx^\mu dx^\nu + r_c^2 d\phi^2 \tag{1.3}$$

By replacing this metric into (1.2) one gets (1.4)

$$\frac{6\sigma'^2}{r_c^2} = \frac{-\Lambda}{4M^3} \tag{1.4}$$

$$\frac{3\sigma''}{r_c^2} = \frac{V_{hid}}{4M^3 r_c} \delta(\phi) + \frac{V_{vis}}{4M^3 r_c} \delta(\phi - \pi) \tag{1.5}$$

from which one can solve for σ and get (1.6)

$$\sigma = r_c |\phi| \sqrt{\frac{-\Lambda}{24M^3}}, \quad k = \sqrt{\frac{-\Lambda}{24M^3}} \tag{1.6}$$

which is consistent with the $\phi \rightarrow -\phi$ symmetry and also implies that in the bulk the cosmological constant has to be negative, unlike on our 3D brane. From this (1.5) gives (1.7) and (1.8)

$$\sigma'' = 2r_c \sqrt{\frac{-\Lambda}{24M^3}} [\delta(\phi) - \delta(\phi - \pi)] \tag{1.7}$$

$$V_{hid} = -V_{vis} = 24M^3 k \tag{1.8}$$

If one fluctuates the metric (1.3) around the vacuum as in (1.9)

$$ds^2 = e^{-2kT(x)|x|} [\eta_{\mu\nu} + \bar{h}_{\mu\nu}(x)] dx^\mu dx^\nu + T^2(x) d\phi^2 \quad (1.9)$$

one obtains two fields, the lowest Kaluza-Klein (KK) excitation of the graviton, $\bar{h}_{\mu\nu}(x)$, and a scalar field $T(x)$ that represents the fluctuations of the distance between the TeV and Planck branes, also known as Radion, whose vacuum expectation value (VEV) is r_c . By introducing this metric into S_{grav} in (1.1) one gets (1.10).

$$M_{Pl}^2 = M^3 r_c \int_{-\pi}^{\pi} d\phi e^{-2kr_c|\phi|} = \frac{M^3}{k} [1 - e^{-2kr_c\pi}] \quad (1.10)$$

Given the metric of the Planck brane $g_{hid} = \bar{g}_{\mu\nu}$ one can write the metric of the TeV brane as $g_{\mu\nu}^{vis} = e^{-2kr_c\pi} \bar{g}_{\mu\nu}$. Taking the part of the action in the TeV brane corresponding to the Higgs sector (term in the Lagrangian involving the Higgs field) and putting all in function of \bar{g} :

$$S_{Higgs} = \int d^4x \sqrt{-\bar{g}} e^{-4kr_c\pi} [\bar{g}^{\mu\nu} e^{2kr_c\pi} D_\mu H^\dagger D_\nu H - \lambda (|H|^2 - v_0^2)^2] \quad (1.11)$$

Changing the normalization of the Higgs field as $H \rightarrow e^{-kr_c\pi} H$ one gets (1.12)

$$S_{Higgs} = \int d^4x \sqrt{-\bar{g}} [\bar{g}^{\mu\nu} D_\mu H^\dagger D_\nu H - \lambda (|H|^2 - e^{-2kr_c\pi} v_0^2)^2] \quad (1.12)$$

which implies $v \equiv e^{-kr_c\pi} v_0$ and given that all the particle masses are proportional to the Higgs VEV one gets (1.13)

$$m \equiv e^{-kr_c\pi} m_0 \quad (1.13)$$

which means that particle masses at TeV scales in our visible brane would correspond to masses close to the Planck scale on the Planck brane for an appropriate value of kr_c .

1.1.1 Graviton Modes

A study of the graviton modes is performed in [5] and in this section we briefly expose it. If we perturb the 4D part of the metric tensor as in (1.14)

$$G_{\mu,\nu} = e^{-2\sigma} (\eta_{\mu\nu} + \kappa^* h_{\mu\nu}) \quad (1.14)$$

and then one plugs this metric tensor in the Einstein equations, takes only the 4D components, keeps first order terms in κ^* and uses both the gauge in which $\partial^\mu h_{\mu\nu} = h_{\mu}^{\mu} = 0$ and the expansion (1.15) of the field h

$$h_{\mu\nu}(x, \phi) = \sum_{n=0}^{\infty} h_{\mu\nu}^{(n)}(x) \frac{\chi^{(n)}(\phi)}{\sqrt{r_c}} \quad (1.15)$$

one gets for the n^{th} graviton mode the wave equations (1.16) and (1.17)

$$(\eta^{\mu\nu}\partial_\mu\partial_\nu - m_n^2)h_{\mu\nu}^{(n)}(x) = 0 \quad (1.16)$$

$$\frac{-1}{r_c^2} \frac{d}{d\phi} \left(e^{-4\sigma} \frac{d\chi^{(n)}}{d\phi} \right) = m_n^2 e^{-2\sigma} \chi^{(n)} \quad (1.17)$$

From which $\int_{-\pi}^{\pi} d\phi e^{-2\sigma} \chi^m \chi^n = \delta_{mn}$ follows. The solution of (1.17) is given by:

$$\chi^n(\phi) = \frac{e^{2\sigma}}{N_n} [J_2(z_n) + \alpha_n Y_2(z_n)] \quad (1.18)$$

where J_2 and Y_2 represent the Bessel functions of the first and the second kind respectively and $z_n = m_n e^\sigma / k$. Given that in the ϕ direction we have the $\phi \rightarrow -\phi$ symmetry and asking for $\chi^n(\phi)$ to be continuous at $\phi = 0$ and $\phi = \pi$ we can use $\partial_\phi \chi^n(\phi) = 0$ to get (1.19)

$$\alpha_n \approx x_n^2 e^{-2kr_c\pi} J_1(x_n) = 0 \quad (1.19)$$

where $x_n = z_n(\phi = \pi)$. The second identity tells us the values of the masses of the n^{th} KK state of the graviton, the first one implies that the term with the second kind Bessel function is negligible.

1.1.2 Localizing SM Fields on the Brane

The original RS model assumes that all the SM fields lie on the IR brane, defined as the brane at $\phi = \pi$. However this leads to predictions in which flavor changing neutral currents (FCNC) are significantly larger than observed via electroweak precision tests. In [6] a way to solve this problem is developed and in this section we will briefly discuss it.

A way to solve this problem is to localize some of the SM fields close to the Planck brane and identify the SM fields with the zero modes of the higher dimensional fields. The first and second generation of fermions are placed near the Planck brane, while the Higgs sector and the top quark are placed near the IR brane. This should suppress the operators responsible for the predicted FCNC in the original model. Furthermore there should be a strong suppression of the Yukawa couplings between the Higgs sector and the first two generation of fermions while the Yukawa coupling to the top quark would not be suppressed strongly thus allowing the top quark to acquire a large mass. The gluon coupling to KK gravitons is also suppressed but only by a factor $\approx \log(\hat{M}_p/\text{TeV})$, where \hat{M}_p is the reduced Planck mass, which makes possible graviton production through gluon fusion at the LHC.

All this implies that the only particles with a significant coupling to the graviton are the Higgs boson and the top quark. However the longitudinal components of the W and Z bosons originate from one of the degrees of freedom of the Higgs field. Therefore the branching ratios of the graviton's KK modes to W_L and Z_L are comparable to the branching ratios to the Higgs boson. This is shown in (1.20)-(1.23), where $N_c = 3$ is the number of colors.

$$\Gamma(G \rightarrow t_R t_R^-) \approx N_c \frac{(cx_n^G)^2 m_n^G}{320\pi} \quad (1.20)$$

$$\Gamma(G \rightarrow hh) \approx \frac{(cx_n^G)^2 m_n^G}{960\pi} \quad (1.21)$$

$$\Gamma(G \rightarrow W_L^+ W_L^-) \approx \frac{(cx_n^G)^2 m_n^G}{480\pi} \quad (1.22)$$

$$\Gamma(G \rightarrow Z_L Z_L) \approx \frac{(cx_n^G)^2 m_n^G}{960\pi} \quad (1.23)$$

In general the m^{th} and n^{th} modes of a bulk field couple to the q^{th} mode of the graviton field as in (1.24), where F symbolizes the bulk field and G the graviton field, $T_{\mu\nu}^{m,n}$ is the energy-momentum tensor and $h_{\alpha,\beta}^q$ is the q^{th} mode of the graviton field. When the bulk field is a gluon one has (1.25) for the coupling of the zeroth mode of the gluon field to the n^{th} mode of the graviton field.

$$\mathcal{L}_G = \sum_{m,n,q} C_{mnq}^{FFG} \frac{1}{M_P} \eta^{\mu\alpha} \eta^{\nu\beta} h_{\alpha,\beta}^{(q)}(x) T_{\mu,\nu}^{(m,n)}(x) \quad (1.24)$$

$$C_{00n}^{AAG} = e^{k\pi R} \frac{2[1 - J_0(x_n^G)]}{k\pi R (x_n^G)^2 |J_2(x_n^G)|} \quad (1.25)$$

1.2 Extended Gauge Model

Heavy resonances decaying into a WZ or WW pair can include heavier versions of the SM W or Z bosons, called W' and Z' bosons respectively [7]. Their couplings to a WZ or WW pair are assumed to have a similar form to the couplings of the SM W and Z bosons, and are given by (1.26). The corresponding partial widths are given by (1.27) and (1.28). Equations (1.29) and (1.30) show the partial widths for the decay to fermions from a W' and a Z' respectively, where θ_w is the Weinberg angle, N_c is the number of colors (1 for leptons and 3 for quarks) and Q_f is the fermion charge.

$$V_{Z'W^-W^+} = V_{W'^{\pm}W^{\pm}Z} = ie \cot \theta_w [g_{\mu\nu}(q-p)_\lambda + g_{\mu\lambda}(p-r)_\nu + g_{\nu\lambda}(r-q)_\mu] \quad (1.26)$$

$$\Gamma(W'^{\pm} \rightarrow ZW^{\pm}) = \frac{\alpha}{48} \cot^2 \theta_w M_{W'^{\pm}} \frac{M_{W'^{\pm}}^4}{M_Z^2 M_W^2} \left[\left(1 - \frac{M_Z^2 - M_W^2}{M_{W'^{\pm}}^2} \right)^2 - 4 \frac{M_W^2}{M_{W'^{\pm}}^2} \right]^{3/2} \cdot \left[1 + 10 \left(\frac{M_W^2 + M_Z^2}{M_{W'^{\pm}}^2} \right) + \frac{M_W^4 + M_Z^4 + 10M_W^2 M_Z^2}{M_{W'^{\pm}}^4} \right] \quad (1.27)$$

$$\Gamma(Z' \rightarrow W^+W^-) = \frac{\alpha}{48} \cot^2 \theta_w M_{Z'} \left(\frac{M_{Z'}}{M_W} \right)^4 \cdot \left(1 - 4 \frac{M_W^2}{M_{Z'}^2} \right)^{3/2} \cdot \left[1 + 20 \left(\frac{M_W}{M_{Z'}} \right)^2 + 12 \left(\frac{M_W}{M_{Z'}} \right)^4 \right] \quad (1.28)$$

$$\Gamma(W'^{\pm} \rightarrow f\bar{f}') = \frac{\alpha}{12} N_c \frac{M_{W'^{\pm}}}{\sin^2 \theta_w} \quad (1.29)$$

$$\Gamma(Z' \rightarrow f\bar{f}') = \frac{\alpha}{48} N_c \frac{M_{Z'}}{\sin^2 \theta_w \cos^2 \theta_w} \left[1 + \left(1 - 4|Q_f| \sin^2 \theta_w \right) \right] \quad (1.30)$$

For a W' or a Z' with a mass of $\approx 1\text{TeV}$ most of the terms in (1.28) and (1.27) are negligible. Therefore the partial widths to a pair of bosons become proportional to $M_{W'/Z'}^5$ while the widths to fermions remain linear in $M_{W'/Z'}$. Given that the branching ratio is the partial width over the total width, the branching ratio of W'/Z' to vector bosons should increase with $M_{W'/Z'}$ as the one to fermions decreases. This implies that for large enough W'/Z' masses the decay should be detected mostly in the WZ/WW channels. On the other hand for large enough masses the width will be comparable to the mass and the peak structure of the signal will not be visible anymore, degrading the search sensitivity.

Reference [8] proposes an Extended Gauge Model (EGM) which assumes that the coupling of the W'/Z' resonance is suppressed by (1.31) where the constant of proportionality c is usually taken as one.

$$\xi = c \left(\frac{M_W^2}{M_{W'/Z'}^2} \right) \quad (1.31)$$

This factor makes the width scale linearly with the mass. This suppression also is responsible for keeping the branching ratios roughly constant, in contrast to the reference model where the WZ and WW channels were dominant at higher masses.

Chapter 2

ATLAS Detector

2.1 Inner Detector

The inner detector (ID) is divided into three parts. The innermost part of the detector is the pixel detector, composed of three layers of semiconductor material and electronics. These layers are aimed to detect charged particles as *hits* on the semiconductor. Surrounding the pixel detector is the SCT (Semiconductor Tracker) composed of four layers in the barrel and nine in the End-Cap, whose purpose is to measure the trajectories of charged particles in the $R - \phi$ plane (perpendicular to the beam pipe). Both the pixel detector and the SCT cover the region $|\eta| < 2.5$. The outermost region of the inner detector contains the TRT (Transition Radiation Tracker), which also tracks the trajectories of charged particles, but with a different technology. The inner detector in the $R - z$ plane is illustrated in figure 2.1. The accuracies with which the three parts of the inner detector measure tracks are shown in table 2.1.

Detector	Barrel (μm)	End-Cap (μm)
Pixel	$10(R - \phi), 115(z)$	$10(R - \phi), 115(R)$
SCT	$17(R - \phi), 580(z)$	$17(R - \phi), 580(R)$
TRT	$130(R - \phi)$	$130(R - \phi)$

Table 2.1: Tracking accuracy in the Barrel and End-Cap for the different parts of the Inner Detector.

2.1.1 Pixel Detector

The pixel detector is made of 1744 modules, which are mounted on staves in the barrel and on disks in the End-Cap. In the barrel the modules form three layers arranged as concentric cylinders and in the End-Cap they form three wheels. Each wheel is made of eight sectors each with three modules mounted in the outer side and three in the inner side, as shown in figure 2.2.

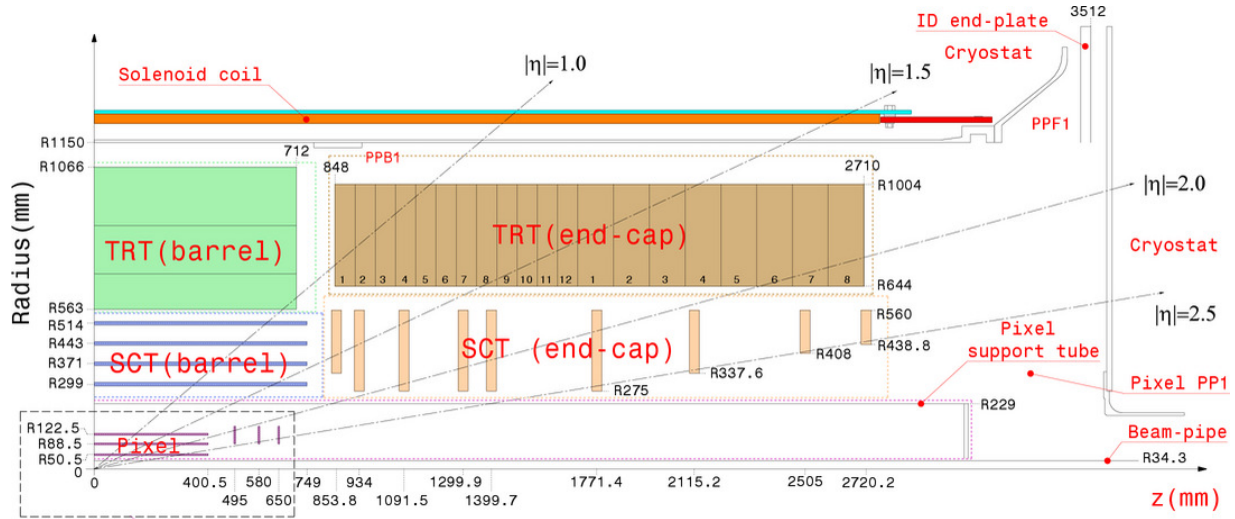


Figure 2.1: View of the Inner detector in the $R - z$ plane.

Each module in the pixel detector is composed of three layers. The first layer, facing away from the interaction point contains 16 chips with a thickness of $180\mu\text{m}$ and each containing 2880 channels. In front of this layer is the silicon tile which measures $63.4 \times 24.4\text{mm}^2$ in area and with a thickness of $250\mu\text{m}$. The layer with chips and the silicon are connected through bump bonds made of In or PbSn. Finally, facing the interaction point is a polyimide¹ printed circuit board which is attached to a polyimide pig-tail.

Each pixel sensor measures $63 \times 19\text{mm}^2$, and operates with a bias voltage of between 150V-600V depending on the radiation damage. About 90% of the pixels in the pixel detector measure $50 \times 400\mu\text{m}^2$, and there are 46080 of them.

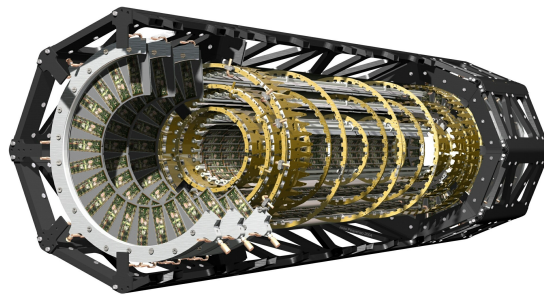


Figure 2.2: Side view of the pixel detector, End-Cap and Barrel.

The pixel modules are approximately flat, so they define a plane. The modules are positioned with respect to this plane with a precision of $1 - 2\mu\text{m}$ and with a precision of $\approx 10\mu\text{m}$ perpendicular to it. In beam tests the spatial resolution of the pixel detector at normal incidence has been measured as $12\mu\text{m}$, 80% of the tracks have a single pixel hit and the resolution is not significantly degraded after irradiation.

¹ Polyimide is a heat resistant polymer

2.1.2 Semiconductor Tracker

The SCT is made of four layers in the barrel and nine wheels in the End-Cap. They cover the pseudo-rapidity $|\eta| < 2.5$ and provide two hits per layer. Each module is made of four wafers each one is made of 768 readout strips of about 6cm in length, and $285 \pm 15\mu\text{m}$ in thickness. The strips of two of them are aligned in the beam (radial) direction for the Barrel (End-Cap). The arrangement of the strips provides a very precise measurement of the hit location in the $R - \phi$ plane. Both wafers are rotated with respect to each other by an angle of 40mrad which allows the measurement of the $z(R)$ coordinate in the Barrel (End-Cap). The inner detector contains 4088 modules which are mounted on carbon-fibre cylinders.

Initially the bias voltage applied to the SCT sensors was $\approx 150\text{V}$ but after 10 years the voltage should be raised to between 250V and 350V to ensure their correct performance. An SCT module can be seen in figure 2.3

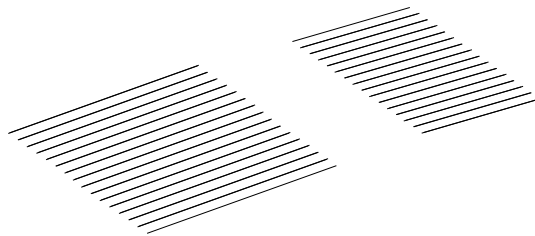


Figure 2.3: SCT module

2.1.3 Transition Radiation Tracker

The TRT is made of a set of polyimide tubes of 4mm of diameter, also called straws. These tubes are filled with a mixture of Xe (70%), CO_2 (27%) and O_2 (3%) at an over pressure of between 5 and 10 mbar. The tubes act as cathodes and at the center is located a cable, the anode, with a diameter of $31\mu\text{m}$ and an active length of 71.2cm ($\approx 37\text{cm}$) in the Barrel (End-Cap); they are read on both ends (outer radius) and kept at ground potential. They have a resistance of $60\Omega/\text{m}$, the cathode is operated at around -1530V , which gives a gain of 2.5×10^4 . The straws are spaced by $\approx 7\text{mm}$ and are surrounded by polypropylene which acts as the transition radiation material.

The TRT straws are aligned parallel to the beam axis (Radially) and have a length of 144cm (37cm) in the Barrel (End-Cap), therefore the barrel only provides information about the location of the particle in $R - \phi$. There are up to 73 (160) layers of straws in the Barrel (End-Cap). A charged particle with $p_T > 0.5\text{GeV}$ and $|\eta| < 2.0$ should cross at least 36 straws, except in the transition region where the number of crossed straws falls to 22.

The straws are inserted in a matrix of polypropylene. The gas mixture inside the straws is recirculated and monitored to ensure stable operation. CO_2 is also recirculated between the matrix and the straw in order to avoid pollution from leaks of Xenon, which would lead to transition radiation being absorbed by the gas outside the straws. A filter is in charge of removing organo-silicone impurities from the gas mixture, which should be kept at low levels. The filter also removes the ozone produced during gas amplification.

2.1.4 Track and Vertex Reconstruction

The tracks are reconstructed from the hits in the pixel detector, SCT or in the TRT. In the TRT the amount of transition radiation emitted as the particle goes from Xenon to polypropylene is inversely proportional to its mass. This transition radiation is absorbed by the Xenon and increases the level of ionization. Therefore there is a lower (250eV) and a higher (6KeV) threshold used when measuring hits. For electrons with energies above 2GeV one expects between seven to ten high-threshold hits; more massive particles should leave less. Thus the TRT can be used for electron identification. The hits in the TRT can be measured with a lower accuracy than the ones in the Inner Detector but the number is larger, therefore improving the overall precision in the reconstruction of the tracks.

An inside-out algorithm is used to reconstruct tracks of primary charged particles², starting from three hits in the silicon detectors, adding more hits farther from the interaction point. The tracks are required to have a $p_T > 400\text{MeV}$. On the other hand to reconstruct tracks from secondary charged particles a track is built from hits in the TRT and extended towards the silicon detector using its hits, an outside-in algorithm. A reconstructed track is required to have at least 9 hits in the silicon detector and zero holes³ in the pixel detector.

The vertex is found through the following steps [9].

- By taking the distribution of the z coordinate of the tracks at their closest approach to the beam line the seed of the primary vertex is defined as the place where this distribution reaches its global maximum.
- A fit based on a χ^2 algorithm is used to find the vertex's position.
- All the tracks that are farther than 7σ from the primary vertex are used to build other vertices.
- The algorithm stops when there are no more unassociated tracks or no more vertices can be found.

The algorithm used to find the vertex's position is based on building $L(v)$ as defined in (2.1) [10]. Where for each term d_i is the distance between the vertex v and the i^{th} track, and σ_i , is its error. Each term is weighted by (2.2), where $\chi_i = d_i/\sigma_i$, χ_c is a constant such that $w_i = 0.5$

²Particles with a life time greater than $3 \times 10^{-11}\text{s}$ produced in the pp interaction or from the decays of particles with a lifetime greater than $3 \times 10^{-11}\text{s}$.

³A place in the detector where a track should correspond to a hit but there is no hit registered.

for track-vertex pairs for which $\chi_i = \chi_c$. T controls the degree in which the weights of the w_i varies between tracks with low χ_i and tracks with high χ_i . $T \rightarrow \infty$ implies that all the weights are one half, while $T \rightarrow 0$ means that all the tracks would have a weight of zero or one for $\chi_i > \chi_c$ or $\chi_i < \chi_c$ respectively. This constant is used during the minimization, which uses an annealing based algorithm.

$$L(v) = \frac{1}{2} \sum_{i=1}^n \chi_i^2(v) = \frac{1}{2} \sum_{i=1}^n \frac{d_i^2(v)}{\sigma_i^2} \quad (2.1)$$

$$w_i(\chi_i^2) = \frac{e^{-\chi_i^2/2T}}{e^{-\chi_i^2/2T} + e^{-\chi_c^2/2T}} \quad (2.2)$$

2.2 Calorimeter

ATLAS has a sampling⁴ calorimeter which has symmetry and full coverage along ϕ . It measures the energies of electrons and photons mainly with the Electromagnetic Calorimeter. The energy of the hadrons is measured with the Tile Calorimeter for central objects and for higher rapidities with the Extended Tile, Hadronic End Cap and Forward Calorimeter.

The Barrel is housed in a central cryostat. There are two extra cryostats, each of them holding one side of the End-Cap, the Hadronic End-Cap and the Forward Calorimeter. The cryostat consists of two toroidal, concentric aluminum vessels, the inner one is at a bit below 90K and the outer one is warm, there is vacuum between them. In the vacuum of the Barrel cryostat is housed a solenoid that generates the magnetic field for the ID.

2.2.1 Electromagnetic Calorimeter

The electromagnetic calorimeter is split into a Barrel ($|\eta| < 1.475$) and two End-Caps ($1.375|\eta| < 3.2$). Its precision region occupies the pseudorapidity $|\eta| < 2.5$ excluding the transition region between the Barrel and End-Cap. The Barrel is divided into two halves at $z = 0$ and each side has a length of 3.2m.

The detector uses lead as passive material and Liquid Argon (LAr) as active material. LAr was chosen because of its stable response in time, its radiation hardness and its linear behavior. Two 0.2mm stainless steel sheets are glued on each side of the lead absorber to provide it mechanical strength. The signal induced by the passage of a particle is collected through a system of three copper electrodes located between the lead absorbers, the central one is kept at ground potential and the external ones are kept at a 2000V, they are separated by two polyimide sheets. The gap between the readout electrodes and the absorbers is kept by honeycomb spacers and filled with LAr. The gap's width is about 2mm and the associated drift time is 450ns. All these components are arranged in an accordion geometry with the folds going in the z direction for the Barrel and the radial direction for the End-Cap. The geometry of a cell is shown in figure 2.4.

⁴The active and passive medium are different.

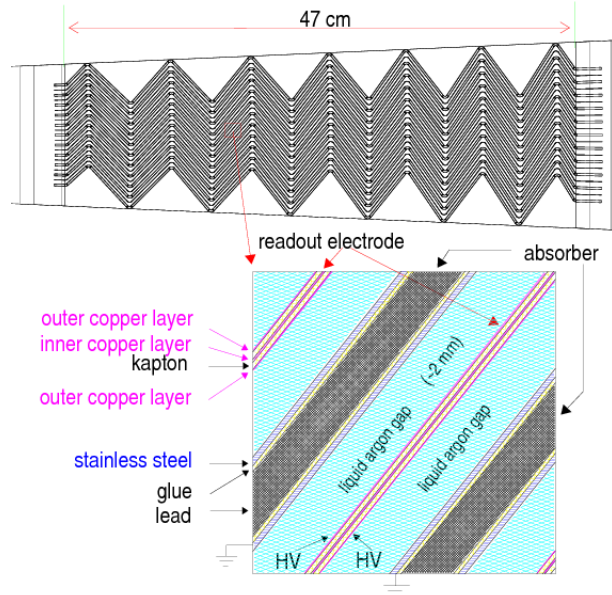


Figure 2.4: The figure shows the position of the active and passive materials in the EM calorimeter.

The Electromagnetic Calorimeter, up to $|\eta| = 2.5$, is divided in three layers and additionally a presampler up to $|\eta| < 1.8$. In the range $2.5 < |\eta| < 3.2$ there are only two layers. The front and middle layer have a high granularity in $|\eta|$ and are used to measure the direction of electrons and photons with high precision, the second layer additionally absorbs most of the particle's energy. The back layer has a more coarse granularity and absorbs the remaining of the electromagnetic shower. The presampler is an 11mm (4mm) thick layer in front of the first layer in the Barrel (End-Cap), and its task is to measure the energy lost by photons and electrons on dead material (cables, cryostat walls ...) before they enter the calorimeter by using their shower multiplicity. Given that hadrons are less susceptible to the material, the presampler can be also used to discriminate between electrons and hadrons.

In the Barrel and the End-Cap the folding angles vary with the radius. However for technical reasons the angle has to be kept between 60° and 120° which limits the radius of the End-Cap's outer wheel. Therefore to reach higher pseudorapidities an inner wheel has to be added, they join at $|\eta| = 2.5$ and there is a crack of about 3mm between them. The variation of the value of the folding angle keeps the gap between the absorbers constant in the Barrel but not in the End-Cap. In the Barrel the front layer is read out in the low radius side of the electrode while the medium and back layers are read at the high radius side. In the End-Cap's outer wheel the signals are read from both front and back sides and in the inner wheel, due to higher radiation levels, the signals are read from the back side.

2.2.2 Hadronic Calorimeter

The energy of the hadrons is measured with the Tile Calorimeter, the Hadronic End-Cap (HEC) and the Forward Calorimeter (FCal). The tile calorimeter covers $0 < |\eta| < 1.7$ and together with the HEC and FCal, they reach $|\eta| < 4.9$.

Tile Calorimeter

The tile calorimeter uses steel as the absorber material and scintillating tiles as the active material, it is divided into a barrel and two extended barrels at each side of the detector. The barrel measures 5.8m along the z direction and the extended sections each have an additional 2.6m. The Tile Calorimeter is made of modules mounted azimuthally which comprise 3mm thick scintillating tiles between 5mm thick steel plates. The tiles are placed radially in 11 layers of different radial sizes, ranging from 97mm to 187mm. Their lengths along the beam axis go from 219.1mm to 368.2mm at their largest radius. The tiles are made of polystyrene doped with scintillating materials. When a particle enters the steel it creates a particle shower, which makes the scintillating material emit ultraviolet light, that is taken to the visible spectrum by wavelength shifting dopants. In order to protect it and to maximize the scintillation light yield, the tile is introduced into a plastic sleeve with a reflectivity of 95%. The tile then is placed in contact with wave shifting fibers that take the light to photomultipliers in the girder on top of the module. Figure 2.5a shows the placement of the tiles in the module and the way the modules are mounted together.

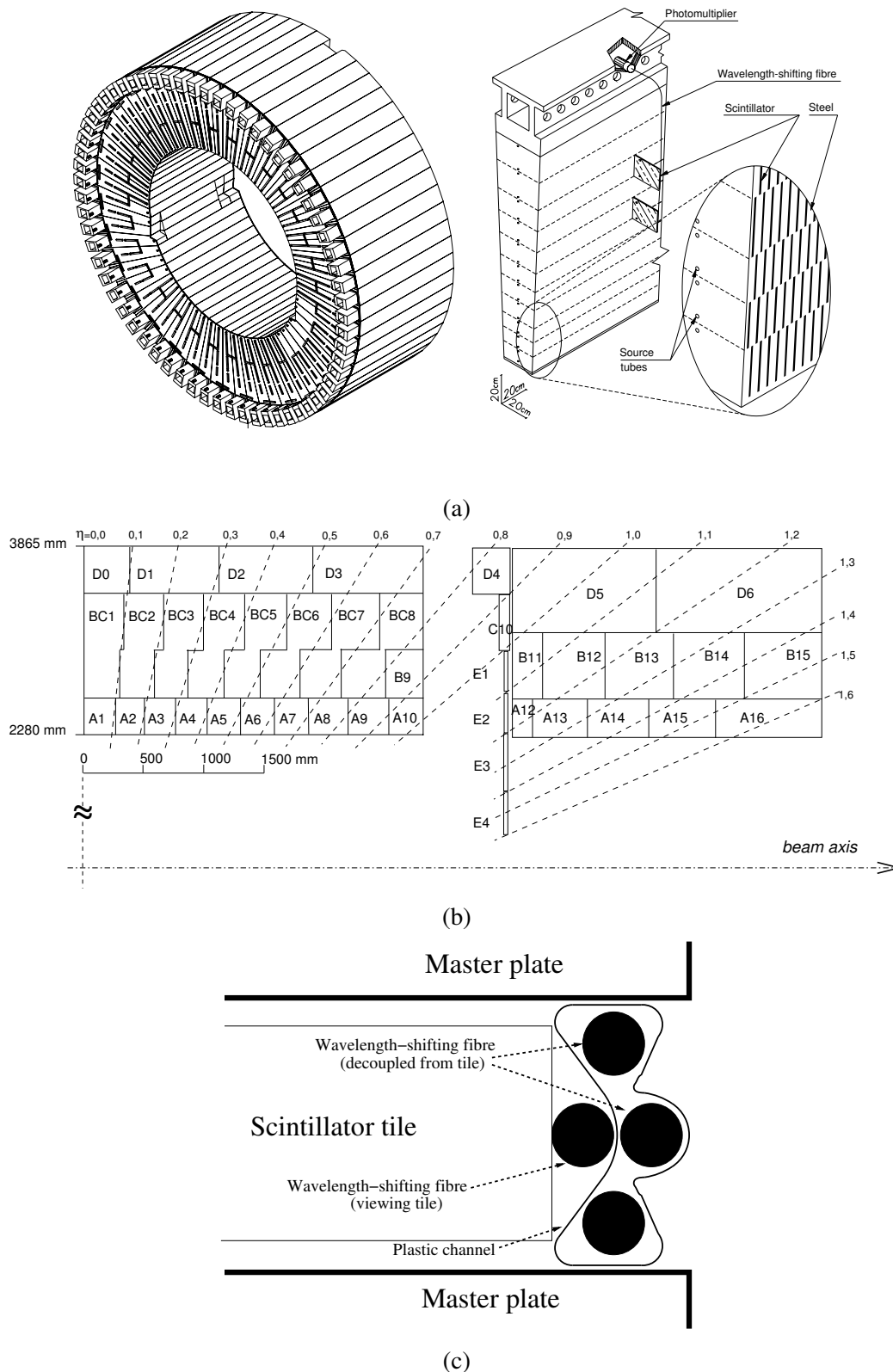


Figure 2.5: In (a) is shown a module and the barrel once they are all assembled. In (b) one side of the Tile Calorimeter after different tiles have been associated to different channels. In (c) three fibers seen inside the channel, while one is outside and in front of the scintillating tile.

The fibers collect the light of two tiles, separated by one radial length as shown in figure 2.5a and then emit light of a lower frequency, their emission peak is at 476nm. The fibers have a

diameter of 1mm and are inserted into a plastic channel holding 3 fibers in the extended barrel and 4 in the Barrel. In order to avoid light cross talk all the fibers have to be kept in the channel (which is opaque) but the one in front of the scintillating material. Also the surface of the channel exposed to the tile is reflective. The mounting of the fibers is shown in 2.5c. The ends of the fibers which are not connected to the photomultiplier are aluminized to increase the light yield. Finally the fibers corresponding to contiguous tiles⁵ are bundled and taken to the photomultipliers in such a way that the bundles define cells of dimensions $\Delta\eta \times \Delta\phi = 0.1 \times 0.1$ for the first two layers and 0.2×0.1 in the last layer. The arrangement of the cells is shown in figure 2.5b. Each channel is read independently by two photomultipliers, by reading the same tile from both sides with different fibers.

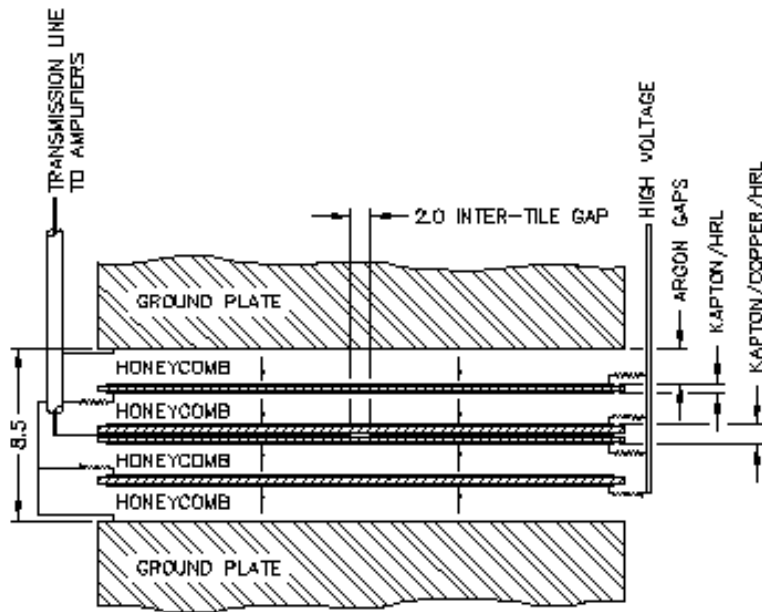
The tile calibration is carried out separately for the electronic components, the photomultipliers and together the scintillating tile and the fibers. The first one uses charge injection, the second one uses a Nd:YV04 laser with a 532nm wavelength and the third one a ¹³⁷Cs radioactive source. This requires the tiles and absorbers to be perforated with holes of 9mm in diameter, shown in figure 2.5a, through which the radioactive source is injected hydraulically, and travels across the entire module.

Hadronic End Cap

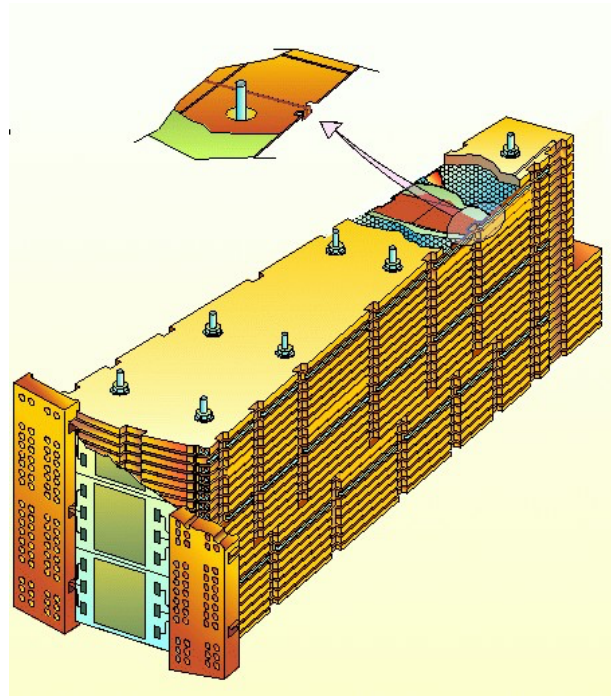
The Hadronic End-Cap (HEC) is housed in the same cryostats as the Electromagnetic End-Caps and situated behind them. Therefore the two sides are submerged in LAr, which acts as active material. The passive material is copper, chosen due to the space constraints and the fact that its use provides the ten extra interaction lengths (additionally to the two provided by the material in front) needed to contain jets coming from 8TeV pp collisions. The reconstruction of forward jets determines the parameters required by the HEC. The wheels cover the range $1.5 < |\eta| < 3.2$. In contrast to the Electromagnetic Calorimeter, the absorber/electrode/LAr system has a flat geometry instead of an accordion shape. The HEC is divided into two wheels, HEC1 and HEC2, one behind the other. Each wheel consists of a system of copper plates that sandwich three electrodes, creating in this way four gaps which are filled with LAr as is shown in figure 2.6a. The HEC is divided into 32 modules. The part of the module that belongs to the HEC1 has 24 25mm thick copper plates and a 12.5mm thick front plate. The part corresponding to the HEC2 has 16 50mm thick plates and a 25mm thick front plate. The gaps created between the plates have a thickness of 8.5mm which are maintained with high precision annular spacers. Each module is kept together with seven rods that go through each plate, as shown in figure 2.6b, the annular spacers are placed around these rods.

Each cell has a granularity of $\Delta\eta \times \Delta\phi = 0.1 \times 0.1$ in $|\eta| < 2.5$ and 0.2×0.2 beyond. This granularity was chosen to reconstruct $W \rightarrow jet + jet$ decays with high p_T . The gap between the absorbers is filled with three electrodes, shown in 2.6a, the central one is called PAD board and the others EST boards. The EST board is made of a layer of polyimide (an insulator) sandwiched with two high resistive layers of carbon-loaded Kapton (CLK). The PAD board has a central $35\mu\text{m}$ layer of copper, sandwiched with polyimide, on top of which later a CLK layer is deposited

⁵Typically 2 or 3 rows and more than 30 tiles.



(a)



(b)

Figure 2.6: Above (a) shows the arrangement of the absorber plates and the electrodes in the HEC, (b) shows a HEC module and the seven rods used to keep the plates in place.

as shown in 2.6a; all the layers are put together with an epoxy sheet glue, not shown in the figure. The configuration with three electrodes and four gaps has the same behavior as the one with two gaps and one electrode but it makes possible to use just 2000V rather than 4000V and to reduce the signal-to-noise ratio and ionization pile-up. The high voltage is applied to the side electrodes and translates in a drift time of $\approx 430\text{ns}$. The space filled with the LAr is kept using honeycomb electrically insulating spacers.

The signals from two consecutive cells in depth are then amplified and summed in the cryostat using GaAs preamplifiers. Placing the preamplifiers in the cryostat offers an optimum signal-to-noise ratio required to detect muons.

Forward Calorimeter

The FCal is located in the same cryostat as the HEC and EMEC and is divided into three modules, the FCal1, FCal2 and FCal3, each measuring 45cm in length and separated by bumpers; furthermore there is a *plug* behind the FCal3 that contains the particle showers, so that they do not reach the muon spectrometer. The FCal detects jets that otherwise would be seen as missing energy, figure 2.7a shows the FCal inside the cryostat.

The FCal is located at about 4.7m from the interaction point and in $3.1 < |\eta| < 4.9$ therefore it is exposed to high particle fluxes. Like the detectors mentioned already the FCal uses LAr as its active material and either copper or tungsten as passive material, however its geometry is different. Given the high doses of radiation the large amount of accumulated charge produced by minimum bias events ⁶ would create an electric field that would distort the signal, so it is necessary to use a small LAr gap. However it is hard to keep a constant small gap between two plates, therefore instead of making cells as sets of absorber plates interleaved with electrodes the cells are made of sets of rods running along the beam axis surrounded by LAr and the system is inserted in a tube as shown in 2.7b. The gap in the FCal1 is $\approx 0.125\text{mm}$, in the FCal2 is 50% larger and in the FCal3 about twice as large. The smaller gaps lead to smaller drift times, for the FCal1 the drift time is only 60ns. The central rod is held at a high voltage and the tube is held at ground potential. The gap size is the most important parameter for the signal and is kept by a plastic fibre wounded around the rod with a variance of $\approx 1\%$ in all the modules. The modules are at 1.8 bar therefore the LAr boiling temperature is 92.7K, and the largest upward variation from the nominal temperature, below 90K, is 1.5K, therefore no boiling is expected.

The FCal1 is an electromagnetic calorimeter, the rod, and the tube surrounding it are made both of copper. These tubes are inserted into copper plates. This metal was chosen because it can dissipate the heat from the minimum bias events efficiently, thus avoiding bubbles in the LAr, and because its Moliere radius is large with respect to the cell size and therefore local fluctuations are averaged out. It is read from the side facing the interaction point, which is the side less exposed to the shower radiation, developed in the absorber.

The FCal2 and FCal3 have rods and tubes made of tungsten in order to contain the longitudinal and transverse spreading of the hadronic showers. The space between the tubes is filled by 1cm long slugs also made of tungsten, which form an hexagonal array. At the front and back

⁶Soft interactions.

ends of the two modules there are two 23.5mm thick copper plates. Both modules are read from the ends that are farthest from the interaction point, which minimizes their exposure to radiation, specially the region between the FCal1 and FCal2, where the hadronic shower maximum occurs.

As for the HEC, the FCal needs ten interaction lengths to stop the hadronic shower, they are split into 2.7λ for FCal1, 3.7λ and 3.6λ for FCal2 and FCal3 respectively. The FCal is contained into a support tube which ends in a conical structure. The reduced size of the FCal leaves space ahead of it which is occupied by the HEC and EMEC, and lined with boron-loaded polyethylene which reduces the neutron reflection towards the tracking system.

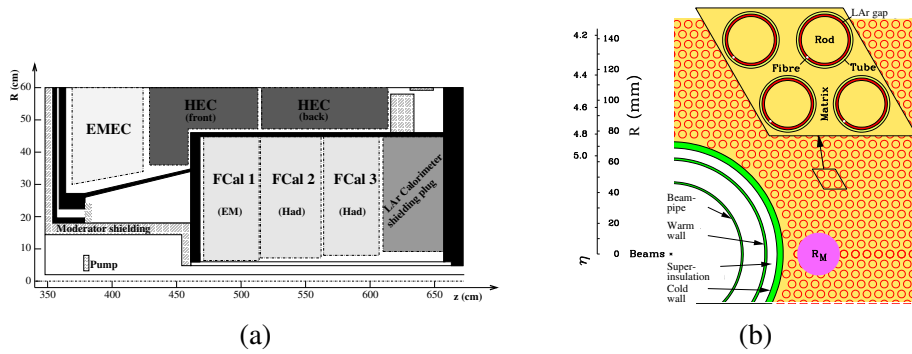


Figure 2.7: In the figure above (a) shows the FCal split into its three modules and placed in the cryostat, (b) shows a view in the (x, y) plane of the detector cells.

2.3 Muon Spectrometer

The Muon Spectrometer (MS) is designed to detect muons and measure their momenta in $|\eta| < 2.7$ and to trigger in $|\eta| < 2.4$. The momentum measurement and particle detection are carried out by the Monitored Drift Tube Chambers (MDT) in the Barrel and End-Cap and by Cathode-Strip Chambers (CSC) in the Barrel beyond $2 < |\eta| < 2.7$. Additionally the Resistive Plate Chambers (RSP) and the Thin Gap Chambers (TGC) are in charge of triggering and supporting the MDT in their tracking task.

2.3.1 Monitored Drift Tube Chambers

In the barrel the MDT chambers are rectangular and are arranged concentrically around the beam. Their radii are approximately 5m, 7.5m and 10m. In the End-Cap the chambers are trapezoidal and form wheels with the beam as their axis, they are located at $|z| \approx 7.4\text{m}$, 10.8m , 14m and 21.5m from the interaction point. There is a region in η , as can be seen in 2.8a, where muons can not traverse the outer MDT wheel but they traverse the inner and the medium ones. There an *extra* wheel with MDT chambers has been placed, the EEL and EES, about 3 to 3.6m behind the inner MDT wheel. The MDT chambers are made of drift tubes, forming two multi layers of three or four tubes, each put together with epoxy glue. These multilayers are separated by three

support beams (spacers) with heights ranging from 6.5mm to 317mm which are connected by two longitudinal beams forming all an aluminum frame. The drift tubes are at a pressure of 3 bar and with a diameter of 29.97mm filled with Ar and CO₂ in a 93/7 proportion, mixture chosen because of its good aging properties. However its drift time is 700ns, higher than other mixtures and there is a nonlinear space-drift time relation. At the center there is a tungsten-rhenium wire of 50μm of diameter at 3080V, the anode. The signal is collected at the opposite end from where the high voltage is injected. The tubes are oriented along ϕ and are of identical length in the Barrel but vary with R in the End-Cap. A diagram of the MDT chamber can be seen in 2.8b

The MS is in charge of measuring the p_T of muons with high precision and is built in such a way that its measurement of the p_T of a 1TeV particle should have a resolution of 10%. The straightness of the drift tubes is required to be better than 100μm. The relative position of the chambers in radially consecutive stations is monitored with an accuracy of 30μm. The sag caused on the chambers by gravitational forces is translated in a sag of the wires in each tube. To correct this the sag adjustment system applies an adjustable force to the central cross plate. The precision achieved with this correction is 10μm. All these adjustments mean that the resolution of the MDT is limited by the resolution of each tube. The large expected background from photons and neutrons should ionize the Ar/CO₂ gas mixture. This will distort the electric field and degrade the resolution, which is expected to be 60 – 80μm and given that many layers are combined one reaches 35μm. Also having many layers means that if one tube breaks down the measurement can be still carried out with the others.

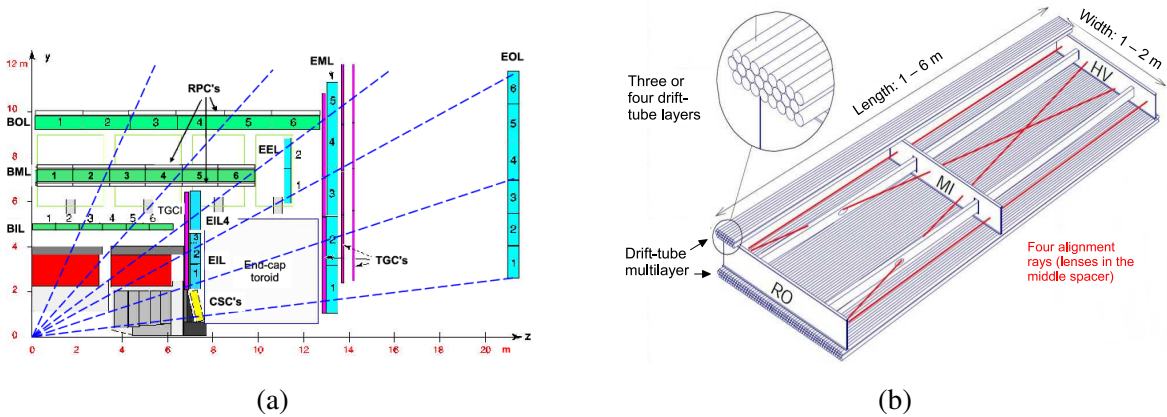


Figure 2.8: In the figure above (a) shows the different components of the MS in the bending ($z - R$) plane. (b) Shows an MDT chamber with its support structure.

When a track traverses a drift tube the quantity of interest is the radius of the circle tangent to the track and centered on the wire, therefore only the initial part of the electric pulse produced is relevant and a dead time is implemented in the front-end readout. This geometry also implies that the resolution of the measurement should be independent of the direction in which the track enters the drift tubes.

2.3.2 Cathode Strip Chambers

The MDT's can operate at rates of up to $150\text{Hz}/\text{cm}^2$ which are exceeded for $|\eta| > 2$, where MDT's are replaced by the cathode strip chambers (CSC) for which the rates can go up to $1000\text{Hz}/\text{cm}^2$.

The CSC covers the range $2 < |\eta| < 2.7$, is at 7m from the interaction point and is made of two wheels with eight chambers each. Each chamber is made of five 18.75mm thick layers of polyurethane foam, clad with 0.82mm copper strips. Between the layers of polyurethane are placed $30\mu\text{m}$ diameter wires made of gold plated tungsten with 3% rhenium. The wires are arranged radially and act as the anodes at a potential of 1900V, while the strips are oriented on one side perpendicularly and on the other side parallel to the wires, the strips act as cathodes. The distance between the wires and the plane with the strips is 2.5mm and it is the same as the distance between the wires. In this way the CSC chambers can provide information about both coordinates, in contrast to the MDT chambers.

The two sets of strips in the CSC do not have the same granularity. The strips perpendicular to the wires have a pitch of $\approx 5.4\text{mm}$ which results in a resolution of $60\mu\text{m}$, while the strips going along the wires are separated by 21mm or 12.92mm and the corresponding resolution is 5mm. The signal is retrieved from the strips and between two strips connected to amplifiers there are two not connected to anything, but that couple capacitively to the readout strips.

The factor limiting the resolution is the electronic noise and the spread of the deposited charge along the anode due to delta electrons⁷, the Lorenz force along the wire and the presence of inclined tracks. In order to minimize the presence of inclined tracks the CSC's are tilted in such a way that they face the interaction point as can be seen in 2.8a. The CSC's have a faster time response than the MDT's and the spread of their signals is between 15 – 25ns, therefore they can be used to distinguish different beam crossings.

2.3.3 Trigger Chambers

The trigger chambers cover the full ϕ range and $|\eta| < 2.4$. The End-Cap chambers ($1.05 < |\eta| < 2.4$) are under stringent constraints. For instance for a given p_T , the momentum in the Barrel is much smaller than the momentum in the End-Cap, making the curvature of the track smaller and therefore harder to measure. This is compounded by the fact that the magnetic field in the End-Cap is weaker (and specially inhomogeneous in $1.3 < |\eta| < 1.65$). Also the distance between the chambers is smaller than in the Barrel. Finally the radiation levels are ten times higher than in the Barrel, therefore the End-Cap requires trigger chambers with a higher granularity and more radiation hardness than the Barrel.

There are two types of trigger chambers, Resistive Plate Chambers (RPC), in $|\eta| < 1.05$, located in contact with the Barrel MDTs and Thin Gap Chambers (TGP) in $1.05 < |\eta| < 2.4$ located in contact or near the End-Cap MDTs. They can both be seen in figure 2.8a.

⁷Electrons that acquired enough energy from another particle to cause ionization.

Resistive Plate Chambers

The RPC's are arranged cylindrically in three stations, the first two stations are used to trigger on particles with $6 < p_T < 9\text{GeV}$ while the third one is also used for particles with $9 < p_T < 35\text{GeV}$. Each station has two layers as shown in figure 2.9.

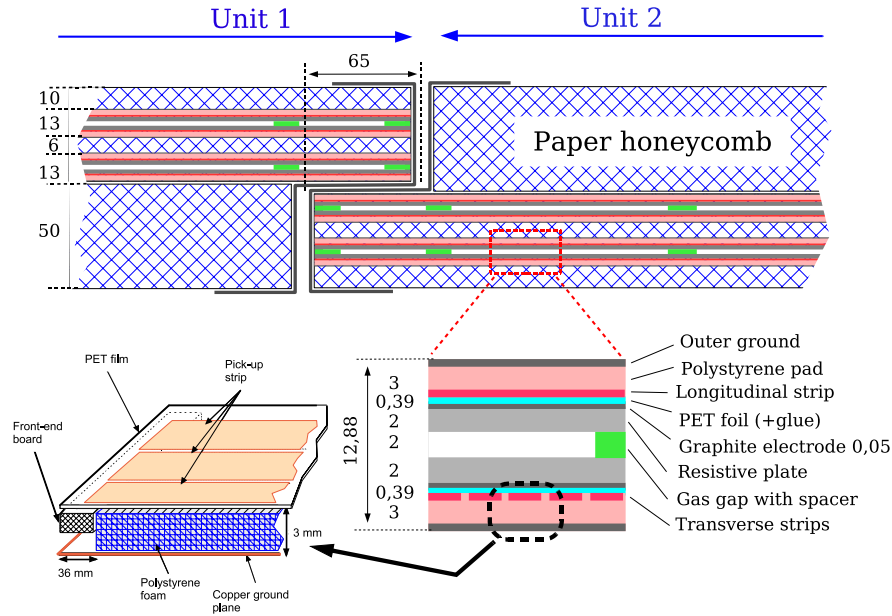


Figure 2.9: The figure shows a resistive plate chamber made of two units.

Each unit consists of two gas volumes limited by several films of different materials. The first layers are phenolic-melaminic plastic plates with a $10^{10}\Omega \cdot \text{cm}$ resistivity, separated by 2mm spacers. The space enclosed by the plates is filled with a mixture of $\text{C}_2\text{H}_2\text{F}_4/\text{Iso}-\text{C}_4\text{H}_{10}/\text{SF}_6$ in a 94.7/5/0.3 proportion. The outer surface of the plates is covered by graphite layers, on one of them a potential of 9.8kV is applied while the other acts as the ground. The graphite is covered by a $190\mu\text{m}$ PET (polyethylene terephthalate) film, above which are the readout strips. The upper strips run perpendicularly to the lower ones, allowing the measurement of the track coordinate in the both the bending and non-bending planes⁸, the signal is read by capacitive coupling. Finally above the strips is a layer of Polystyrene covered with copper.

Thin Gap Chambers

The Thin Gap Chambers (TGC) are located in two concentric wheels at $1.05 < |\eta| < 1.92$ and $1.92 < |\eta| < 2.4$. They fulfill the task of the RPC but in the End-Cap region. However, as can be seen in 2.8a, there is not TGC on the outer MDT layer of the End-Cap, here, due to the lack of magnetic field, the ϕ coordinate can be extrapolated from the track direction in the middle MDT layer.

⁸The bending plane is the $R - z$ plane, the non-bending plane is the $R - \phi$ plane.

The TGCs are made of gas cavities with a mixture of CO_2 and n-pentane ($\text{n-C}_5\text{H}_{12}$). The cavities contain wires that act as anodes, oriented in ϕ which are at 2900V and strips that act as cathodes, oriented in the radial direction and connected to the amplifiers. The distance between the anode and the cathode is 1.4mm and the distance between the anodes is 1.8mm. The large anode potential and the small distance between anodes and cathodes makes it possible to get very small drift times. The TGC layer in front of the EM wheel (see 2.8a) is made of chambers with three gas volumes, while the other two behind the EM wheel are made of two gas volumes. The gas volume is limited by a 1.6mm FR4⁹ plate, the side facing the anodes is coated with a thin graphite layer, the other side of the FR4 is clad with copper. In both types of chambers there are two sides in which the copper is segmented in strips, these are the cathodes, while the other surfaces are continuous. Figure 2.10 shows the two types of chambers, with two and three gas cavities.

The chambers are sealed and CO_2 is circulated around them and monitored, if n-pentane is detected the high voltage and low voltage are switched off.

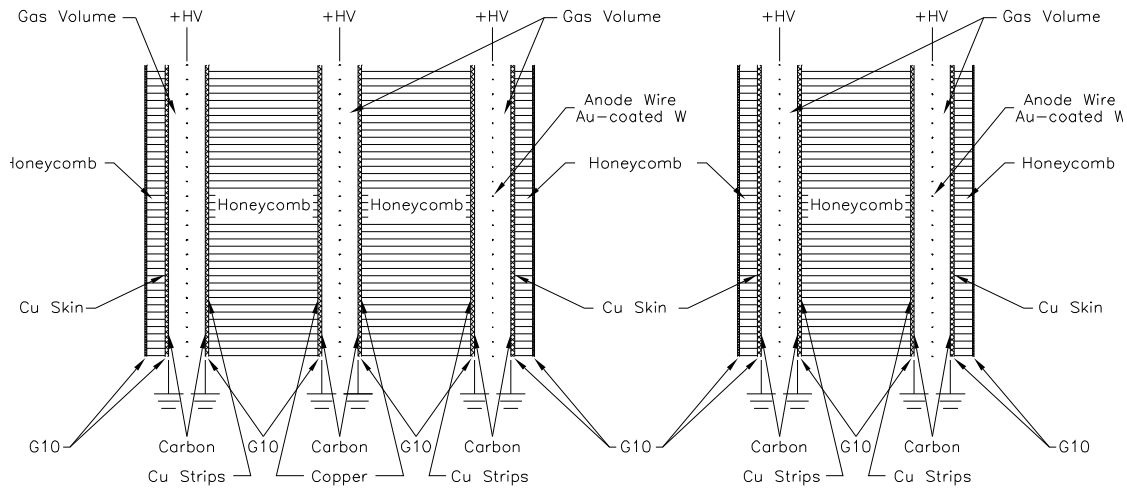


Figure 2.10: At the left is a thin gap chamber with three gas chambers, at the right one with two.

2.4 Luminosity Measurement

The luminosity is defined in (2.3), where R_{inel} is the rate of events in inelastic interactions and σ_{inel} is the associated cross section.

$$\mathcal{L} = \frac{R_{inel}}{\sigma_{inel}} \quad (2.3)$$

In order to measure the luminosity various detectors count the number of inelastic interactions per crossing, μ^{vis} , which corresponds to a cross section σ_{vis} . The luminosity then can be written as (2.4) where f_r is the number of revolutions per second for the bunches and n_b is the number of

⁹Epoxy resin binding fiberglass cloth.

bunches circulating in the LHC ring. σ_{vis} cannot be calculated directly but the luminosity can be written as (2.5), where n_1 and n_2 are the number of particles in each bunch and $\Sigma_{x(y)}$ is the width of the bunches in the $x(y)$ directions.

$$\mathcal{L} = \frac{\mu^{vis} n_b f_r}{\sigma_{vis}} \quad (2.4)$$

$$\mathcal{L} = \frac{n_b f_r n_1 n_2}{2\pi \Sigma_x \Sigma_y} \quad (2.5)$$

Through a van der Meer Scan [11] the beams are moved across each other in both vertical and horizontal directions as the μ_{vis} is measured. In this way the sizes of the bunches can be calculated and also the μ_{vis} at its highest value.

The next quantity that needs to be calculated is $n_1 \cdot n_2$. This is done by the Fast Bunch-Current Transformers (FBCT), which can measure the n_i for individual bunches. The Direct-Current Current Transformers (DCCT) can measure the intensity of the current of the beam, however it does not retain the information for individual bunches [12]. The DCCT has a better accuracy but it needs to collect data over hundreds of seconds to achieve the required precision. Therefore n_i is first measured with the FBCT and then rescaled using the DCCT measurement.

From this numbers and using (2.4) one can extract σ_{vis} , which now can be used to extract the absolute luminosity for a specific beam crossing by measuring μ^{vis} with any of many detectors. An alternative way of getting σ_{vis} is through simulation of the non-diffractive, single-diffractive and double-diffractive processes with a generator (e.g PYTHIA) however the uncertainties associated are too large.

2.4.1 LUCID

LUCID (LUminosity measurement Cerenkov Integrating Detector) is primarily used to measure relative luminosities. It consists of 20 1.5m long reflective aluminum tubes with 15mm of diameter wrapping the Beryllium beam pipe at ± 17 m of the interaction point and placed into an aluminum vessel. The vessel is filled with C_4F_{10} at a pressure of 1.2 – 1.4bar and when a charged particle enters them it produces around 70 photoelectrons. These photo electrons are reflected in average three times before going through a quartz window and producing an electric pulse in the photomultiplier tubes. In some cases the incident particle produces an extra 50 photoelectrons in average when traversing the quartz. A tube registers a hit if the signal it receives is above a threshold equivalent to 15 photoelectrons. The number of particles entering the tube is deduced by the height of the induced pulse.

The number of hits in LUCID is used to calculate μ_{vis} [13]. This number and σ_{vis} are used in (2.6), where the sum is over the bunch crossings, to get the luminosity corresponding to a lumiblock.

$$\mathcal{L} = \sum_{i=BC} \mu_i^{vis} \frac{f_r}{\sigma_{vis}} \quad (2.6)$$

2.4.2 ALFA

The Absolute Luminosity For ATLAS (ALFA) [14] detector is used to measure the absolute luminosity. According to the optical theorem, (2.7) can be used to get the total cross section σ_{tot} , where $f_{el}(t = 0)$ is the scattering amplitude from elastic processes extrapolated to zero momentum transfer, t , where $t = -p\theta$ is the product of the momentum of the beam and the scattering angle.

$$\sigma_{tot} = 4\pi \cdot \text{Im}[f_{el}(t = 0)] \quad (2.7)$$

ALFA consists of two detector stations on each side of the interaction point. The detectors are four meters away from each other and 240 meters away from the interaction point. In each detector station there are two detectors that are moved towards the beam one from above and the other from below. Figure 2.11a shows the upper detector.

The detectors are made of ten modules each containing 64 scintillating fibers [14]. The fibers are arranged as in figure 2.11b, in what is called a UV or stereo geometry, the overlapping region between the fibers defines the active area. The fibers' cross section is a square of dimensions $0.5 \times 0.5\text{mm}^2$.

In order to be able to extrapolate the scattering amplitude to $t \rightarrow 0$ one needs to estimate the particle flow very close to the beam, the detector used to do this is inside the beam pipe as shown in figure 2.11a and can get as close to the proton beam as 10σ ($\approx 1\text{mm}$)¹⁰.

¹⁰The density of protons in the beam is assumed to be gaussian, with standard deviation equals to σ .

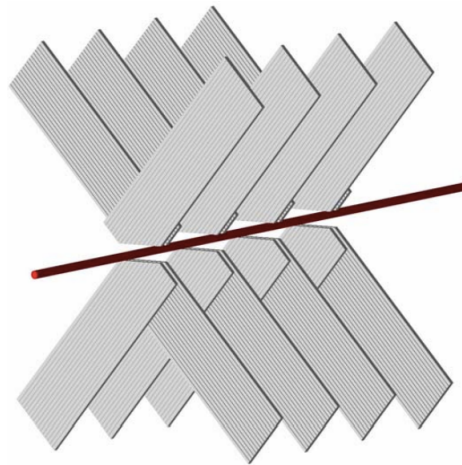
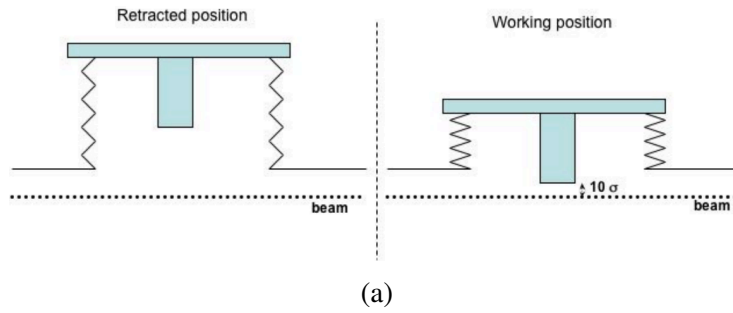


Figure 2.11: (a) shows a cross section of the Roman pot configuration in ALFA. At the right is the detector in a working position, at about 1mm of the beam. At the left the same detector retracted. (b) shows the geometry of the scintillating fibers.

Chapter 3

Monte Carlo, Data and Physics Objects

3.1 Event Topology

This thesis will discuss the search for a heavy resonance decaying into either a WW or a ZZ pair, which decays hadronically. The hadronic final state offers the highest branching ratios as can be seen in figure 3.1.

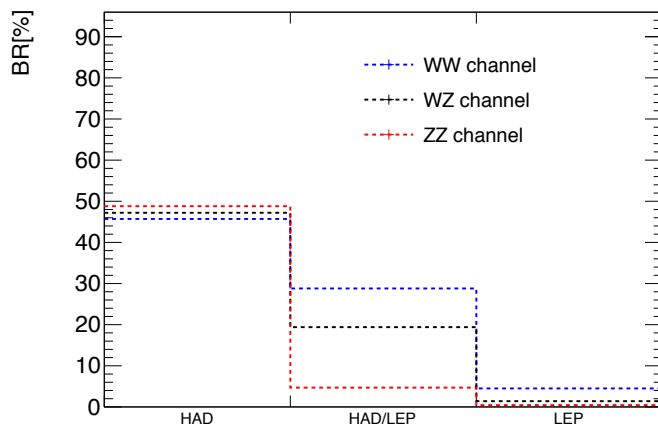


Figure 3.1: Theoretical prediction of the branching ratio of a WW , WZ and ZZ pair, to fully hadronic, semi-hadronic and fully leptonic final states.

When a vector boson, coming from a relatively low mass resonance, decays hadronically, it decays into two quarks which give rise to four well defined jets; this is what is called the *resolved* regime. However when the resonance mass goes beyond $\approx 1\text{TeV}$ the vector bosons are boosted and each of them produces a single large jet, when decaying hadronically. This implies that the final state should consist of two large radius jets, whose invariant mass spectrum will be used to search for new physics. Thus, a heavy resonance should be visible as an excess of events, localized around a certain dijet mass in a smoothly decreasing background.

3.2 MonteCarlo Samples

3.2.1 Graviton Signals

The m_{JJ} distribution for the Graviton is obtained by generating events with the model implemented in [15]. The signal samples were produced in graviton mass intervals of 100GeV. CalcHEP [16] was used given that the gravitons decay into longitudinally polarized bosons and the generator retains the spin correlations; the PDF used was CTEQ6L1 and each sample contains 20000 events. The shape and cross section of the signal were cross checked with MadGraph [17]. The hadronization and showering were carried out with PYTHIA8 [18].

In figure 3.2 are shown the Graviton mass distributions for the $G \rightarrow WW/ZZ$ channels both at truth level and after simulation. It is clear the effect of the detector on the mass resolution of the graviton, the simulated samples are more *spread*. Also simulation is shifted downwards in mass, which later will be corrected when the samples be calibrated.

The events were simulated using FullSim [19] because substructure variables need to be studied in order to optimize cuts and maximize the signal significance.

3.2.2 Background

The background is dominated by QCD dijet events with a small amount of $W/Z + jets$ events. The QCD dijet samples available for the analysis were generated with PYTHIA8, Herwig++ and POWHEG interfaced with PYTHIA, from now on referred just as POWHEG. The PYTHIA and Herwig samples are generated at leading order and there are very large higher order corrections that should be applied. Therefore data driven approaches are used to model and optimize many quantities. However the POWHEG interfaced with PYTHIA samples are generated at next to leading order.

The Monte-Carlo (signal and background) and the data are calibrated at particle level and all the plots presented will include calibrated quantities. The calibration will be mentioned in section 3.6.

Before using the dijet samples for optimization studies one first re-weights the p_T spectrum of the leading jet so that the data-Monte Carlo agreement is improved. The data and background samples whose distributions are re-weighted are required to pass the cuts on table 3.1 plus a set of standard data quality requirements. In figure 3.3 one can see the distributions before and after the weights are applied.

Figure 3.4 shows the PYTHIA QCD background prediction overlaid with the $W + jets$ and $Z + jets$ distributions.

The cross sections of the different background samples, in different p_T slices are listed in Appendix A. In the same Appendix are also the cross sections for the different signal samples.

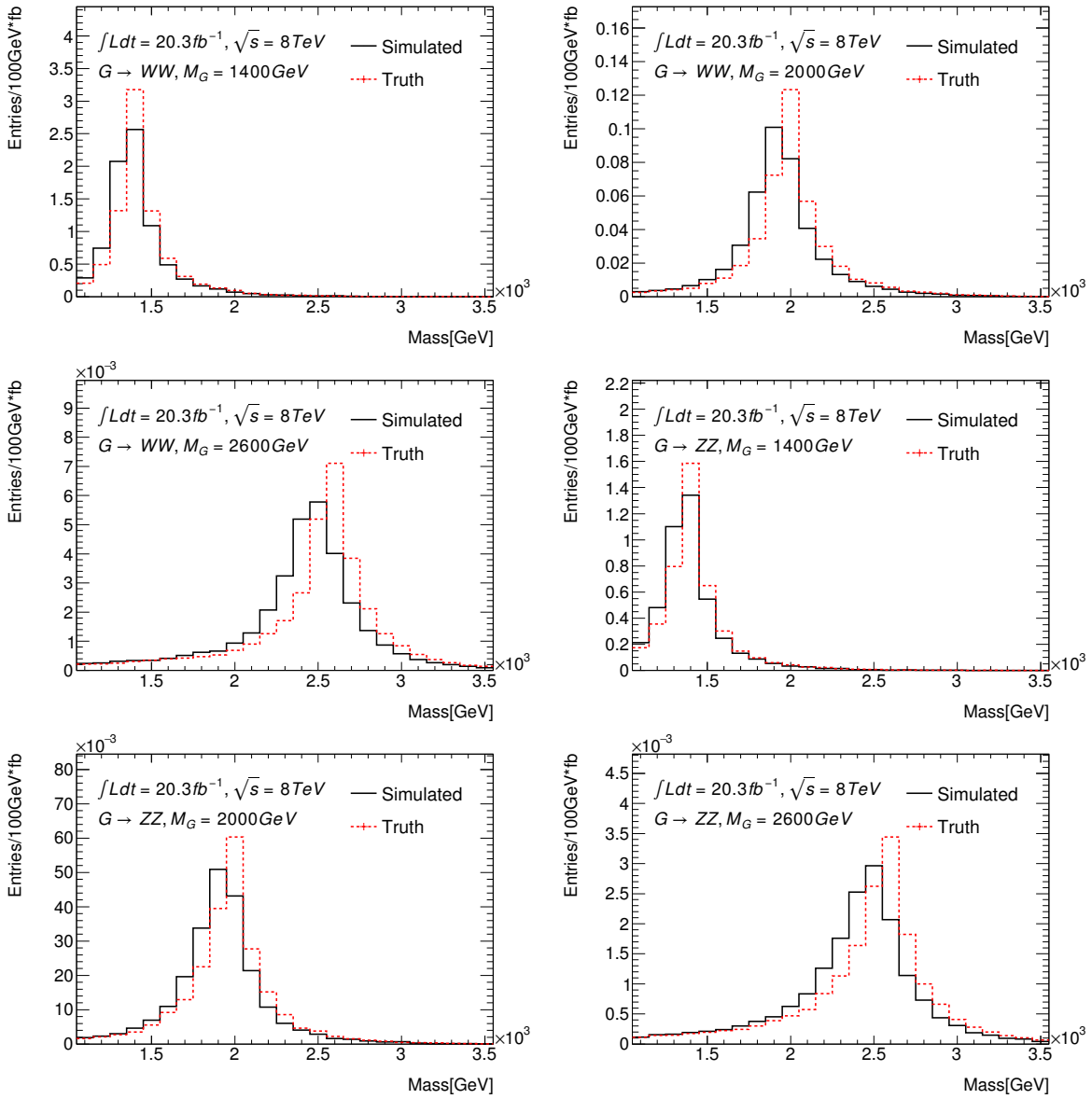


Figure 3.2: Dijet Mass distributions for both $G \rightarrow WW$ and $G \rightarrow ZZ$ for three different mass points at truth level and after simulation.

Name	Value	Description
e/μ veto	true	To be orthogonal to semileptonic and fully leptonic channels.
Trigger	EF_j360_a10tcm	Lowest unrescaled trigger for large radius jets.
\cancel{E}_T	$< 350 \text{ GeV}$	To be orthogonal to analyses with $Z \rightarrow \nu\nu$.
LC3	< 3	Number of jet's leading clusters (largest energy clusters) in a dead module of the TileCal.

Table 3.1: Cuts applied to data and MC before optimization studies.

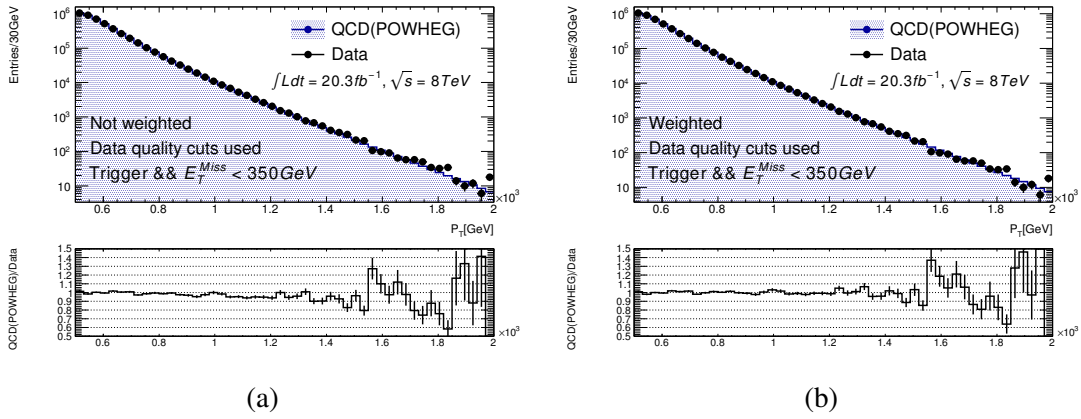


Figure 3.3: In (a) the p_T distribution of the leading jet before re-weighting and in (b) after it.

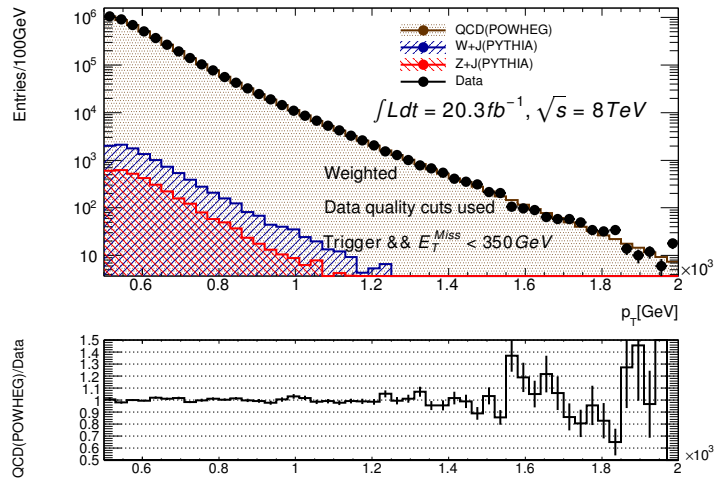


Figure 3.4: Different background components compared with data.

3.3 Tracks

Tracks are used to discriminate between signal and background. The tracks are reconstructed in the inner detector, within $|\eta| < 2.5$ and have to satisfy $p_T > 500\text{MeV}$. Tracks are associated to jets through *ghost association* [20]. Ghost association consists of including tracks in the clustering algorithm, as if they were other topo-clusters¹ but taking their momentum to be infinitesimal.

3.4 Jets

When a quark hadronizes the parton shower consists of around one thousand particles. These particles are seen as energy deposits forming clusters in the detector. These clusters have to be put together, forming what is called a *jet*, which is supposed to represent the original quark. In order to build a jet one starts with a list of objects (clusters, particles, tracks...) and calculates the distances $d_{i,j}$ between the elements i and j and also the quantity $d_{i,B}$. The momenta of the closest pair are added, getting in this way a new list of objects. If for a given object i the quantity $d_{i,B}$ is smaller than all of the $d_{i,j}$ then i is taken out of the list and considered a jet itself. The process continues until the list is empty.

Both Anti-kt [21] and Cambridge/Aachen [22] algorithms perform the clustering by combining the closest objects, but they differ on the definition of the metric and the quantity $d_{i,B}$. The Cambridge/Aachen algorithm uses (3.1) with $p = 0$, the Anti-kt algorithm uses $p = -1$ and the kt algorithm uses $p = 1$.

$$d_{i,j} = \min(k_{ti}^{2p}, k_{tj}^{2p}) \frac{\Delta R_{ij}^2}{R^2} \quad \text{and} \quad d_{i,B} = k_{ti}^{2p} \quad (3.1)$$

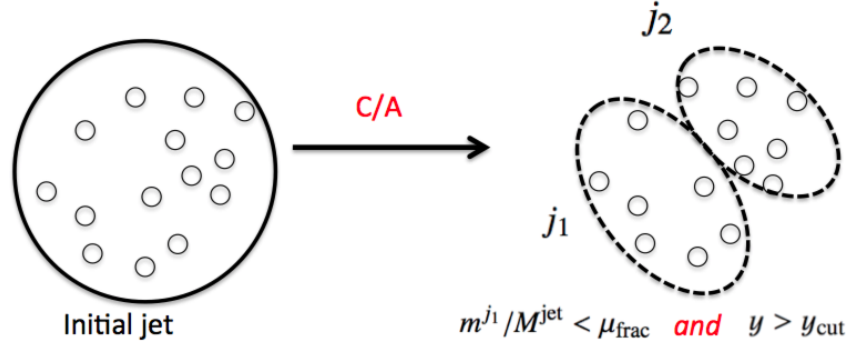
$\Delta R_{ij}^2 = (y_i - y_j)^2 + (\phi_i - \phi_j)^2$, R is the radius of the jet and $d_{i,j}$ is the distance between the i^{th} and j^{th} objects.

3.4.1 Split Filtering and Trimming

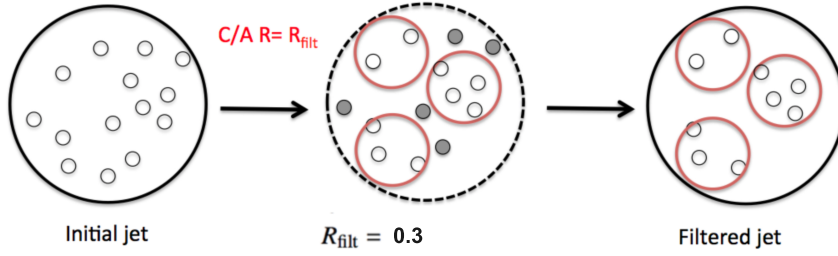
This search focuses on massive resonances, therefore the W 's or Z 's are very boosted and the resulting quarks from their decays are very close to each other. After hadronization the reconstructed object is a single large radius jet (either Anti-kt or C/A). Many of the energy deposits in the jet will come from soft interactions happening in the same bunch crossing (on time pile-up) or in a different bunch-crossing (out of time pile-up). In order to get rid of these extra energy deposits one can *split filter* or *trim* a jet. The split filtering algorithm [23] is illustrated on figure 3.5 and consists of:

- **Splitting:** Go back one step in the clustering process in such a way that one gets two jets.

¹A topocluster is a cluster seeded with cells with energies larger than $4\sigma_{noise}$, to which are added the neighboring cells with $E \geq 2\sigma_{noise}$ and finally the surface is obtained with the remaining cells. σ_{noise} is the average noise in a cell.



(a) Splitting and grooming.



(b) Reclustering and filtering.

Figure 3.5: Jet grooming and filtering.

- **Grooming:** Cut on the momentum balance, y , and mass drop, μ , if the jet does not pass the cut the lowest mass jet is thrown away and the process is repeated with the heavier jet until nothing is left or until two subjets are found for which the cut is satisfied.
- **Filtering:** Take the groomed jet and **recluster** it with a smaller radius R_r jet, taking the $n_r = 3$ highest p_T subjets².

The momentum balance and mass drop are defined as

$$y = \frac{\min(p_{Tj_1}^2, p_{Tj_2}^2)}{m_J^2} \Delta R_{j_1, j_2}^2 \quad (3.2)$$

$$\mu = \frac{\max(m_{j_1}, m_{j_2})}{m_J} \quad (3.3)$$

Where J is the large radius jet and j_1 and j_2 are its subjets. The parameters for the jet used in this search are in table 3.2 For the anti-kt jets the QCD contamination is dealt with using trimming [24]. It consists of reclustering the jet J using smaller radius anti-kt jets. If for a given sub-jet, j , $p_{Tj}/p_{TJ} < f$ then j is thrown away, what remains is the trimmed jet.

²Three subjets are allowed in case one of the quarks radiates a gluon. Not all jets have three subjets.

Parameter	C/A
Radius	1.2
\sqrt{y}	> 0.2
μ	1
R_r	0.3
n_r	3

Table 3.2: Different parameters used to build and groom the jets used here.

3.5 Systematics

In order to assess the uncertainty in the scales and resolutions of different quantities one uses the PYTHIA QCD dijet MC and W' signal samples respectively. Some of the quantities whose uncertainties were deduced are listed in table 3.3 with their respective values.

Source	Scale (%)	Resolution (%)
p_T	2	5
m_J	3	7.5
\sqrt{y}	2	16

Table 3.3: Systematics on the scales and resolutions of the jet's p_T , mass and momentum balance.

The scales were deduced using the double ratio method [25] which for a quantity X is defined as in (3.4)

$$\alpha_X = \frac{\langle X^{\text{track jet}} / X^{\text{calo jet}} \rangle_{\text{Data}}}{\langle X^{\text{track jet}} / X^{\text{calo jet}} \rangle_{\text{MC}}} \quad (3.4)$$

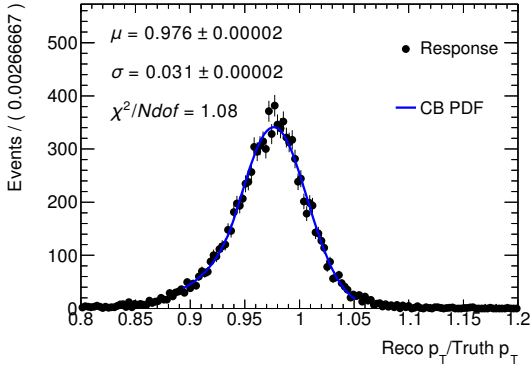
The $\langle \rangle$ symbols represent the average of the ratio of X measured for a jet in the tracking system³ and a jet in the calorimeter. These jets are *matched* by requiring $\Delta R < 0.3$.

The systematics deduced with the double ratio method should be applied to a boson tagged data set. Therefore they are deduced using a sample in data and simulation, where the jets were tagged, which implies taking jets passing only $60 < m_J < 110\text{GeV}$, $\sqrt{y} > 0.45$ and $n_{\text{trk}} < 30$ (see chapter 4). Additionally the jets used to carry out the studies were required to pass the cut (3.5) which reaches a $\approx 60\%$ efficiency for tagged jets.

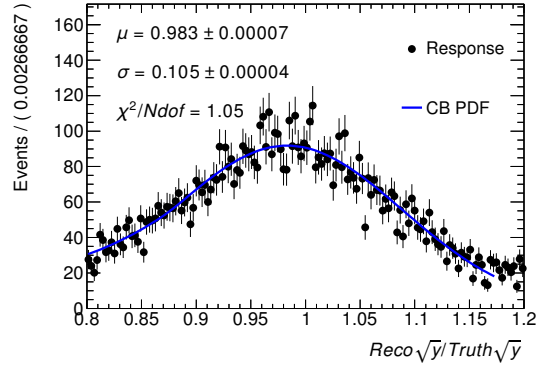
$$\Delta R_{q\bar{q}}^{\text{calo}} - \Delta R_{q\bar{q}}^{\text{track}} < 0.1 \quad (3.5)$$

The resolutions for the p_T and \sqrt{y} , described above, were obtained from their *response*, defined as $X_{\text{truth}}/X_{\text{reco}}$. This ratio, although not necessarily equal to one, should be normally

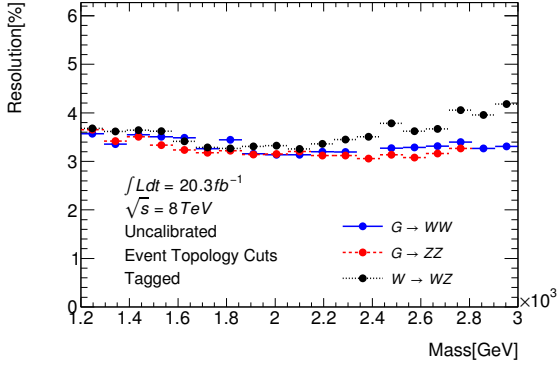
³Which are built from tracks instead of topo-clusters



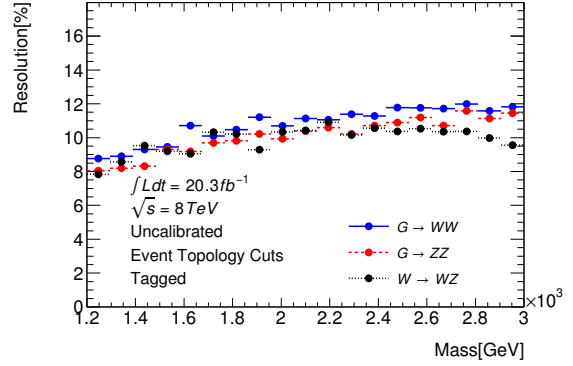
(a) p_T response for a $G \rightarrow WW$ signal sample for $m_G = 2\text{TeV}$



(b) \sqrt{y} response for a $G \rightarrow ZZ$ signal sample for $m_G = 2\text{TeV}$



(c) p_T resolution for each signal mass.



(d) \sqrt{y} resolution for each signal mass.

Figure 3.6

distributed around some point. This distribution is fitted to a gaussian or Crystal Ball distribution and the resolution taken as σ_x/μ_x . Figure 3.6a shows the fit to the p_T response and 3.6b the one corresponding to \sqrt{y} . The final values are obtained from figures 3.6c and 3.6d.

The values chosen were adopted across the diboson analyses as a conservative estimate, based on the width of the response to the p_T and \sqrt{y} . The resolution on m_J was deduced from fitting the W boson mass distribution from the $W + jets$ simulated samples.

These uncertainties represent the limitations of the simulated samples to represent the data.

3.5.1 Other Sources of Uncertainty

Other sources of uncertainty considered are listed in table 3.4, where the luminosity uncertainty is obtained using ATLAS tools used for luminosity calculation. The PDF uncertainty is gotten from comparing the variation of the number of events in a Graviton signal sample as the PDF is changed. The systematics associated to the generator were obtained by comparing a W' mass distribution, after showering with PYTHIA and HERWIG, the largest discrepancy implied a 5% uncertainty. However the largest source of uncertainty is associated to the efficiency of one of

the boson tagging cuts, which will be discussed in chapter 4.

Source	Uncertainty (%)
Luminosity	2.8
PDF	3.3
Generator	5
n_{trk} cut	19

Table 3.4: Additional systematics associated to the luminosity, generator settings and the efficiency on the n_{trk} cut.

3.6 Jet Energy and Mass Calibration

Most of the calibration work was done by Chris Malena Delitzsch. In figure 3.2 one can see that at truth level and after simulation the graviton mass distributions differ, this is a detector effect. The jet's constituents are clusters and their energies might be underestimated or some of them might be thrown away. Furthermore non-uniformities in the values of the energy and mass are introduced by the detector. To counteract this and also bring back the mass and energy spectra to the scale of the truth level value the jets were calibrated.

The jet calibration was carried out using the QCD samples generated with PYTHIA. In order to calibrate, the jets have to be matched to truth jets, this is done by associating jets within $\Delta R < 0.3$. Calibrating is equivalent to finding a function $\mathcal{F}_{calib}^{E/M}$ that takes the value of the energy or mass of a jet and returns a *truth* version of these quantities. Equation (3.6) shows the relationship between the calibrated and uncalibrated energies and masses

$$E_{LCW+JES}^{jet} = \frac{E_{LCW}^{jet}}{\mathcal{F}_{calib}^E(E_{LCW}^{jet})}, \quad m_{LCW+JES}^{jet} = \frac{m_{LCW}^{jet}}{\mathcal{F}_{calib}^m(E_{LCW}^{jet} * JES)} \quad (3.6)$$

where \mathcal{F}_{calib}^E and \mathcal{F}_{calib}^m are used for the energy and mass respectively. The term with an * in the denominator indicates that the mass is calibrated after calibrating the energy. \mathcal{F}_{calib} is parametrized as in (3.7) and it is fitted, where a_i are the fitting parameters and N_{max} is between one and six.

$$\mathcal{F}_{calib}^{E/m}(E_{reco}^{jet}) = \sum_{i=0}^{N_{max}} a_i (\log(E_{reco}^{jet}/E_{truth}^{jet}))^i \quad (3.7)$$

$$\mathcal{R}_{E/m}^{jet}(\eta_{det}) = \frac{(E/m)_{reco}^{jet}}{(E/m)_{truth}^{jet}} \quad (3.8)$$

The values of \mathcal{F} in the fit come from the average of the energy or mass response defined in (3.8) and evaluated in an energy- η bin. The independent variable in the fit of the mass or

energy calibration function is taken as the average in a bin of the values of the E^{jet} at truth or reconstructed level respectively. Figure 3.7a shows the energy response in function of η before calibration, 3.7b shows it after, the same is shown in 3.7c and 3.7d but for the mass.

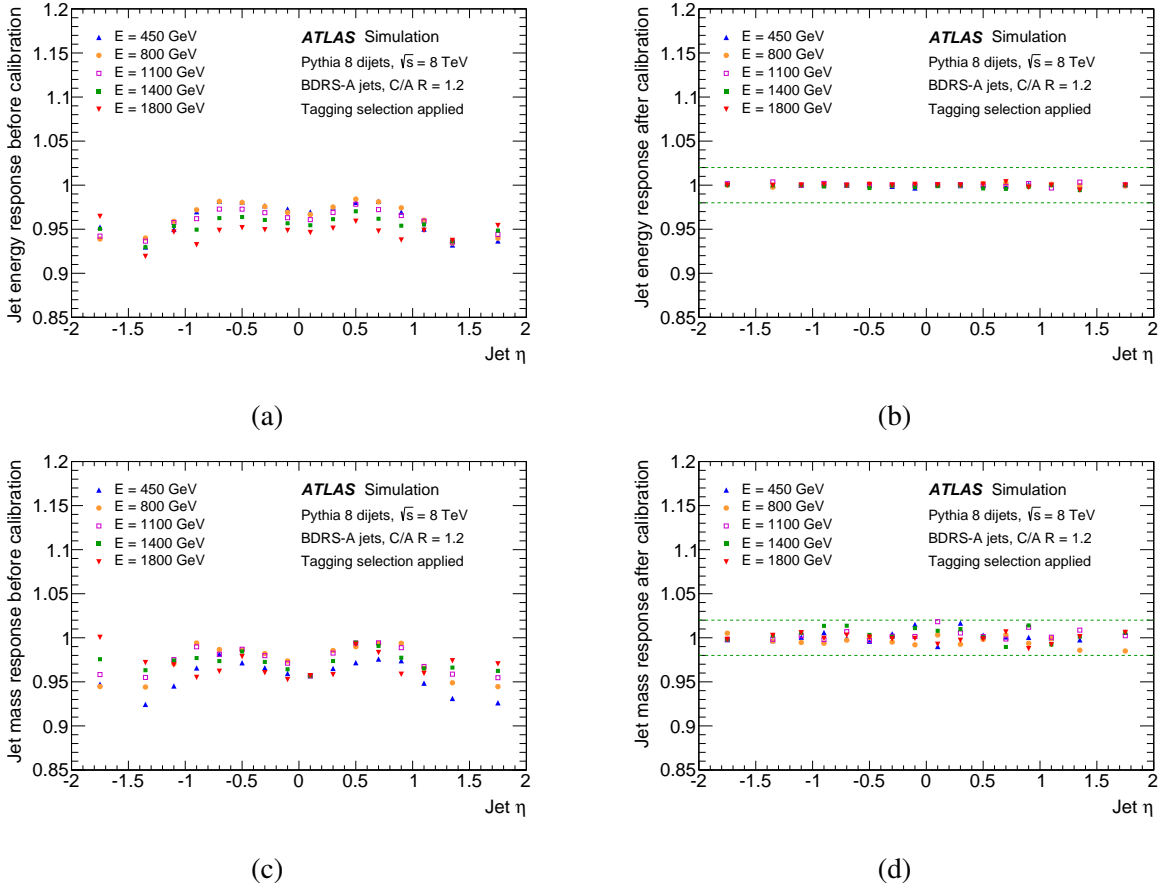


Figure 3.7: (a) shows the energy response for different p_T slices in PYTHIA. (b) shows the same distributions after calibration. (c) and (d) show the same distributions but for the mass response.

The binning used in the energy of the jet at truth level can be also seen in the figures. The binning used in η is -2.0, -1.5, -1.2, -1.0, -0.8, -0.6, -0.4, -0.2, 0.0, 0.2, 0.4, 0.6, 0.8, 1.0, 1.2, 1.5, 2.0.

Chapter 4

Event Selection

The idea of the analysis is to apply a set of cuts to get rid of as many background events as possible, while at the same time keeping the signal efficiency as large as possible. To achieve this, the background, and signal samples are used to maximize the significance defined in (4.1) [26], which gives the known S/\sqrt{B} in the $S \ll B$ limit.

$$Z_{llr} = \sqrt{2(s+b) \ln(1+s/b) - s} \quad (4.1)$$

Simulation cannot represent correctly the distributions of some quantities, therefore a background sample is deduced from data and its used to carry out some optimization studies.

4.1 Event Topology Cuts

In 4.1a one can see the distribution of the difference in rapidity, $\Delta_{y_{JJ}}$, between the boosted jets after a mass cut in the dijet mass was applied. This variable offers a strong discrimination between signal and background and is used as a selection cut. In 4.1b and 4.1c one can see the η distributions; this cut does not offer a strong discrimination, however the tracks associated with the jets will be used to increase the sensitivity of the analysis and therefore a cut at $|\eta| < 2$ has to be applied¹. Finally figure 4.1d shows the *momentum asymmetry* distribution in signal data and background, this variable does not offer any discrimination but is used to get rid of events in which one of the jets might have been reconstructed incorrectly, only events with an asymmetry lower than 0.15 are accepted. In all the distributions the background normalization was obtaining by fitting the background to the data. The signal was normalized in such a way that its largest bin agrees with the data's largest bin.

As mentioned before, the $\Delta_{y_{JJ}}$ variable offers a high discriminating power and a cut between 1 and 1.5 should be applied. Figure 4.2a shows the event yield for the graviton signal with $m_G = 2000\text{GeV}$ for a window of a given lower and upper edge in $\Delta_{y_{JJ}}$, the background yield is shown in 4.2b. From these event yields one can calculate the signal significance as defined by (4.1), which is shown in 4.2c. The lower edge of the window should be zero, so 4.2d shows

¹The Inner detector goes all the way to $|\eta| < 2.5$ however 2 was chosen given the large radii of the jets used.

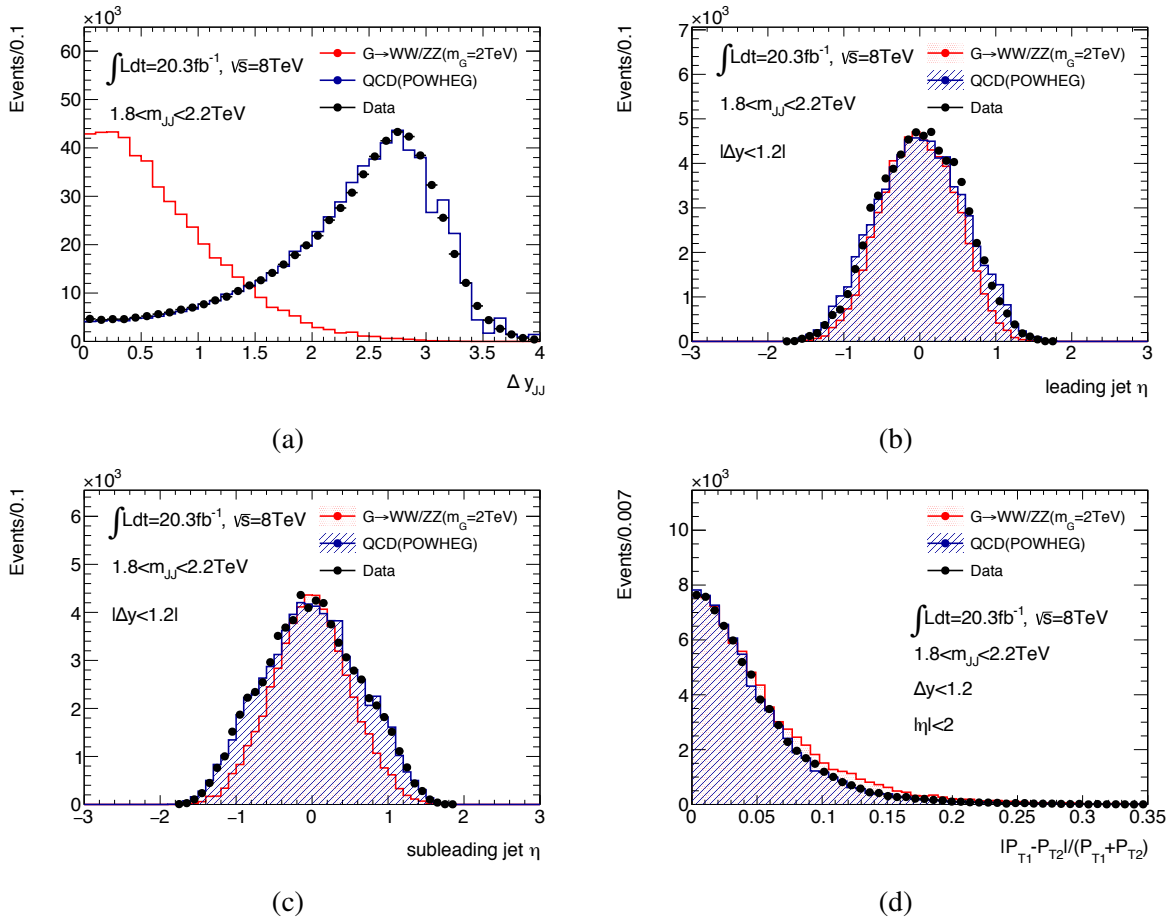
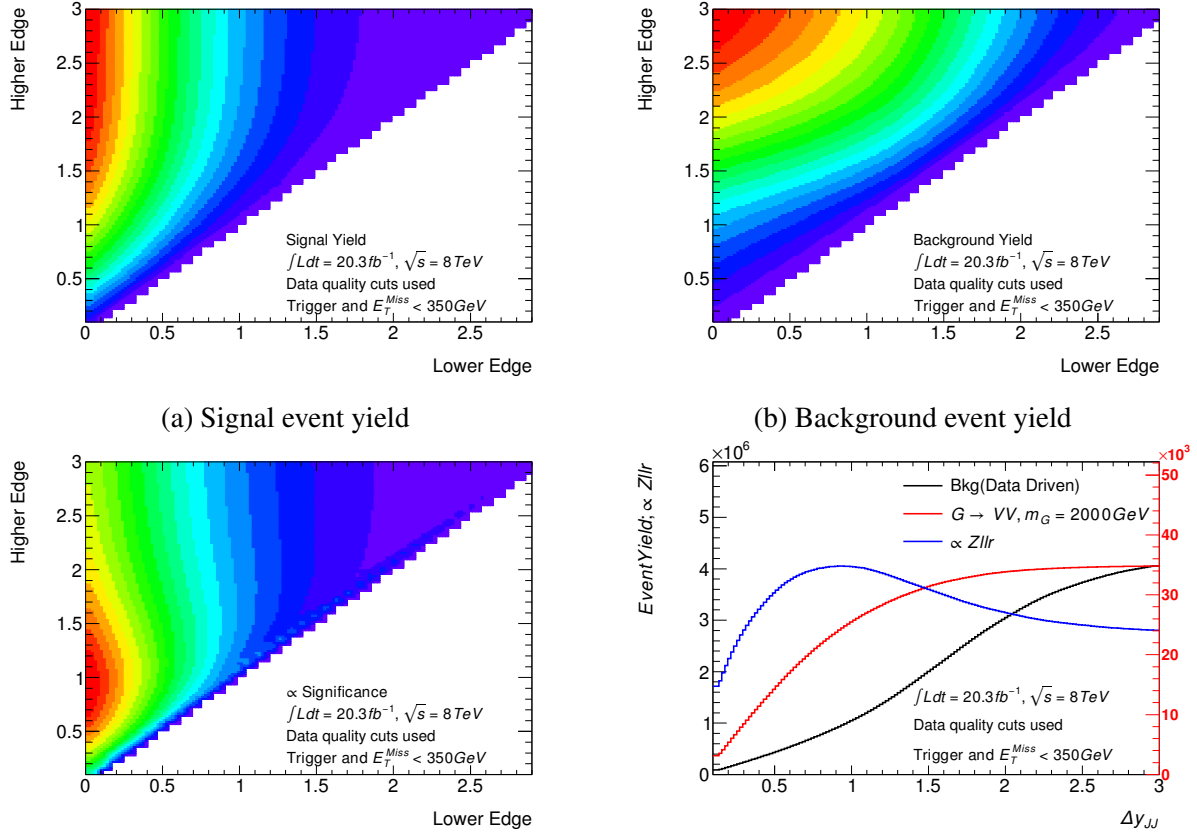


Figure 4.1: Comparison of the distributions of different quantities between data and simulation. The signal was normalized in such a way that the peak of the histogram agrees with the data. The background was fitted to the data.

a slice at this value for the signal yields and the significance. The optimal value seems to be between 0.9 and 1 a conservative cut at 1.2 is applied.



(c) Significance calculated from (a) and (b) following (4.1).

(d) Slice of (a), (b) and (c) for which the lower edge is zero

Figure 4.2

The optimal value for this cut seems to be very stable with respect to the resonance mass. Figure 4.3 shows the optimal value in function of the mass point for the RS1 graviton and EGM W' signals.

4.2 Boson Tagging

Three quantities have been used to discriminate between jets originating from a boson and jets originating from a gluon or a quark: the filtered jet's mass, the momentum balance and the number of tracks associated with the ungroomed jet.

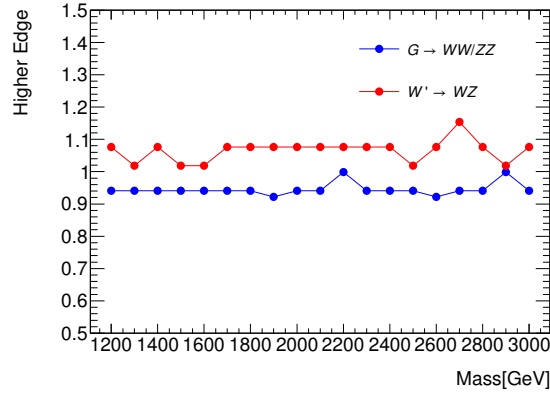


Figure 4.3: Comparison of the optimal cut in Δy_{JJ} for a $G \rightarrow WW/ZZ$ and a $W' \rightarrow WZ$ signals.

4.2.1 Momentum Balance

This variable offers a strong discrimination between signal and background, figure 4.4 shows its distribution for the background, modeled with PYTHIA, and the Graviton signal decaying in both WW and ZZ channels.

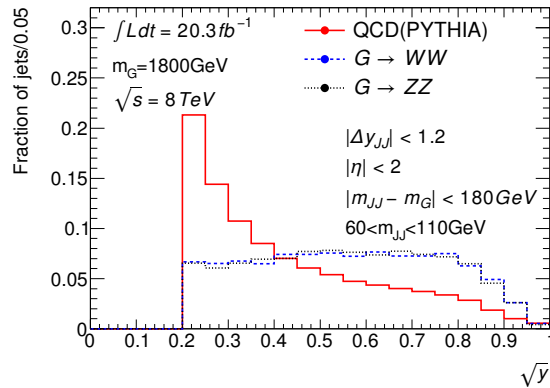


Figure 4.4: Distribution of the momentum balance for QCD background and graviton signal.

Based on the distributions obtained for several mass points a cut at $\sqrt{y} > 0.45$ was chosen.

4.2.2 Ungroomed Jet's Number of Tracks

As was mentioned in chapter 3 the tracks are included as jet constituents during the clustering process used to build the C/A 1.2 jet. However their momentum is made negligible in order not to double count their energy, which is already accounted when using the calorimeter clusters. This allows to associate to a jet a list of tracks in what is called *ghost association*. Figure 4.5a shows the distribution of the number of tracks associated to the ungroomed jets for signal and NLO background.

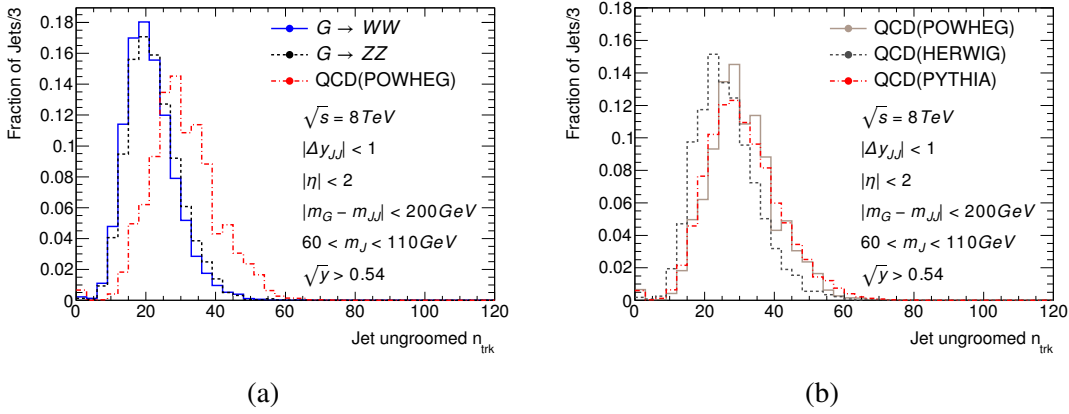


Figure 4.5: Figure (a) shows the distribution of the number of tracks associated to the ungroomed jets for a Graviton signal with $m_G = 2\text{TeV}$. Figure (b) shows the same distribution but comparing only QCD background.

The background distribution appears to be consistently higher than data, however there is a noticeable disagreement between PYTHIA, Herwig and Powheg as figure 4.5b shows. This is another observable that simulation cant simulate correctly and a conservative cut at $n_{trk} < 30$ is used.

4.2.3 Uncertainty on the efficiency of the cut on the ungroomed jet's number of tracks

After applying the cut on the number of tracks to the signal a given efficiency will be obtained. However the efficiency expected in data is not know and is possibly quite different. In order to assess the effect of this cut on data a W/Z + jets sample was extracted from data. This sample was fitted to a Crystal Ball function² plus a polynomial used to model the background.

The data used was required to pass the trigger a Δy_{JJ} cut, a $\sqrt{y_f} > 0.45$ cut and the leading jet in p_T was required to satisfy $0.58 < p_T < 0.68\text{TeV}$. The signal (W and Z bosons) efficiencies were extracted from this fit for different cuts on n_{trk} . Figure 4.6 shows two of these fits for a $n_{trk} = 30$ cut.

²A gaussian with an exponential tail on the left side. However an exponential tail was also used for the right side.

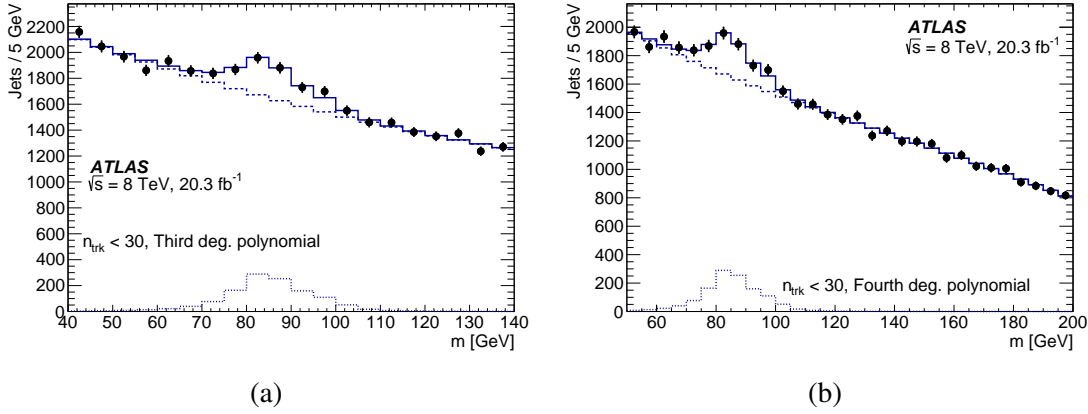


Figure 4.6: Figure (a) shows the fit of the $V + jets$ distribution in data to a Crystal Ball plus third polynomial PDF, (b) shows the same fit but with a fourth degree polynomial PDF.

The fit was done using a Bayesian approach, i.e. by maximizing the posterior. The posterior distribution for the signal yield is used to build the PDF describing the efficiency of the n_{trk} cut. The background can be modeled with a third (BG3) or fourth degree (BG4) polynomial. In each case a different posterior is obtained and therefore a different PDF for the efficiency of the n_{trk} cut. These PDF's are added and the result fitted to a truncated gaussian described by (4.2)

$$G_t(\epsilon|\epsilon_0, \sigma_\epsilon, \epsilon_{\max}) = \begin{cases} 0, & \epsilon < 0 \\ Ke^{-\frac{(\epsilon-\epsilon_0)^2}{2\sigma_\epsilon^2}}, & 0 \leq \epsilon \leq \epsilon_{\max} \\ 0, & \epsilon > \max \end{cases} \quad (4.2)$$

where $\epsilon_0 = 0.83$, $\sigma_\epsilon = 0.09$ and $\epsilon_{\max} = 1$. Figure 4.7 shows the PDF's corresponding to the fits using BG3 and BG4, also it shows the fit to their combination. Following the same procedure with simulated $W/Z+jets$ samples generated with PYTHIA one obtains an efficiency of 0.947. Therefore simulation overestimates the efficiency and (4.2) needs to be scaled. The PDF describing this scale is (4.3), where $S_0 = 0.89$, $\sigma_S = 0.095$ and $S_{\max} = 1.07$.

$$P(S) = G_t(S|S_0, \sigma_S, S_{\max}); \quad (4.3)$$

4.2.4 Filtered Jet's Mass

The mass distribution of the groomed and filtered jets for $G \rightarrow WW/ZZ$ and dijet QCD are shown in 4.8a where it is evident that the filtered jet's mass is a very strong discriminant that can be used to tag jets as W or Z bosons. Given the poor modeling of the jet mass provided by the simulation, a background sample was extracted from data to carry out this optimization. From the data a distribution of the mass of the tagged (cut on \sqrt{y} and n_{trk}) jet is obtained in events in which the other jet is not tagged as a W or Z boson.

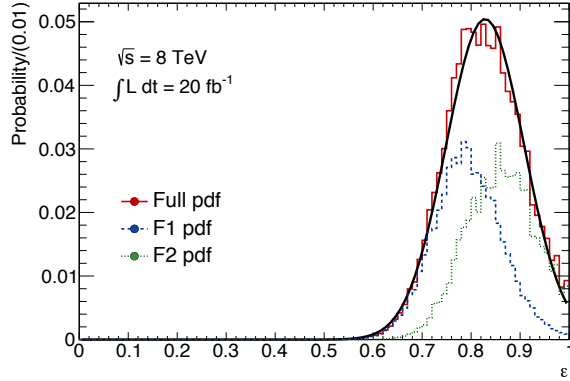


Figure 4.7: PDF describing the efficiency of the n_{trk} cut for the BKG3 and BKG4 background parametrizations. Their combination is shown in red.

Events belonging to different p_T slices are used to optimize the cut for different mass points. In order to do it the simulated Graviton mass distribution is fitted to a Breit-Wigner distribution and only the events in a 200GeV window are chosen. These events are used to form the p_T distribution of both jets which is subsequently fitted to a gaussian PDF. The p_T slice chosen is within 2σ of the mean, μ , of the distribution. The fit of the graviton mass to a Breit-Wigner distribution and the p_T distribution to a gaussian PDF are shown in figure 4.10 for a given mass point.

$$f(x) = C_0 e^{C_1 \cdot x + C_2 \cdot x^2} \quad (4.4)$$

The events in each p_T slice are fitted to (4.4). This fit is subsequently used to draw randomly values representing the masses of the jets belonging to the data-driven background. This fit is necessary specially in the high p_T slices, where the statistics are poor.

The mass distribution representing the signal is taken from simulation. A sample of tagged jets is extracted after the systematics are applied to each event. As was discussed in section 3.5 the jet mass resolution adopted was 7.5% of the jet mass. Also the uncertainty in all the resolutions was agreed to be the quantity that increases the resolution by 20%, therefore the uncertainty can be extracted as shown in (4.5)

$$\sigma_{total} = 1.2 \cdot \sigma_{nominal} = \sqrt{\sigma_{unc}^2 + \sigma_{nominal}^2} \Rightarrow \sigma_{unc} = \sigma_{nominal} \cdot \sqrt{1.2^2 - 1} \quad (4.5)$$

which for the mass resolution gives $\sigma_{unc} = 4.97\%$. This is taken as the standard deviation of a gaussian PDF used to smear the jet mass distribution. To take into account the p_T scale one shifts the jet mass up and down by 3%, randomly for each event, all this is shown in (4.6).

$$m'_j = m_j \cdot (1 \pm 0.3) + m_j \cdot G(x|0, 0.0497) \quad (4.6)$$

The mass distribution before and after the systematics are shown in figure 4.9 for a given mass point.

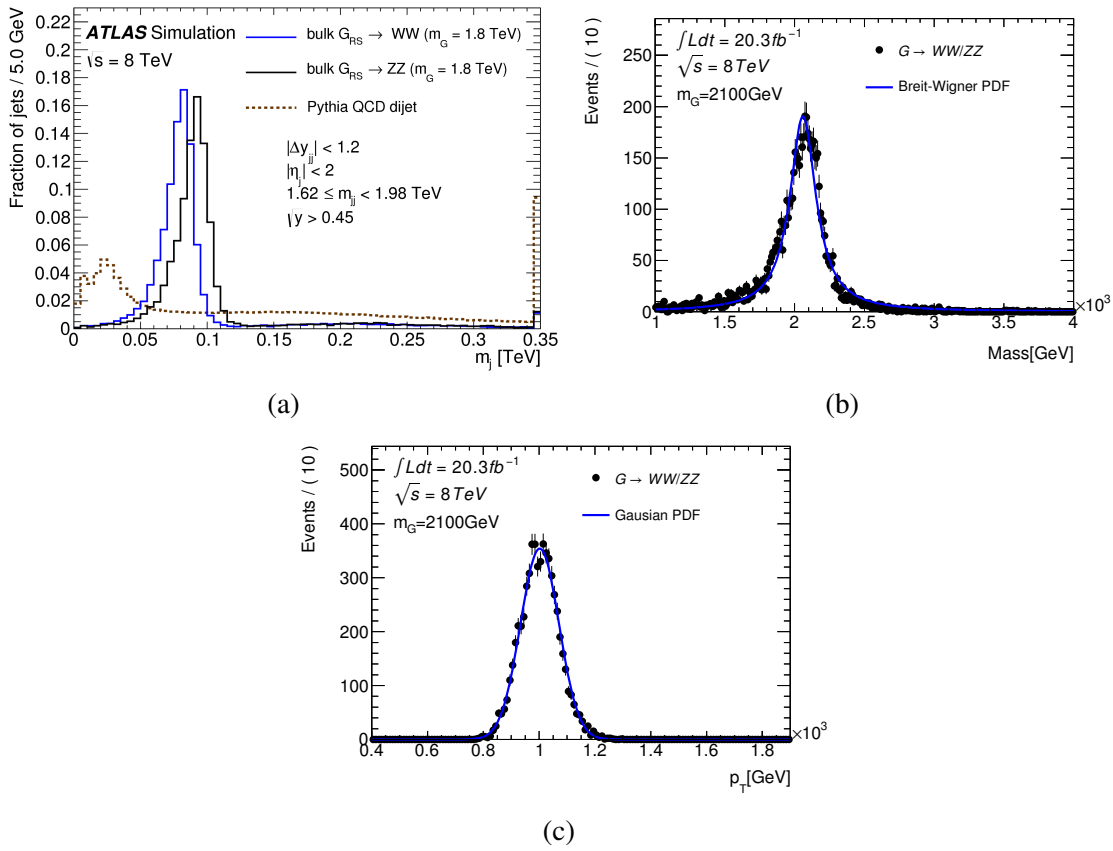


Figure 4.8: Figure (a) shows the mass distributions for W jets, Z jets and QCD jets. In (b) the graviton mass distribution is fitted to a Breit-Wigner PDF in order to determine the events that will go into the distribution in (c). From (c) will be obtained the values of the p_T slices used for the mass window optimization.

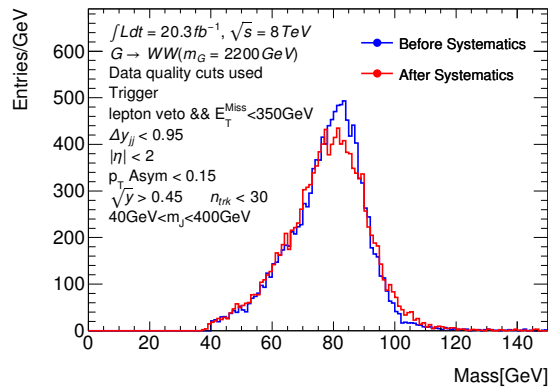


Figure 4.9: The figure shows the jet mass distributions for a $G \rightarrow WW$ with $m_G = 2200$ GeV before and after the systematics were applied.

The optimization was carried out by calculating the significance corresponding to each mass window in a grid, as was done for the Δy_{JJ} cut.

For a given graviton mass point figure 4.10a shows the event yield for the background for each point in the grid, 4.10b shows the signal yield, 4.10c the significance and 4.10d shows the overlay of a section of the three plots.

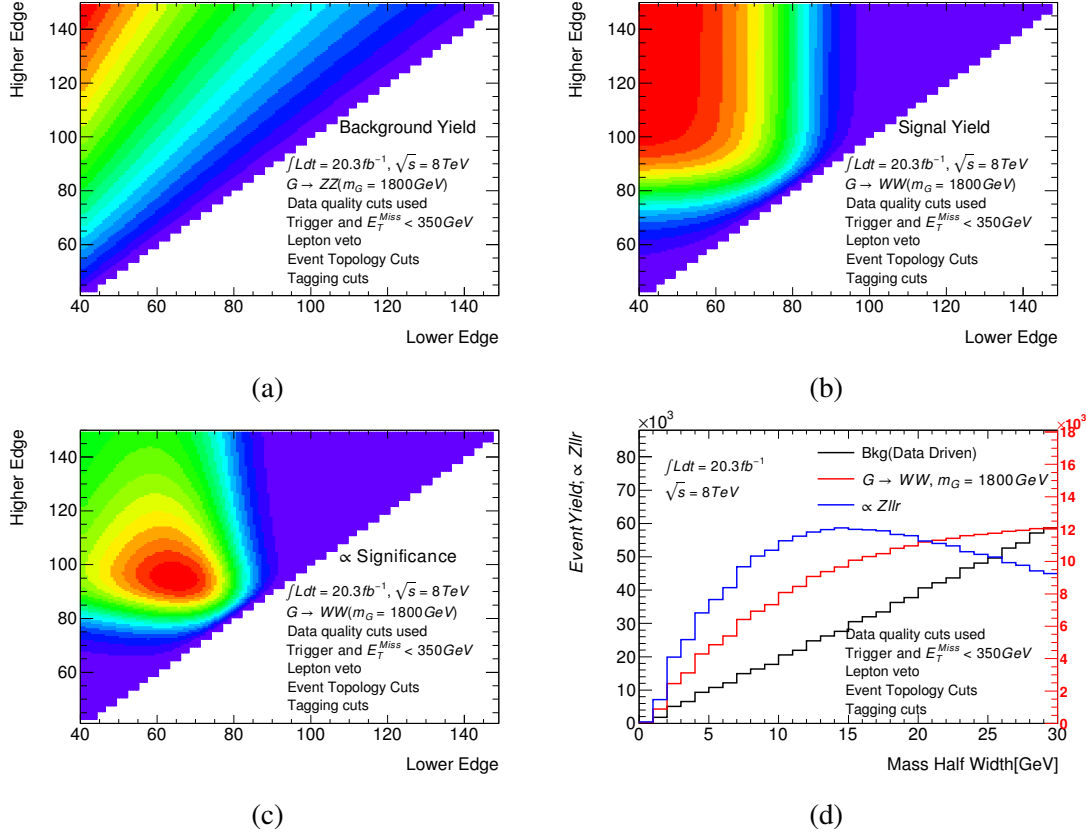


Figure 4.10: Figure (a) shows the background yield for many combinations of the higher and lower edge of the mass window. (b) shows the same but for the signal yield. Using (a) and (b) the significance is obtained for each point in (c). Figure (d) shows how the signal and background yields and the significance behave with different half widths and placing the center of the window at the mass of the W boson.

Based on the plots a value of 13GeV is chosen for the half width of the mass window, for both the WW, WZ and ZZ channels.

4.3 Event Selection Summary

Table 4.1 shows the cuts used to get the final dijet mass spectrum, where the efficiency is with respect to the last cut. Additionally figure 4.11a shows the efficiency for different graviton and

W' masses after applying cuts on observables related to the event topology. Figure 4.11b shows the same when furthermore the tagging cuts are applied. The final selection efficiency is of about 10%. The strongest discriminants are the difference in rapidity and the jet mass.

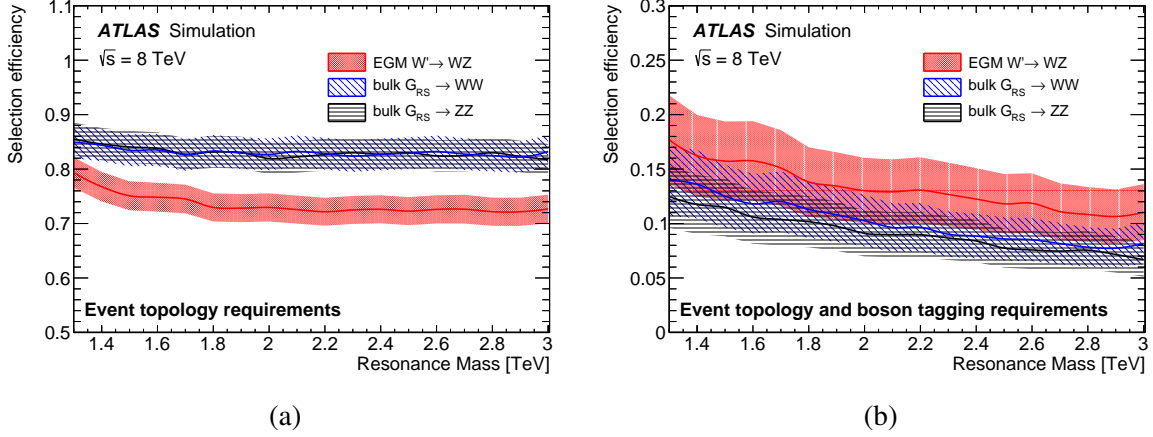


Figure 4.11: In (a) is shown the efficiency related to the event topology cuts for both a $W' \rightarrow WZ$, a $G \rightarrow WW$ and a $G \rightarrow ZZ$ signal and for different mass points. Figure (b) shows the efficiency after the boson tagging cuts are additionally applied.

		1.2 TeV Eff. [%]		1.8 TeV Eff. [%]		2.4 TeV Eff. [%]		3.0 TeV Eff. [%]	
	<i>Data</i>	$G^{(WW)}$	$G^{(ZZ)}$	$G^{(WW)}$	$G^{(ZZ)}$	$G^{(WW)}$	$G^{(ZZ)}$	$G^{(WW)}$	$G^{(ZZ)}$
Pre-selection	8510451	90.0	86.7	93.2	92.9	91.6	90.7	90	85.8
2 filtered jets	8387735	90.0	86.7	93.2	92.9	91.6	90.7	89.9	85.7
$ \Delta y_{12} < 1.2$	5023199	77.2	74.2	77.4	77.0	75.7	74.6	74.9	70.2
$ \eta < 2$	4981723	77.2	74.2	77.4	77.0	75.7	74.6	74.9	70.2
$A < 0.15$	4069018	69.4	64.3	71.5	69.0	71.6	68.7	71.8	65.6
Tag (WW)	1467	12.4	6.3	10.6	6.8	8.8	5.9	8.7	5.4
$m_{jj} > 1.05\text{TeV}$	423	12.1	6.0	10.5	7.1	8.7	5.9	8.5	5.4
Tag (ZZ)	1205	5.1	10.2	4.2	9.1	3.5	8.1	3.5	6.7
$m_{jj} > 1.05\text{TeV}$	336	4.9	9.9	4.1	9.1	3.5	8.0	3.4	6.6

Table 4.1: Event Selection Summary

Chapter 5

Statistical Analysis

The statistical analysis consists of comparing the shape of the data with the shape of the background estimate and the predicted signal. This is done by using bins of 100GeV and starting the analysis at 1050GeV, where the trigger becomes fully efficient.

The final result is the calculation of the upper limits on the cross section times the branching ratio at 95% confidence level and the significance of any excess present in the dijet mass distribution found after applying the event selection cuts.

5.1 Background Estimate

The background, as mentioned in chapter 4 is dominated by QCD dijet events with small amounts of $W/Z + jets$ and WW/ZZ events. This background is supposed to decrease with the dijet mass and therefore a smoothly decreasing function can be used to parametrize it. The background was estimated by fitting the data to (5.1) where p_2 and p_3 control the shape and 4.3 was chosen in order to de-correlate them. The fit is done by minimizing the negative log likelihood and is carried out using RooFit. In case of the presence of signal a bias, proportional to the size of the resulting bump, would be expected.

Many background parametrizations were tried and all were seen to agree. By estimating the background in this way the associated nuisance parameters are p_2 , p_3 and the number of background events, embedded in the proportionality constant of (5.1).

$$B(p_2, p_3) \propto (1 - x)^{p_2 + 4.3p_3} \cdot x^{p_3} \quad (5.1)$$

5.2 Signal Hypothesis

The signal templates are taken from simulation and then smeared and scaled to take into account the systematic uncertainties. The uncertainty on the signal shape depends on the p_T scale uncertainty ($\alpha_{p_T}^{scale}$, which is the main nuisance parameter determining the location of the signal's peak), the uncertainty on the p_T resolution ($\alpha_{p_T}^{reso}$ which controls the width of the peak) and the

uncertainty on the jet mass scale ($\alpha_{m_J}^{scale}$). The uncertainty on the signal normalization is propagated from the uncertainties on the resolutions of \sqrt{y} ($\alpha_{\sqrt{y}}^{reso}$), m_J ($\alpha_{m_J}^{reso}$), the \sqrt{y} scale ($\alpha_{\sqrt{y}}^{scale}$)... but most importantly from the uncertainty of the efficiency of the cut on the number of tracks associated to an ungroomed jet ($\alpha_{n_{trk}}^{eff}$) as can be seen in table 5.1.

Source	Normalization Uncertainty %
Efficiency on n_{trk} cut	17
m_J resolution	5.5
\sqrt{y} scale	3.5
\sqrt{y} resolution	2.0
Parton shower modeling	5.0
PDF	3.5
Luminosity	2.8

Table 5.1: Impact of different sources of systematics on the signal normalization uncertainty.

As was mentioned in chapter 4 the efficiency of the n_{trk} cut is 0.89 and its uncertainty is 9.5%. This implies that the efficiency for passing an **event** should be 0.80 and the uncertainty about 17%.

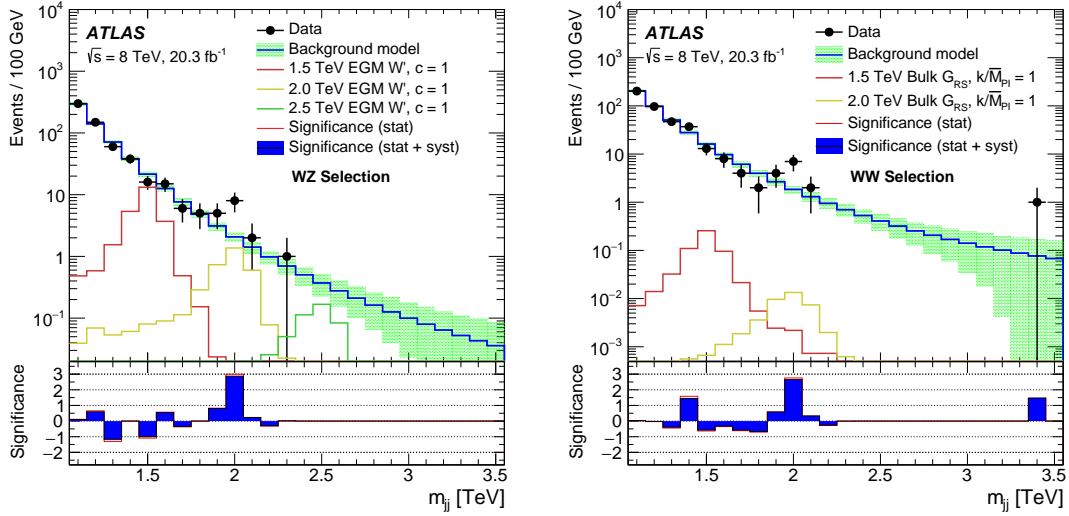
All the systematic uncertainties that affect the signal normalization are assumed to be uncorrelated, and therefore can be added in quadrature to give a total normalization uncertainty of 19.5%.

In order to parametrize the signal as a function of the three scales mentioned a set of templates was created for each combination of the nuisance parameters. Therefore each bin in the dijet mass distribution is a function of the nuisance parameters. The function is found by fitting a polynomial of up to fourth degree ¹ and in this way building a parametrized PDF with three nuisance parameters, $\alpha_{p_T}^{reso}$, $\alpha_{p_T}^{scale}$ and $\alpha_{m_J}^{scale}$.

5.3 Dijet Mass Distribution

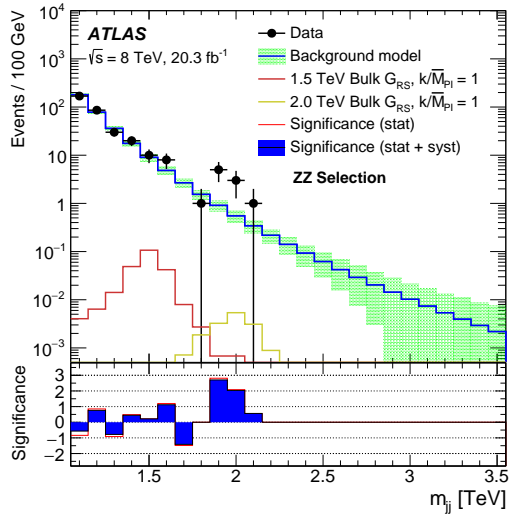
Figure 5.1a, 5.1b and 5.1c show the dijet mass spectrum in data after all the cuts described in chapter 4 were applied. These mass distributions are shown with the expected background and three signal hypotheses normalized to their cross sections. Below each of these plots is shown the local significance plot, calculated by using the data and the background estimation. The blue histogram shows the significance taking into account both the statistical uncertainty on the background estimate and the uncertainty coming from the fit, while the red histogram takes into account just the statistical uncertainty. An excess of events at around 2TeV is clearly visible.

¹This was done with the TMultiDimFit class, belonging to ROOT.



(a)

(b)



(c)

Figure 5.1: Figure (a) shows the background estimate in blue, the data in black and three different W' signal hypotheses in red, yellow and green. Figures (b) and (c) contain the same information but after applying the WW and ZZ selection cuts with $G \rightarrow WW$ and $G \rightarrow ZZ$ signal hypotheses respectively.

5.4 Model

In order to get limits, extract p-values and in general fit and compare the null and alternative hypothesis with the data one needs to build a model with the signal, background and data. As mentioned above the analysis will be carried out by binning all the templates, therefore we use a binned likelihood defined as (5.2)

$$\mathcal{L} = \prod_{i=1}^{n_{bins}} P(\mu s_i k + b_i, d_i) = \prod_{i=1}^{n_{bins}} \frac{(\mu s_i k + b_i)^{d_i} e^{-(\mu s_i k + b_i)}}{d_i!} \quad (5.2)$$

where b_i , s_i and d_i are respectively the amount of background, signal and data in bin i , while μ and k represent the signal strength and the signal normalization. $P(\mu s_i k + b_i, d_i)$ is the probability that for the bin i one observes d_i events in data when one expects $\mu s_i k + b_i$.

Each bin in the signal template is (as is the signal itself) a function of three nuisance parameters. From studies in simulation, mentioned in chapter 4, in the systematics section, one can constrain these quantities, given the uncertainties that one obtained. This is implemented by multiplying the likelihood by PDF's as shown in (5.3), where the dependence of the likelihood on the nuisance parameters has been made explicit.

$$\begin{aligned} \mathcal{L}'(\alpha_{p_T}^{reso}, \alpha_{p_T}^{scale}, \alpha_{m_J}^{scale}, k) &= \mathcal{L}(\alpha_{p_T}^{reso}, \alpha_{p_T}^{scale}, \alpha_{m_J}^{scale}, k) \cdot G(\alpha_{p_T}^{scale} | 0, 0.02) \cdot G(\alpha_{p_T}^{reso} | 0, 0.033) \cdot \\ &G(\alpha_{m_J}^{scale} | 0, 0.02) \cdot L(k | 0.8, 0.195) \end{aligned} \quad (5.3)$$

$G(x|\mu, \sigma)$ represents a gaussian PDF that depends on x , has a mean μ and a standard deviation σ . $L(x|\mu, \sigma)$ represents the same but for a log-normal PDF and is used to constrain the normalization scale.

No previous knowledge of the background is assumed, therefore p_2 and p_3 are not constrained.

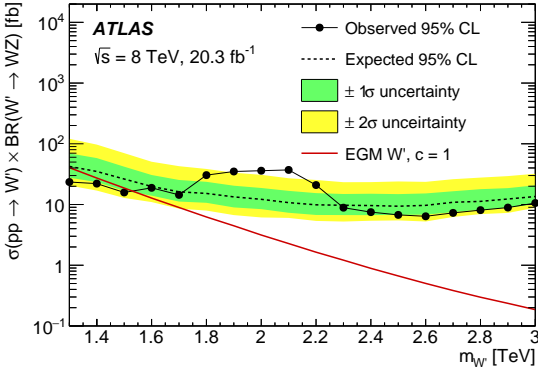
5.5 Limits and p_0

The limit setting procedure was carried out using a frequentist approach with the tools provided by RooStats [27] and RooFit [28]. The test statistic used for the limits was the one-sided profile likelihood [29]² defined in (5.4) as:

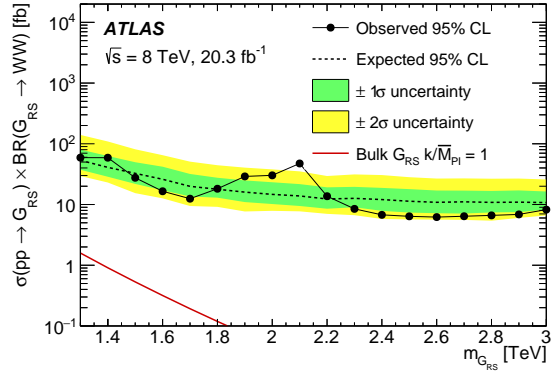
$$q_\mu = \begin{cases} -2 \ln \lambda(\mu) & \hat{\mu} \leq \mu, \\ 0 & \hat{\mu} > \mu, \end{cases} \quad \lambda(\mu) = \frac{L(\mu, \hat{\theta})}{L(\hat{\mu}, \hat{\theta})} \quad (5.4)$$

Where \hat{x} is the estimator of x , i.e. the value for which the likelihood reaches its maximum. μ represents the parameter of interest and θ the nuisance parameters. The denominator of $\lambda(\mu)$ is what is called an *unconditional* likelihood and the numerator is a *conditional* likelihood; named in this way because its parameter of interest, μ , is fixed to a given value before carrying out the

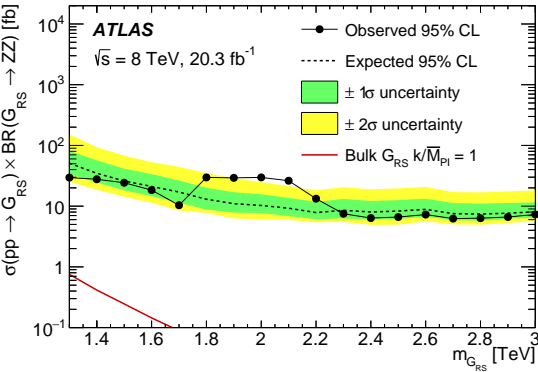
²Implemented in the RooStats class ProfileLikelihoodTestStat.



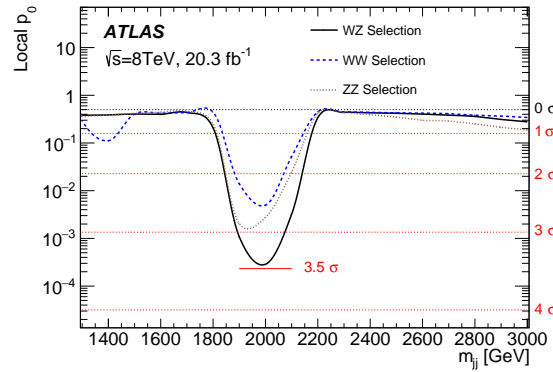
(a) Upper limits at 95%CL on $\sigma \cdot B$ for an EGM W' signal. The theory prediction is plotted in red.



(b) Upper limits at 95%CL on $\sigma \cdot B$ for an RS1 $G \rightarrow WW$ signal. The theory prediction is plotted in red.



(c) Upper limits at 95%CL on $\sigma \cdot B$ for an EGM $G \rightarrow ZZ$ signal. The theory prediction is plotted in red.



(d) Local significance for the WW , WZ and ZZ event selections.

Figure 5.2

maximization, which in turn gives the $\hat{\theta}$ values for the nuisance parameters. The numerator of $\lambda(\mu)$ will be always smaller or equal than the denominator, so q_μ adopts values in $[0, \infty]$. After fitting the model to a dataset one should get, a value $\hat{\mu}$ for the parameter of interest, q_μ will be large if this value disagrees strongly with μ .

In order to quantify the agreement of the background and the signal plus background models with the data one generates toys from these models and builds their q_μ distribution. μ is set to zero if one is trying to obtain p_0 , the degree of agreement of the data with the background model. (5.5) defines p_0 , where $f_b(q_0)$ represents the distribution of the test statistic (5.4) for the background model and q_0^{data} is the value corresponding to the data.

$$p_0 = \int_{q_0^{data}}^{\infty} f_b(q_0) dq_0 \quad (5.5)$$

From p_0 one can define the significance (different from what was used in chapter 4) as (5.6) where Erf^{-1} is the inverse of the error function.

$$\sigma_{sig} = \sqrt{2} \text{Erf}^{-1}(1 - 2p_0) \quad (5.6)$$

On the other hand during the limit setting procedure one tests the agreement of the data with the signal plus background model scanning different values of μ until a 95% confidence level is reached

Figure 5.2 shows the upper expected and observed limits on the $\sigma \cdot BR$ for an Extended Gauge Model W' decaying into a WZ pair and an RS1 graviton decaying into a WW or ZZ pair. All the channels show an excess at around 2TeV. The largest significance is obtained for the WZ channel with a value of $\sigma_{sig} \approx 3.4$. Upper limits can be set in all the channels, but only for the W' signal one can rule out the presence of signal for a mass of 1.3TeV, 1.4TeV and 1.5TeV. The predicted graviton cross section is for most of the mass points two orders of magnitude below the sensitivity of the analysis.

5.5.1 Look Elsewhere Effect (LEE)

Given the large significance obtained one has to consider the fact that one is searching for a possible signal everywhere in the range $1050 < m_{JJ} < 3550\text{GeV}$ and therefore the probability of finding an excess is larger than if one selected the mass point initially and looked only there. The $\sigma_{sig} \approx 3.4$ obtained in the last section will decrease once one takes into account the LEE. In order to implement this, reference [30] will be followed. Reference [30] develops an asymptotic formula to get the probability of observing an excess anywhere in the spectrum of the observable (the dijet mass in our case). The degree with which the LEE dilutes the local significance (3.4σ in our case) depends on the potential of the background to *develop* excesses. This can be quantified by generating toys and plotting the distribution of the q_0 test statistic. As discussed before q_0 represents the amount of agreement of the toy with the background. Therefore whenever the background has an excess q_0 gets farther from zero. Reference [30] parametrizes q_0 in function of the observables, which in our case is just the mass. A measure of the potential of the background

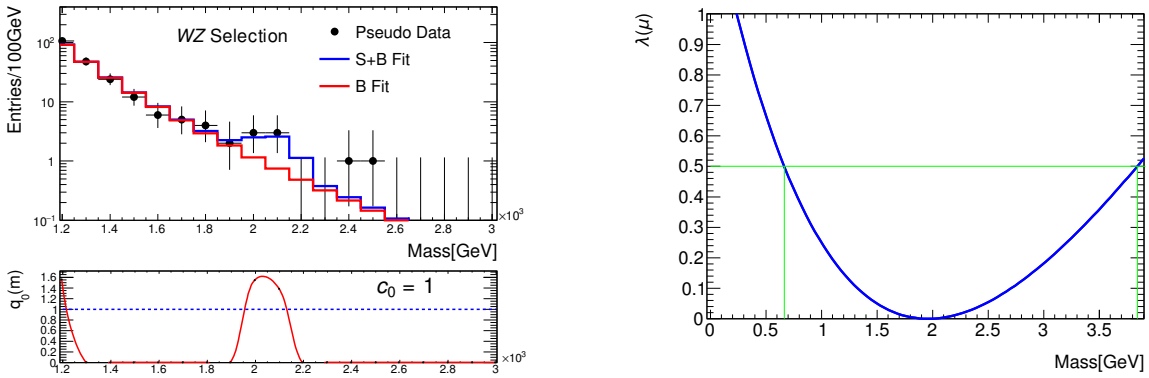
to produce fake excesses can be the number of times $q_0(m)$ crosses an upper boundary, c_0 , i.e. the number of up-crossings.

The formula that reference [30] uses to estimate the probability of an excess arising anywhere in the spectrum of the observable is (5.7), where χ_s^2 is a chi-square distribution with s degrees of freedom, here taken as equals to one, the mass. c_0 is the up-crossing level, $\langle N(c_0) \rangle$ is the average number of up-crossings, c is the square of the significance.

$$P(q(\hat{\theta}) > c) \leq P(\chi_s^2 > c) + \langle N(c_0) \rangle \left(\frac{c}{c_0}\right)^{(s-1)/2} e^{-(c-c_0)/2} \quad (5.7)$$

(5.7) offers an upper bound but is assumed to be a good approximation of p_0 . Therefore the uncertainty in the estimate of the global p_0 depends on the uncertainty of $c = \sigma_{local}^2$ and $\langle N(c_0) \rangle$. The last factor depends on the number of toys used, which is of order 10^2 .

Figure 5.3a shows one of the sets of pseudo data corresponding to the WZ selection fitted to the signal plus background model, the background component is also shown. Below this, the value of the test statistic q_0 in function of the signal mass is also shown. One can see that the pseudo data has an excess at 1.2TeV and around 2TeV, which gives us one up-crossing with a $c_0 = 1$. The corresponding $\lambda(\mu)$ with the 68% confidence level, symbolized by the green lines, is shown in 5.3b.



(a) Best fit of the pseudo-data to the signal plus background model in blue. The background component is shown in red.

(b) Profile likelihood in function of the signal strength corresponding to the fit in (a).

Figure 5.3

The distribution of the up-crossings is obtained from an ensemble of 100 toys, from which one chooses the average. This is used to calculate the global significance for the WZ selection which gives us 2.5σ . Lower significances are expected for the WW and ZZ channels.

Chapter 6

Electromagnetic Calibration

6.1 Introduction

The LAr calorimeter was briefly described in chapter 2. It is known that there is a discontinuity in the values of a particular constant used to calculate the energy that the cell measures, $M_{\text{phys}}/M_{\text{cal}}$. It is assumed that a cell can be modeled as an RLC circuit [31] and in this chapter the origin of this discontinuity is traced to its resonance frequency measurement. It is known that the detector cells cannot be modeled accurately as RLC circuits in the End Cap [32], therefore currently no attempt is made to extract the resonance frequency for most of the strips and the back layer. Suggestions about possible values that this frequency can adopt in this part of the calorimeter are given.

Finally a search for unusually large or small values of these calibration constants is carried out and parts of the detector have been found where these values are suspicious and could be further studied. However it is uncertain whether these cells are miscalibrated.

As seen in chapter 2, the electromagnetic calorimeter cells translate into electric impulses the energy deposited by charged particles. Most of the time the energy deposited in a cell is not large, therefore when these electric impulses are amplified the amplifier works on high gain. Occasionally the energy deposited (coming from an energetic particle) is larger and the amplifier needs to work on medium or even high gain. All the plots in this chapter will deal with high gain.

6.2 Calibration Constants

The electromagnetic calorimeter of the ATLAS detector is designed to measure the energies of charged particles by measuring the amount of ionization generated in LAr (Liquid Argon), which is in contact with metallic plates at high voltage. The ionization charges induce a signal, which is amplified, shaped and sampled every 50 ns. The shaped signal is called the physics wave. The peak value of the physics wave is proportional to the particle's energy and the first stage of calibration is finding the proportionality constants.

The formula used to go from the peak of the physics wave to the measured energy is:

$$E_{cell} = F_{\mu A \rightarrow \text{MeV}} \cdot F_{\text{DAC} \rightarrow \mu A} \frac{1}{\frac{M_{\text{phys}}}{M_{\text{cal}}}} \sum_{i=0}^1 R_i \cdot A^i \quad (6.1)$$

In order to estimate the difference in the behavior of each cell a *fake* wave, called *injected* calibration wave is used. This wave, in contrast with the pulse generated by the passage of a particle, is a decreasing exponential and is introduced in the motherboard, not between the plates, where the ionization occurs. R_i , the ramps, are the proportionality constants between the calibration wave injected and what is measured after it goes through electronics [33]. The calibration and physics waves are shown below in (6.2) and (6.3) respectively:

$$g_{\text{inj}}^{\text{cali}} = (1 - f_{\text{step}}) e^{-\frac{t}{\tau_{\text{cal}}}} + f_{\text{step}} \quad (6.2)$$

$$g^{\text{phys}} = \left(1 - \frac{t}{T_d}\right) \theta(t) \theta(T_d - t) \quad (6.3)$$

This means that the peak of the calibration wave and the physics wave are not the same. The ramps are measured using the calibration injected wave. So a constant is necessary to get back the right value of the peak. The constant used is called $M_{\text{phys}}/M_{\text{cal}}$ and is shown in (6.1) as inversely proportional to the measured energy.

$M_{\text{phys}}/M_{\text{cal}}$ is supposed to take into account the non-triangular shape of the injected calibration wave and the fact it is injected in the motherboard and not at the plates. The part of the detector between these points can be modeled as an RLC circuit, as shown in Figure 6.1.

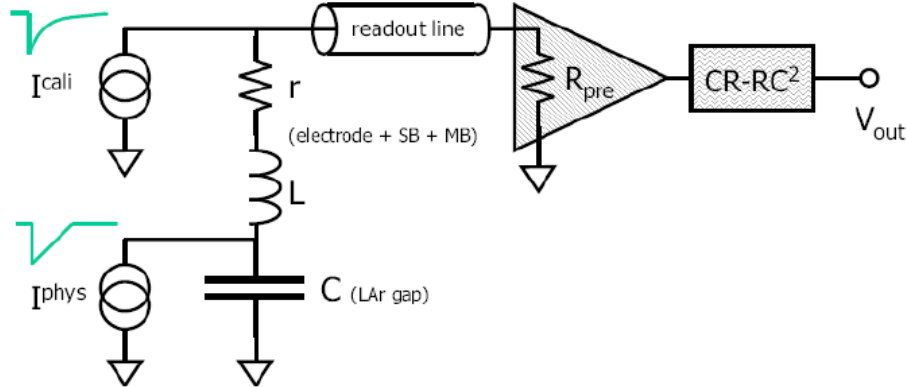


Figure 6.1: Diagram of a LAr calorimeter cell. RLC circuit that models the detector cell, followed by a transmission line, an amplifier (triangle) and a shaper (rectangle).

Because of all of this $M_{\text{phys}}/M_{\text{cal}}$ is a function of all the constants in (6.2) and (6.3) and of the quantities used to model the RLC circuit, $\omega_0 = 1/\sqrt{LC}$ and $\tau_r = RC$, and it is obtained using (6.4) in the time domain, where $\omega_0 = 1/\tau_0$. Issues have been found with ω_0 , and their values will be analyzed in the front layer of the barrel.

$$g^{\text{phys}}(s) = g^{\text{cali}}(s) \frac{(1 + s\tau_{\text{cali}})(sT_d - 1) + e^{-sT_d}}{sT_d(f_{\text{step}} + s\tau_{\text{cali}})} \frac{1}{1 + s\tau_r + s^2\tau_0^2} \quad (6.4)$$

$M_{\text{phys}}/M_{\text{cal}}$ is a function of ω_0 , the resonance frequency of the RLC circuit of figure 6.1. Consequently the impedance between ground and the circuit for the frequency components of the injected calibration wave that are close to ω_0 should be lower than the impedance for the frequency components far from ω_0 . Therefore ω_0 should appear as a minimum of the calibration wave in the frequency domain.

There are many problems with this idea. First, the circuit is not made only of the RLC part, but it is followed by elements that cannot be easily modeled, this can distort a clear minimum. Second, the part of the detector that has been modeled as an RLC circuit does not necessarily have to behave like that. Finally part of the injected calibration (and physics) wave can propagate to the neighboring cells (cross talk) and this can also affect the shape of the wave [34].

The default method used to get ω_0 is the Cosine Response [31]. It consists in deconvolving from the calibration wave the injected calibration signal, so that what results is the transfer function of the circuit; then a cosine function of a given frequency is convolved, these two steps are carried out by convolving the calibration wave with (6.5).

$$f_{\text{tran}}^{\text{cos}}(t, \omega) = \mathcal{L}^{-1} \left\{ \frac{s}{s^2 + \omega^2} \frac{s(1 + s\tau'_{\text{cali}})}{s\tau'_{\text{cali}} + f'_{\text{step}}} \right\} \quad (6.5)$$

τ'_{cali} and f'_{step} are extracted using a method called Step Response. The first factor inside the curly brackets is the Laplace Transform of the cosine that is injected and the second factor is one divided by the Laplace Transform of (6.2), the result of the convolution is $X(\omega, t)$. However the transfer function of the shaper (figure 6.1) is known, it is given by (6.6) [35] with $\tau_{sh} \approx 15\text{ns}$ and can also be deconvolved. In this way ω_0 is found, where (6.7) reaches its minimum where $X'(\omega, t) = X(\omega, t)/|H_{\text{shaper}}(\omega)|$.

$$H_{\text{shaper}}(\omega) = \frac{i\omega\tau_{sh}}{(1 + i\omega\tau_{sh})^3} \quad (6.6)$$

$$Q^2(\omega) = \sum_{t > T_{\text{tail}}} X'(\omega, t) \quad (6.7)$$

6.3 Study of the Calibration Constants in the Barrel

6.3.1 Software Related Problems

Figure 6.2 shows the values of $M_{\text{phys}}/M_{\text{cal}}$ in the front layer of the barrel of the LAr calorimeter for side A.

A sudden discontinuity can be seen in the interval $0.8 < \eta < 1$, corresponding to slot 6, this is seen on both the A and C sides. As was discussed in the last section $M_{\text{phys}}/M_{\text{cal}}$ is a function of ω_0 and τ_r among other variables.

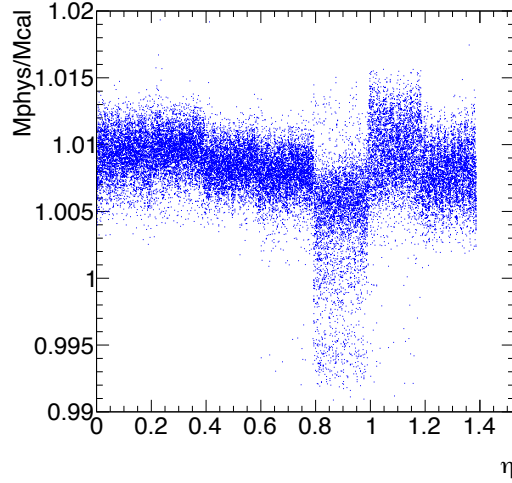


Figure 6.2: $M_{\text{phys}}/M_{\text{cal}}$ distribution in function of η in the front layer of the LAr barrel. The seven slots of the front layer (from 2 to 8) can be clearly distinguished.

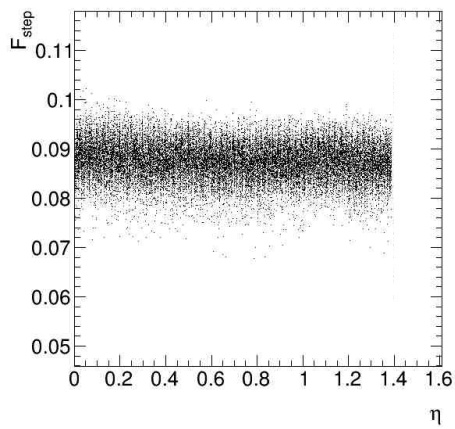
In figure 6.3 four of these constants have been plotted for the same part of the detector. Among these variables τ_r seems to have a smooth behavior everywhere except slot 6; however ω_0 is not smooth at all, its values change from one slot to the next one. Furthermore in slot 6, for many channels $\omega_0 = 0.33\text{GHz}$ exactly.

The problem was traced back to the interval in which the sum in (6.7) is performed. Figure 6.4 shows many $Q^2(\omega)$ curves for which the starting point in the sum was chosen to be 20ns and the end point (t_{end}) was increased in steps of 20ns from 150ns to 750ns. For small intervals $Q^2(\omega)$ is almost flat and as the interval increases the minimum moves and the features become more evident, by the time all the interval, from 20ns to 750ns is used, the location of the minimum and the shape of $Q^2(\omega)$ stabilize. The official code was supposed to use approximately that interval [32], but it was using the interval that starts where the wave rises, $\approx 20\text{ns}$, and ends where the wave becomes negative, $\approx 150\text{ns}$.

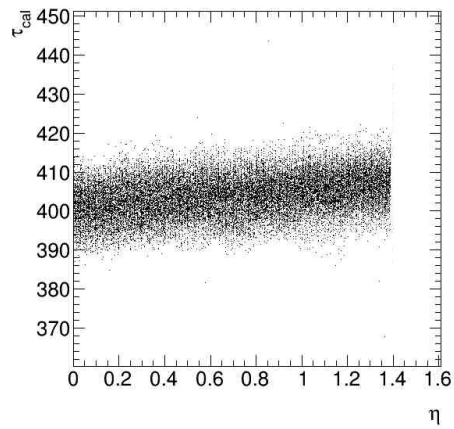
In order to find a minimum for $Q^2(\omega)$ an interval in frequency has to be selected, for the strips the interval used by the official code is $0.1 < \omega < 0.33\text{GHz}$. Figure 6.4 shows $Q^2(\omega)$, taken before any correction is applied (lowermost black curve). This curve has a minimum at 0.33GHz, which explains all the points in figure 6.3 located at this value. After the interval of the sum is changed the curve gets a minimum typically about 0.275GHz, like in the uppermost curves of figure 6.4.

6.3.2 Hardware Related Problems

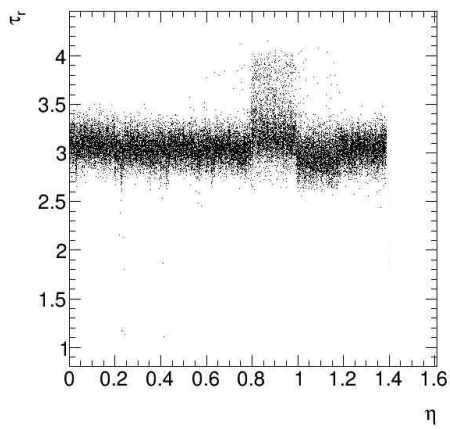
Figure 6.5 shows slots 2 to 7 in the front layer of the Barrel. The curves are reasonably similar to each other and show a clear minimum at about 0.27GHz, however again slot 6 (and less noticeably its neighbors) become *noisier*. This noise that was correlated with the absence of a minimum and probably caused it (before the correction was carried out) now is responsible for the presence of too many minima. One of the curves contributing to this noise is seen in figure



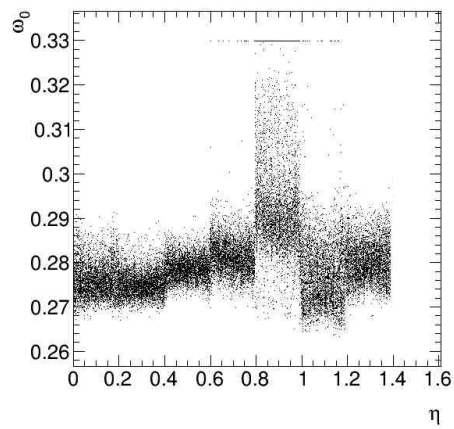
(a) F_{step}



(b) τ_{cal}



(c) τ_r



(d) ω_0

Figure 6.3: Values of various calibration constants for the front layer of the Side A of the Barrel of the LAr calorimeter

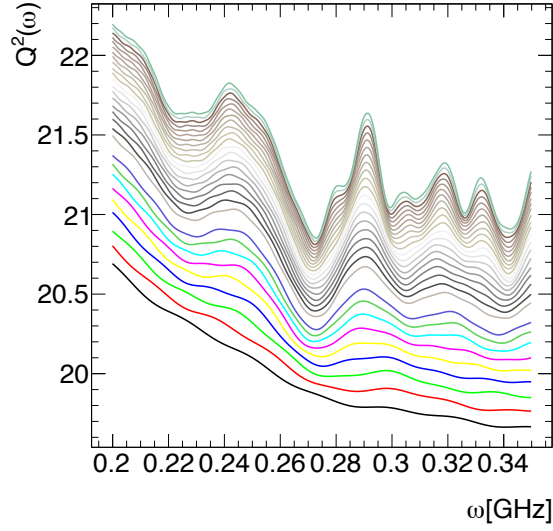
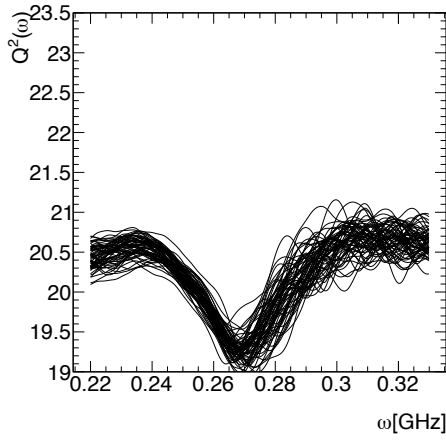


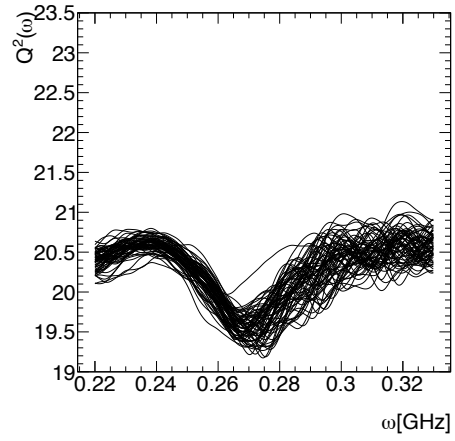
Figure 6.4: $Q^2(\omega)$ corresponding to many T_{tail} values (see (6.7)), increasing in steps of 20ns from 150ns, for $t_{start} = 20$ ns and where the uppermost curve corresponds to a sum with $t_{end} = 750$ ns.

6.6. Assuming, in cases like this, that the real value of ω_0 is not the lowest, but the one closest to the average in the slot considered and the adjacent ones, one could try to force the algorithm to choose the minimum at 0.27GHz for channels in the relevant parts of the detector; this would take down many of the values of ω_0 in slot 6 shown in figure 6.3.

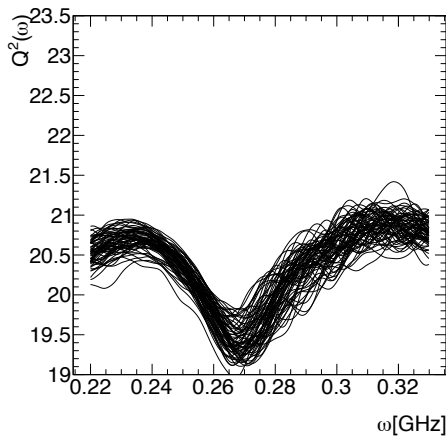
Figure 6.7 shows three distributions of ω_0 , in (a) the default (b) is the distribution after changing the interval of the sum. It clearly gets rid of the steps seen in (a) and also of the channels at 0.33GHz. Finally in (c) the algorithm has been modified to choose the minimum closest to 0.275GHz (based on the plots in figure 6.6). There are still channels not aligned with the distribution, but they are much fewer.



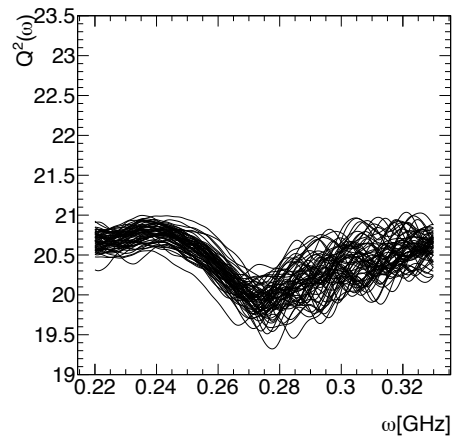
(a)



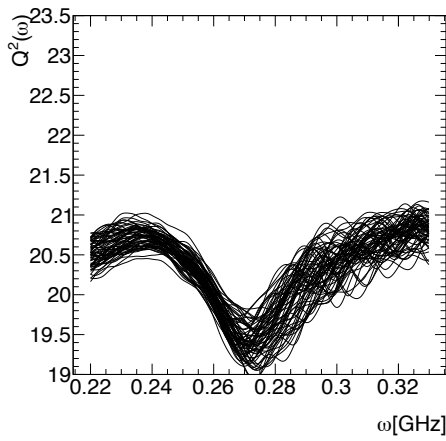
(b)



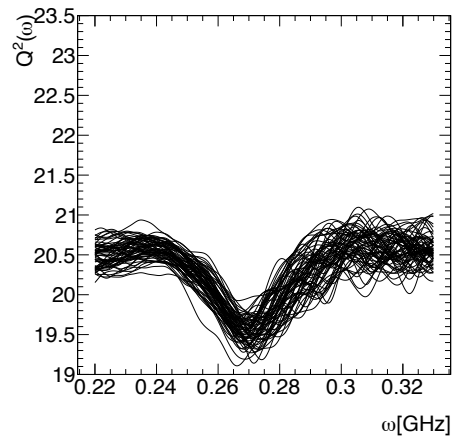
(c)



(d)



(e)



(f)

Figure 6.5: $Q^2(\omega)$ from slot 2 (a) to slot 6 (f) for Feedthrough=11 and $\phi = 2.3$ radians.

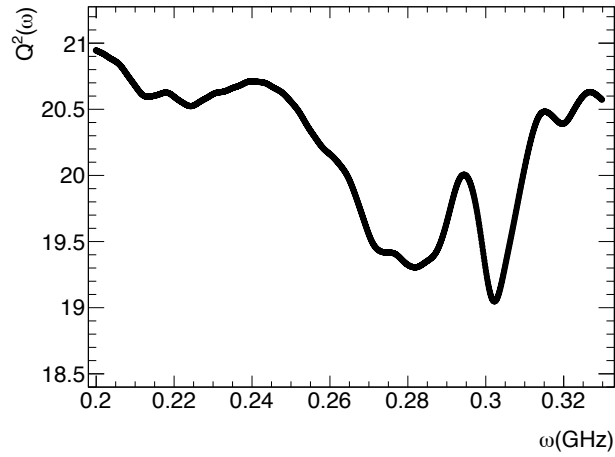
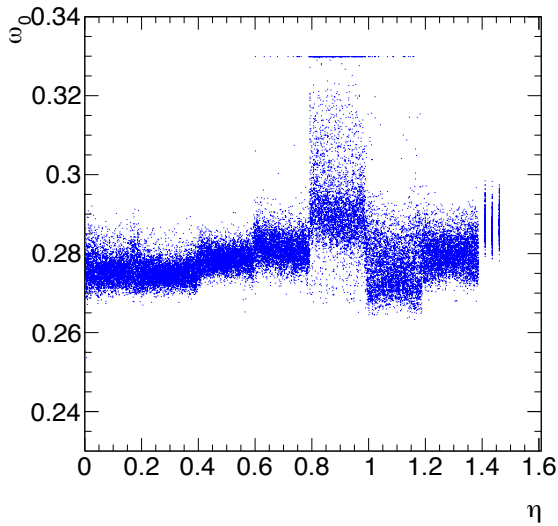
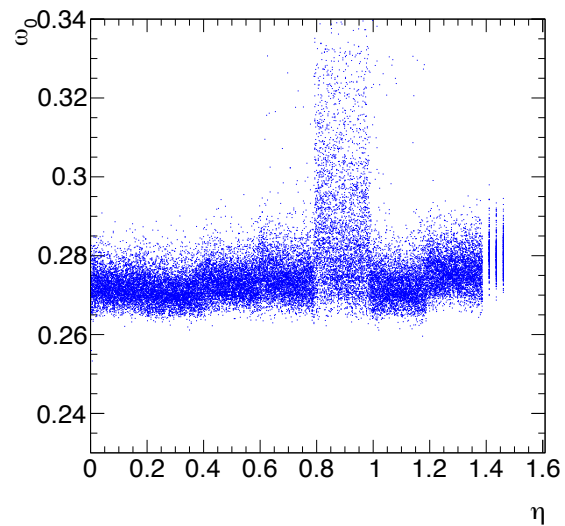


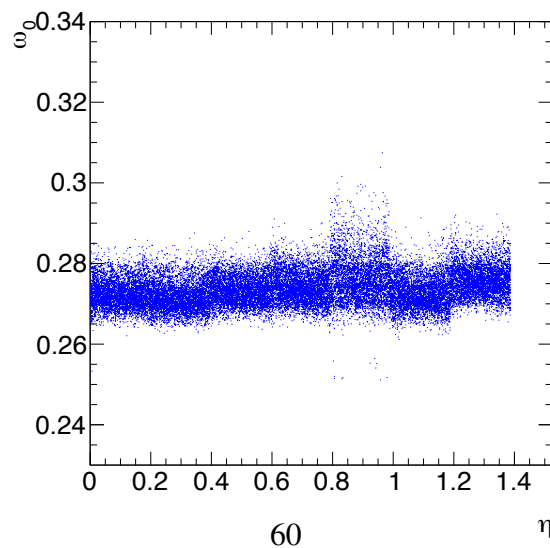
Figure 6.6: $Q^2(\omega)$ showing many minima.



(a) ω_0 using the default limits from approximately 20ns to 150ns.

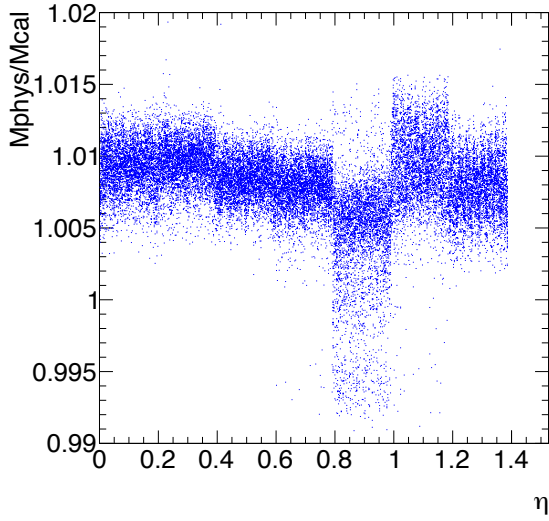


(b) ω_0 setting the limits from 20ns to 750ns.

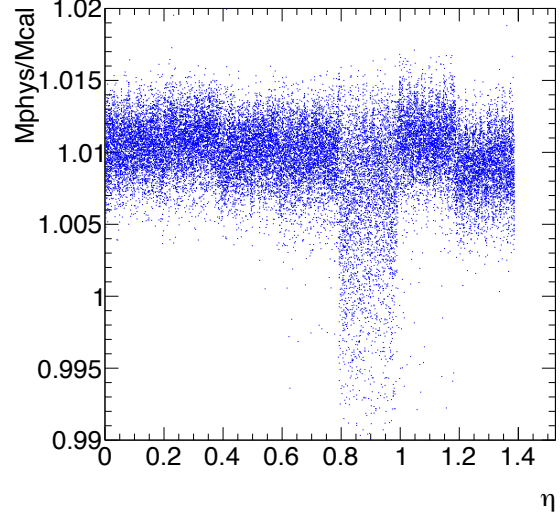


(c) Distribution of ω_0 after correcting the interval of the sum and associating its value to the

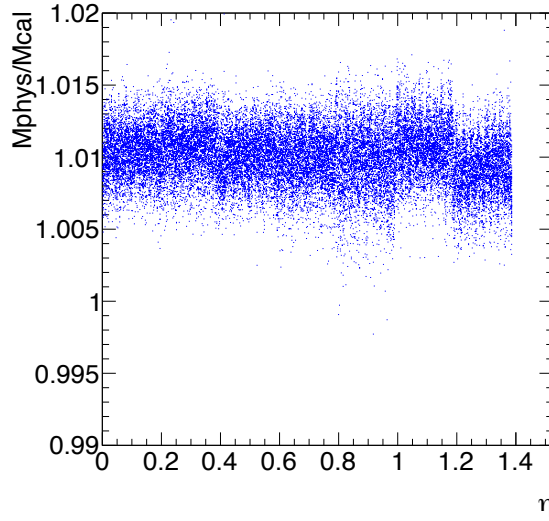
The corresponding plots for $M_{\text{phys}}/M_{\text{cal}}$ also change and they are shown in figure 6.8.



(a) Default $M_{\text{phys}}/M_{\text{cal}}$.



(b) $M_{\text{phys}}/M_{\text{cal}}$ using ω_0 from figure 6.7b.



(c) $M_{\text{phys}}/M_{\text{cal}}$ distribution using ω_0 from figure 6.7c.

Figure 6.8: Distributions of $M_{\text{phys}}/M_{\text{cal}}$

All the plots presented so far show calibrations run with the preamplifier working in high gain, which is the most frequently used during data taking (highly energetic particles are rarer). However the issues presented here also occur in medium and low gain, the corresponding plots are in figures C.1 and C.2 in the Appendix C.

In figure 6.9 one can see the $M_{\text{phys}}/M_{\text{cal}}$ distributions before and after the correction is made and also their ratio in function of η .

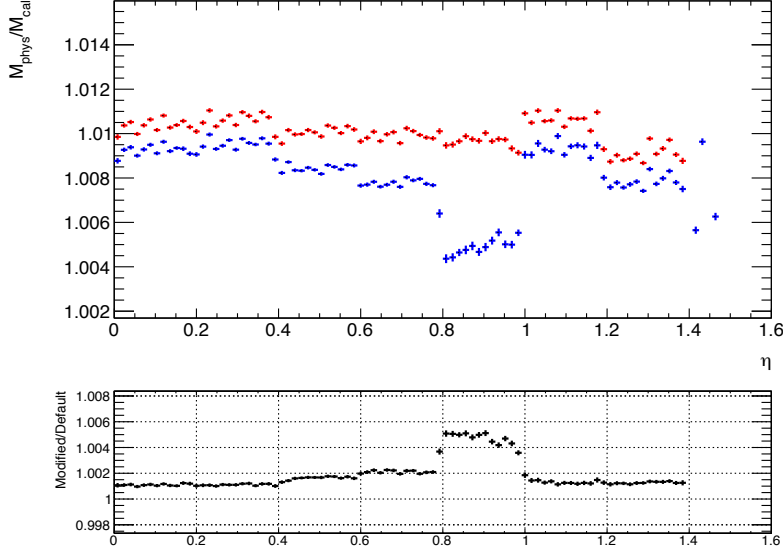


Figure 6.9: Distribution of $M_{\text{phys}}/M_{\text{cal}}$ before and after the corrections are applied in function of η .

6.4 Study of the Calibration Constants in the End Cap

In the outer wheel of the End Cap ω_0 and τ_r are extracted only for the middle layer, where most of the energy is deposited. In the front and back layers a default value is assumed for these constants in order to get $M_{\text{phys}}/M_{\text{cal}}$, therefore one is insensitive to the difference in the electric response of the cells and the calculated $M_{\text{phys}}/M_{\text{cal}}$ distribution is narrower than the real one.

In figure 6.10 one can see that for different intervals in η and for the front and back layers there is a minimum at around 0.27GHz. Figures 6.10 and 6.5 show the $Q^2(\omega)$ curves for the End-Cap and Barrel respectively, they have roughly the same shape, therefore it seems natural to choose the closest minimum to 0.27GHz as the location of ω_0 in the End-Cap too. Figure 6.11 shows the distributions of $M_{\text{phys}}/M_{\text{cal}}$ after extracting ω_0 in this way, it also shows the default values of $M_{\text{phys}}/M_{\text{cal}}$, the shapes do not change, but the distributions' RMS is larger.

Figure 6.12a shows $Q^2(\omega)$ for the middle layer and for a specific value of ϕ . Here the curves do not show any type of pattern and the extraction of ω_0 is by default carried out using frequency intervals that change with η . Figure 6.12b shows the $M_{\text{phys}}/M_{\text{cal}}$ distribution, obtained by constraining ω_0 to be in $0.23 < \omega_0 < 0.35$. The values of $M_{\text{phys}}/M_{\text{cal}}$ obtained in this way are compared between the front and middle layer in figure 6.13.

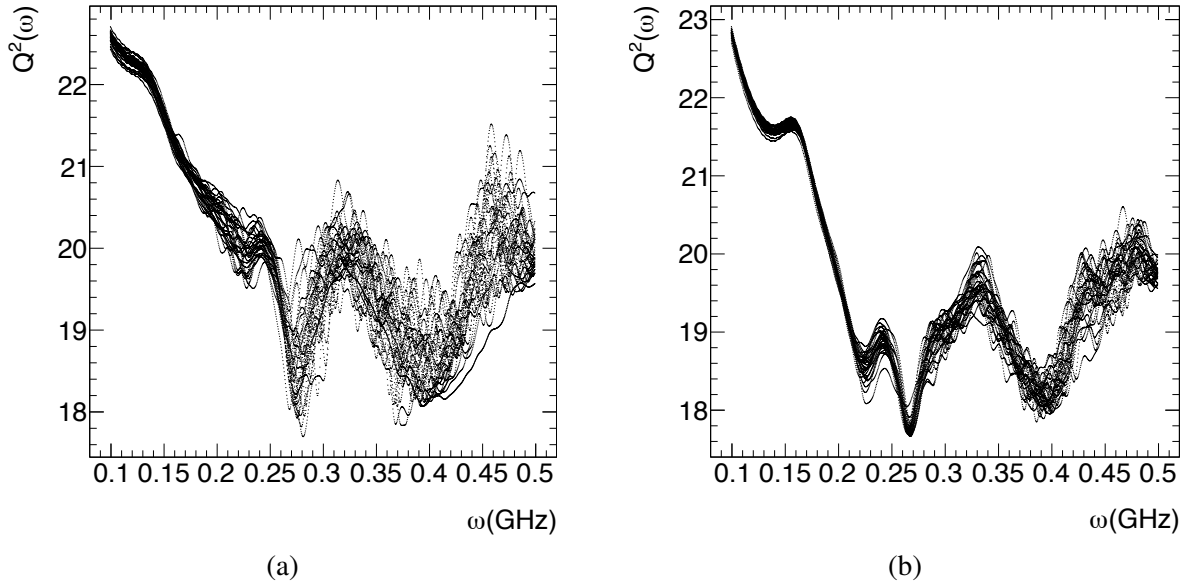


Figure 6.10: In (a) $Q^2(\omega)$ for channels in $2 < \eta < 2.4$, in the front layer of the End Cap. In (b) $Q^2(\omega)$ for channels in $1.4 < \eta < 2.5$ in the back layer of the End Cap.

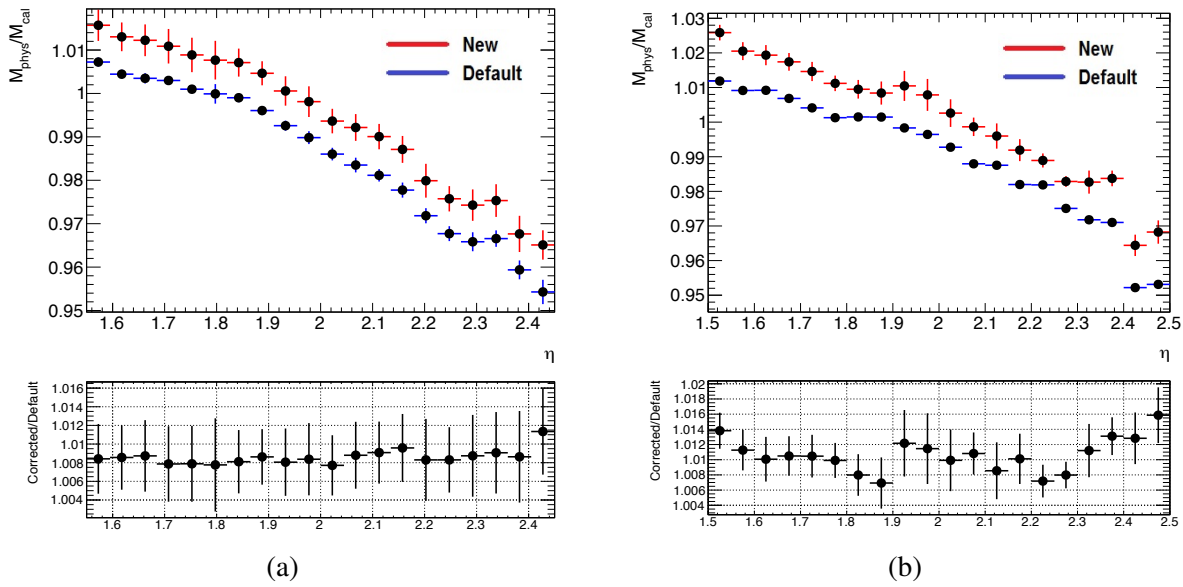


Figure 6.11: In (a) old and new values (setting $\omega_0 = 0.27\text{GHz}$) for $M_{\text{phys}}/M_{\text{cal}}$ for the front layer of the End Cap, Side A. In (b) the same values for the back layer

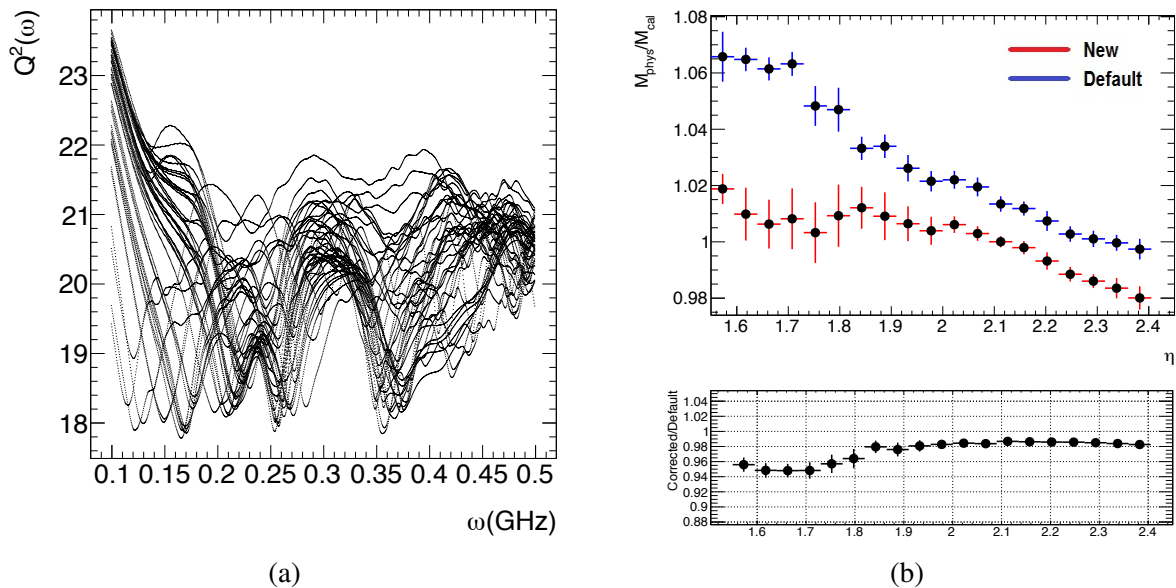


Figure 6.12: In (a) $Q^2(\omega)$ curves for the middle layer of the side A of the End Cap. In (b) Comparison of default and modified values of $M_{\text{phys}}/M_{\text{cal}}$ in the same part of the detector.

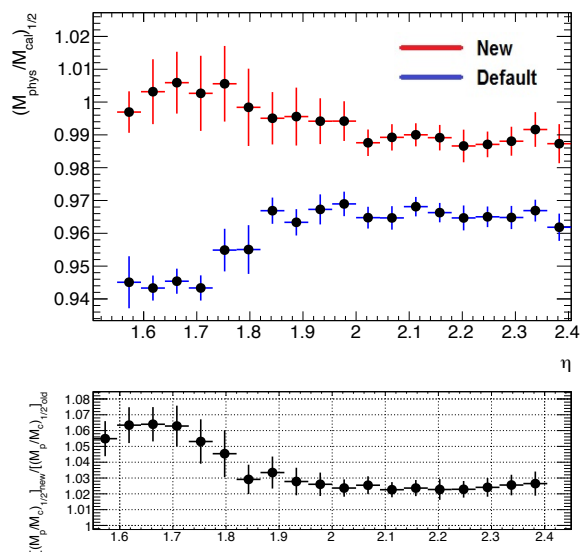


Figure 6.13: Ratio of $M_{\text{phys}}/M_{\text{cal}}$ between the front and middle layer. The subscript $1/2$ is used to symbolize the ratio between the quantities in layer 1 and layer 2.

6.5 Search for Outliers

6.5.1 Method

If for a given channel one measures the value of a calibration constant several times and if the conditions are stable, the constant's distribution should be gaussian. Also, if many channels in an homogeneous region of the detector are measured one expects to get a gaussian distribution. A channel is said to be an outlier if the mean of its distribution is beyond 2σ from the mean of the distribution of the channels in the homogeneous region to which it belongs, this is illustrated in 6.14.

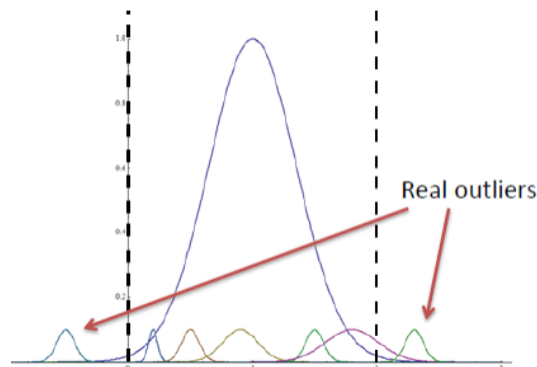


Figure 6.14: Representation of real outliers and channels within 2σ .

The issues in the barrel due to software or hardware problems were manifested in unusual values for the calibration constants. Therefore we decided to extend this approach and look for outliers.

For each row of channels, corresponding to a specific value of η , a set of constants is extracted, the mean and RMS of the distribution are calculated and the channels beyond 2σ are stored. These channels could be outliers because they are either special in some sense (i.e. miscalibrated) or because of a statistical fluctuation. To make sure that these channels are special we extracted a list of outliers from each campaign and *intersected* them as shown in figure 6.15. The optimal number of intersections to be taken should be the minimum that allows us to get rid of fake outliers and keep most of the true outliers. From figure 6.16, 13 seems to be a reasonable number of intersections.

If these channels were outliers because of statistical fluctuations, as more intersections are taken their number should decrease exponentially. Figure 6.16 shows the number of outliers in function of the number of intersections, they follow roughly the shape of an exponential plus a constant. It is reasonable to think that the exponential part is made of channels that are there due to statistical fluctuations. However the constant term could come from malfunctioning channels.

Channels that have a mean beyond 2σ might be found within 2σ too, due to statistical fluctuations, which is manifested in a slowly decreasing tail, that for an infinite number of intersections, or realistically just very large, should go to zero.

It will be assigned to the real outliers an effective probability P_i of been measured inside 2σ

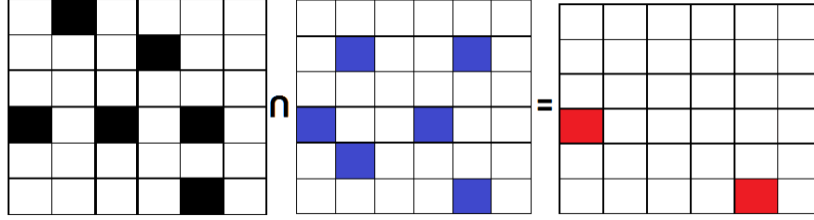


Figure 6.15: The black and the blue squares represent outliers in two different campaigns, the red channels are their intersection.

and to the non-outliers an effective probability P_o of been measured outside 2σ . Furthermore if in a given campaign one identifies O of the real outliers as such and I non-outliers as outliers, the number of fake outliers after k intersections is $I \cdot P_o^k$ and the number of outliers that are measured as such is $O \cdot (1 - P_i) \cdot k$. So the number of channels measured as outliers after k intersections is:

$$N(k) = IP_o^k + O(1 - P_i)^k = Ie^{-k \cdot \ln P_o^{-1}} + Oe^{-k \cdot \ln(1 - P_i)^{-1}} \quad (6.8)$$

which is a superposition of two exponentials, one that decreases very rapidly and another that does it very slowly. This is clearly an approximation, mainly because P_i and P_o are assumed to be constants.

6.5.2 Results

Figure 6.16 shows the fit, to a superposition of two exponentials for the barrel and the End-Cap in the side A, with the values of the fitting parameters also shown. The errors are the square roots of the bin contents. The fit with two exponentials follows almost perfectly the data for the End Cap and reasonably well for the Barrel, the coefficients I and O are respectively the number of fake outliers and real outliers measured in one campaign. I should be equal to the number of channels with means inside 2σ that were measured outside 2σ and O is the number of outliers that remained outside 2σ . Consequently for the End Cap the number of true outliers can be estimated as $O/(1 - P_i) \approx 272$. Given that the probability for a channel to be outside 2σ is 0.046, the number of non-outliers should be $I/0.046 \approx 22075$. The sum of this and 272 should be the total number of channels in the side A of the End-Cap, around 32 000, however it is not. The most likely reason is that there are channels that rarely go outside 2σ and therefore do not affect the exponential fit and are not counted. This exponential fit reveals the existence of outliers and gives us an idea of their number.

Figure 6.17 shows the same outliers in the $\eta - \phi$ plane. The black circles are outliers only in $M_{\text{phys}}/M_{\text{cal}}$, the constant one is really interested in. The other colors represent outliers in $M_{\text{phys}}/M_{\text{cal}}$ and at the same time a specific constant on which $M_{\text{phys}}/M_{\text{cal}}$ depends.

It is reasonable to think that if a constant on which $M_{\text{phys}}/M_{\text{cal}}$ depends is beyond 2σ that might take $M_{\text{phys}}/M_{\text{cal}}$ also beyond 2σ . In the cases where only $M_{\text{phys}}/M_{\text{cal}}$ is an outlier, more than one of the other constants might be close to 2σ and their combined contributions might take $M_{\text{phys}}/M_{\text{cal}}$ beyond 2σ .

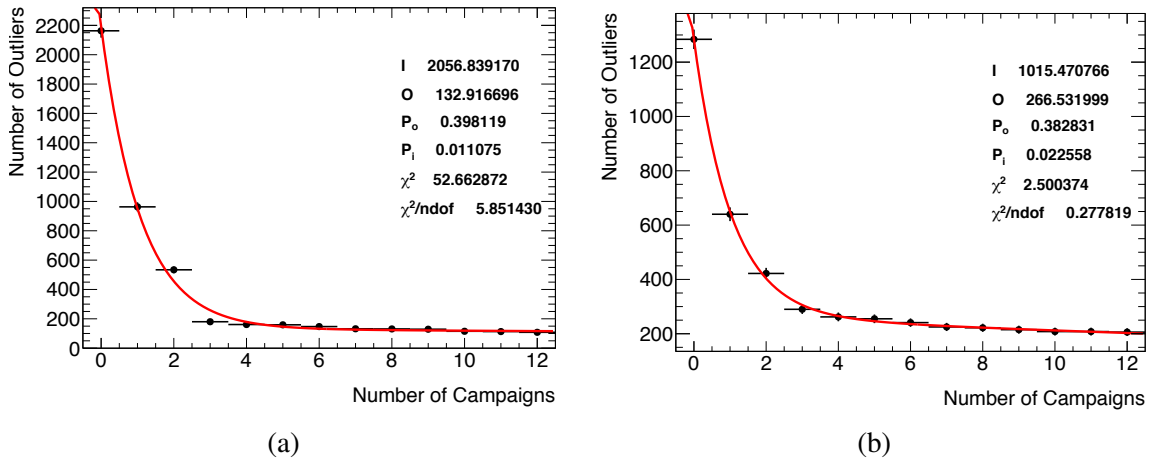
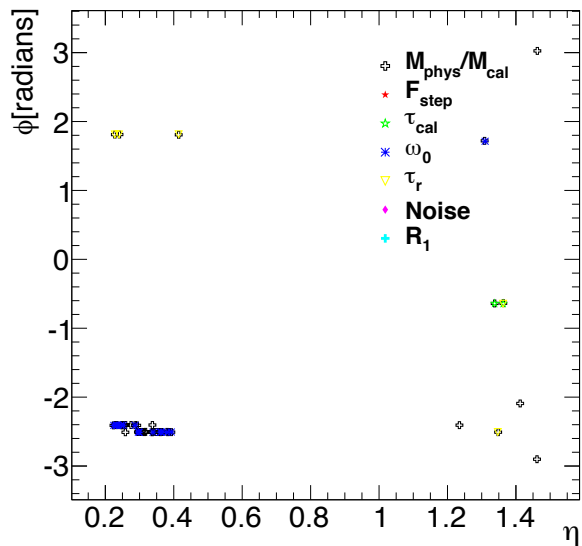
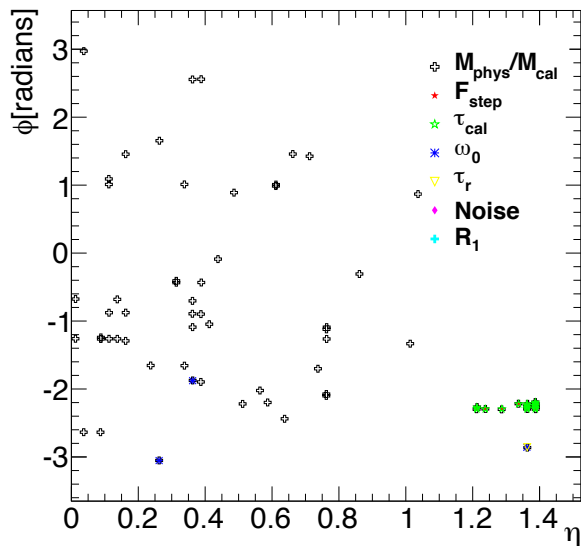


Figure 6.16: Intersection of outliers for 13 campaigns in the Barrel in (a) and in the End Cap in (b) fitted to a superposition of two exponentials.

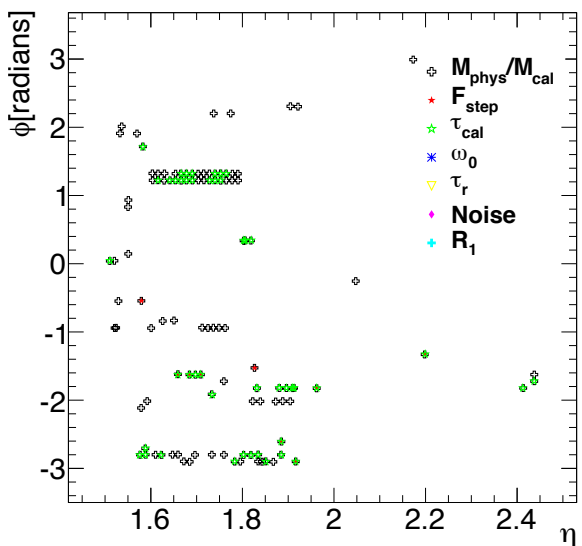
The behavior of ω_0 in the Barrel, treated in section 6.3.2, was related to slot 6 in both sides A and C, which strongly suggested a hardware problem associated with the geometry of the detector. Apart from isolated channels one can recognize clusters in slot 3 for the strips and slot 14 for the middle layer of the barrel. The End Cap shows also outliers localized in specific feedthroughs. This clearly implies that their *outlierness* is related to the behavior of specific motherboards and they must have a physical origin.



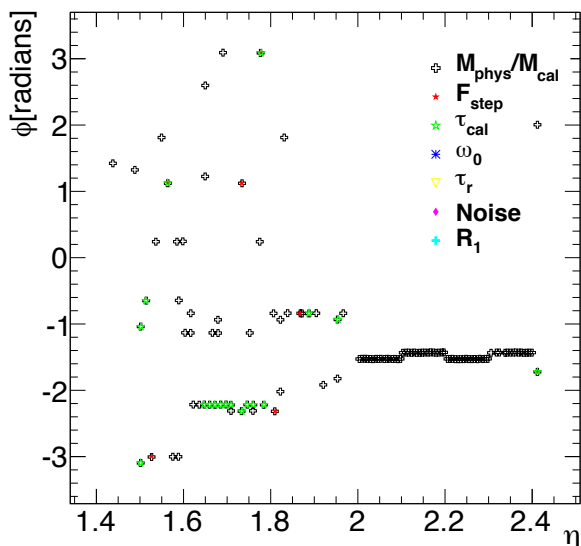
(a) Front layer, side A, Barrel.



(b) Middle layer, side A, Barrel.



(c) Front layer, side A, End-Cap.



(d) Middle layer, side A, End-Cap.

Figure 6.17: Plots of outlier cells in a given calibration constant.

Chapter 7

Conclusions

7.1 Graviton Search

A search for heavy resonances decaying into a WW , WZ and ZZ pair of bosons was carried out. The search used 20.3fb^{-1} of ATLAS data collected in 2012. The most effective discriminants between QCD and signal were found to be the jet mass and the difference in rapidity between the two jets. The largest source of uncertainty is related with the efficiency of the n_{trk} cut, which was estimated as 17%. Despite the large signal efficiency and background rejection achieved the analysis was only able to rule out W' masses in the 1.3 – 1.5TeV mass range and no mass hypothesis for the RS model with SM fields in the brane.

However an excess was found at 2TeV, its local significance was found to be almost 3.4σ and after taking into account the LEE the global significance obtained was 2.5σ . The excess was seen in all the channels studied, but the most significant one corresponds to the WZ channel. It is therefore not possible to rule out at 95%CL the existence of a W' or a graviton at 2TeV. More data is required to either rule out the excess as a statistical fluctuation or confirm the existence of new physics.

If the excess observed in data is signal then the signal strength associated to the graviton model is several hundreds. This means that the excess is unlikely to be caused by a graviton. As seen in figures 5.2a, 5.2b and 5.2c the width of the excess does agree with the width of the signal peak, specially taking into account that the width is allowed to *float* within the p_T resolution. On the other hand the W' branching ratio to a WZ pair is negligible in comparison to the branching ratio to a $q\bar{q}'$ pair. Therefore if the excess were due to a W' boson, its likely that It would have been seen in other channels too, which is not the case. So far there is no clear candidate for a model that explains the excess observed.

7.2 Study of the Calibration Constants of the Electromagnetic Calorimeter's Cells

The calibration constants of the electromagnetic calorimeter's barrel at high gain were studied and a discontinuity was found in $M_{\text{phys}}/M_{\text{cal}}$ in slot 8 in both the A and the C sides. The origin of this discontinuity was traced to the way how the frequency of resonance of the cells, ω_0 , was extracted. The bug in the code responsible should be fixed. Furthermore a way of modifying the algorithm used to extract this quantity was suggested and it was proved that it improves significantly the discontinuity observed.

Also a scan of the calibration constants was carried out. The values were evaluated across many calibration campaigns and a list of channels with calibration constants far from the mean was obtained, their distribution suggests a hardware related issue. There is no conclusion yet about the nature of their values and further studies are needed.

Bibliography

- [1] Ilia Gogoladze and Cosmin Macesanu. Precision electroweak constraints on universal extra dimensions revisited. *Phys.Rev.D*, 74:093012, 2006.
- [2] C. Hoyle, U. Schmidt, B. Heckel, E Adelberger, J. Gundlach, D. Kapner, and H. Swanson. Sub-millimeter tests of the gravitational inverse-square law: A search for "large" extra dimensions. *Phys.Rev.Lett.*, 86:1418–1421, 2001.
- [3] Nima Arkani-Hamed, Savas Dimopoulos, and Gia Dvali. The hierarchy problem and new dimensions at a millimeter. *Phys.Lett.B*, 429:263–272, 1998.
- [4] Lisa Randall and Raman Sundrum. A large mass hierarchy from a small extra dimension. *Phys.Rev.Lett*, 83:3370–3373, 1999.
- [5] H. Davoudiasl, J Hewett, and Rizzo T. Phenomenology of the randall-sundrum gauge hierarchy model. *Phys.Rev.Lett*, 84:2080–2083, 2000.
- [6] Kaustubh Agashe, Hooman Davoudiasl, Gilad Perez, and Amarjit Soni. Warped gravitons at the lhc and beyond. *Phys.Rev.D*, 76:036006, 2007.
- [7] R Kleiss and W Stirling. Standard model expectations for large transverse momentum w+two-jet events at the cern collider. *Phys.Lett*, B180:170, 1986.
- [8] Guido Altarelli, Barbara Mele, and M Ruiz-Alba. Searching for new heavy vector bosons in pp colliders. *Zeitschrift fur physik C*, 45:109–121, 1989.
- [9] The ATLAS collaboration. Performance of the atlas inner detector track and vertex reconstruction in the high pile-up lhc environment. ATLAS-CONF-2012-042, 2012.
- [10] Wolfgang Waltenverger, Rudolf Fruhwirth, and Pascal Wanlaer. Adaptive vertex fitting. *J. Phys. G: Nucl. Part. Phys.*, 34:N343, 2007.
- [11] The ATLAS Collaboration. Luminosity determination in pp collisions at sqrt(s)=7tev using the atlas detector at the lhc. *Eur.Phys.J*, 71:1630, 2011.
- [12] D Belohrad, J Gras, L Jensen, et al. Commissioning of the first performance of the lhc beam current measurement systems. <http://accelconf.web.cern.ch/AccelConf/IPAC10/papers/mope059.pdf>, 2010.

- [13] The ATLAS collaboration. Luminosity determination using the atlas detector. ATL-ATLAS-CONF-2010-060, 2010.
- [14] The ATLAS collaboration. Atlas forward detectors for measurement of elastic scattering and luminosity. <http://cdsweb.cern.ch/record/1095847>, 2008.
- [15] Oleg Antipin and Tuomas Hapola. <http://cp3-origins.dk/research/units/ed-tools>.
- [16] Alexander Belyaev, Neil Christensen, and Pukhov Alexander. Calchep 3.4 for collider physics within and beyond the standard model. *Comput.Phys.Commun.*, 184:1729–1769, 2013.
- [17] Johan Alwall, Michel Herquet, Fabio Maltoni, Olivier Mattelaer, and Tim Stelzer. Madgraph5:going beyond. *JHEP*, 128, 2011.
- [18] Torbjørn Sjöstrand, Stephen Mrenna, and Peter Skands. A brief introduction to pythia 8.1. *Comput.Phys.Commun.*, 178:852–867, 2008.
- [19] The ATLAS Collaboration. The atlas simulation infrastructure. *Eur.Phys.J. C*, 70:823–874, 2010.
- [20] Matteo Cacciari, Gavin Salam, and Gregory Soyez. The catchment area of jets. *JHEP*, 0804:005, 2008.
- [21] Matteo Cacciari, Gavin Salam, and Gregory Soyez. The anti-k_t jet clustering algorithm. *JHEP*, 0804:063, 2008.
- [22] M. Wobisch and T Wengler. Hadronization corrections to jet cross sections in deep-inelastic scattering. <http://arxiv.org/abs/hep-ph/9907280v1>, 1999.
- [23] Jonathan Butterworth, Adam Davison, Mathieu Rubin, and Gavin Salam. Jet substructure as a new higgs search channel at the lhc. *Phys.Rev.Lett.*, 100:242001, 2008.
- [24] David Krohn, Jesse Thaler, and Lian-Tao Wang. Jet trimming. *JHEP*, 1002:084, 2010.
- [25] The ATLAS Collaboration. Performance of jet substructure techniques for large-r jets in proton-proton collisions at $\sqrt{s}=7\text{TeV}$ using the atlas detector. *JHEP*, 09:076, 2013.
- [26] Glen Cowan, Kyle Cranmer, Eilam Gross, and Ofer Vitells. Asymptotic formulae for likelihood-based tests of new physics. *Eur.Phys.J. C*, 71:1554, 2011.
- [27] Lorenzo Moneta, Kevin Belasco, Kyle Cranmer, Sven Kreiss, Alfio Lazzaro, Danilo Piparo, et al. The roostats project. <http://arxiv.org/abs/1009.1003v2>, 2011.
- [28] Wouter Verkerke and David Kirkby. The roofit toolkit for data modeling. <http://arxiv.org/abs/physics/0306116>, 2003.
- [29] Gregory Schott. Roostats for searches. <http://arxiv.org/abs/1203.1547>, 2012.

- [30] Eilam Gross and Ofer Vitells. Trial factors for the look elsewhere effect in high energy physics. *Eur.Phys.J, C70:525–530*, 2010.
- [31] D. Banfi, M. Delmastro, and M. Fanti. Cell response equalization of the atlas electromagnetic calorimeter without the direct knowledge of the ionization signals. *JINST*, 1:P08001, 2006.
- [32] Marco Delmastro. personal communication, 2013.
- [33] Martin Alexa et al. Computation and validation of the electronic calibration constants for the electromagnetic calorimeter. *ATL-LARG-PUB-2006-003*, 2006.
- [34] Ahmed Aly Abdelalim. Study on the impact of cross-talk in the atlas electromagnetic calorimeter on the signal prediction in the strip layer. Master Thesis, 2008. University of Geneva.
- [35] R.L. Chase et al. A fast monolithic shaper for the atlas e.m. calorimeter. *ATLAS-LARG-INT-1995-10*, 1995.

Appendix A

Monte Carlo, Data and Physics Objects

A.1 Background

Tables [A.1](#) and [A.2](#) provide details about the background samples used in the analysis in PYTHIA and POWHEG respectively.

Slice	p_T range (TeV)	σ (fb)	n_{evt} (10^3)
J3	0.2-0.5	544000000	6000
J4	0.5-1.0	6450000	6000
J5	1.0-1.5	39700	1500
J6	1.5-2.0	416	1500
J7	> 2.0	40.6	1500

Table A.1: Cross-sections of different p_T slices for the PYTHIA dijet QCD MC.

Slice	p_T range (TeV)	σ (fb)	n_{evt} (10^3)
J3	0.2-0.5	1640000000	1500
J4	0.5-1.0	7570000	1500
J5	1.0-1.5	48900	1400
J6	1.5-2.0	2800	1400
J7	> 2.0	26.2	1400

Table A.2: Cross-sections of different p_T slices for the POWHEG dijet QCD MC.

Table [A.3](#) provides details about the $W + jets$ and $Z + jets$ montecarlo samples used.

Slice	p_T range (TeV)	σ (fb)	n_{evt} (10^3)
W	0.2-0.35	30640	500
	> 0.35	2459	200
Z	0.2-0.35	13290	250
	> 0.35	1069	100

Table A.3: Cross-sections of different p_T slices for the PYTHIA $W + jets$ and $Z + jets$ samples.

A.2 Signal

Each graviton mass point was generated with 20000 events. Table A.4 shows the cross section and widths for different mass points.

Mass	$\sigma \cdot \text{BR}$	Γ	$\sigma \cdot \text{BR}$	Γ
	$G \rightarrow WW$	$G \rightarrow WW$	$G \rightarrow ZZ$	$G \rightarrow ZZ$
(TeV)	(fb)	(GeV)	(fb)	(GeV)
1300	1.5887	69	0.37	76
1400	0.9081	76	0.2	83
1500	0.5318	83	0.12	89
1600	0.3173	90	0.071	96
1700	0.1924	96	0.043	103
1800	0.1188	103	0.027	109
1900	0.0744	109	0.017	116
2000	0.047	116	0.01	123
2100	0.03	123	0.0067	129
2200	0.0194	129	0.0043	136
2300	0.0126	136	0.0028	142
2400	0.0083	142	0.0018	149
2500	0.0055	149	0.0012	155
2600	0.0036	155	0.00092	161
2700	0.0024	161	0.00054	168
2800	0.0016	168	0.00037	174
2900	0.0011	174	0.00025	181
3000	0.0008	180	0.00017	187

Table A.4: Cross-sections times branching ratios and widths for different mass points for a graviton decaying in the WW and ZZ channels.

Appendix B

Event Selection

B.1 Filtered Jet Mass Cut Optimization

In table B.1 are shown the different p_T slices in which the mass window optimization was carried out.

Mass (GeV)	Lower p_T (GeV)	Higher p_T (GeV)
1200	476.432	676.432
1300	525.167	725.167
1400	571.135	776.138
1500	611.206	827.973
1600	653.422	878.418
1700	697.679	932.786
1800	737.451	981.067
1900	779.07	1037
2000	818.779	1088.44
2100	864.163	1140.1
2200	905.594	1191.34
2300	947.191	1246.21
2400	987.863	1294.42
2500	1032.39	1344.78
2600	1075.98	1394.31
2700	1110.31	1445.23
2800	1149.08	1497.72
2900	1195.37	1548.93
3000	1219.66	1582.14

Table B.1: Cross-sections of different p_T slices for the PYTHIA $W + jets$ MC.

Table B.2 lists the different mass windows obtained after optimizing for each mass point with an EGM W' monte-carlo sample.

Mass (TeV)	Half Window (GeV)
1200	10
1400	10
1600	12
1800	12
2000	14
2200	14
2400	14
2600	14
2800	14
3000	15
Average	12.9

Table B.2: Optimal values for the half window size for a vector boson, deduced from many W' signal samples.

Figures B.1a and B.1b show the significance gain in function of the mass window half width for three mass points corresponding to the W' signal sample. Similar results were obtained for the graviton signals.

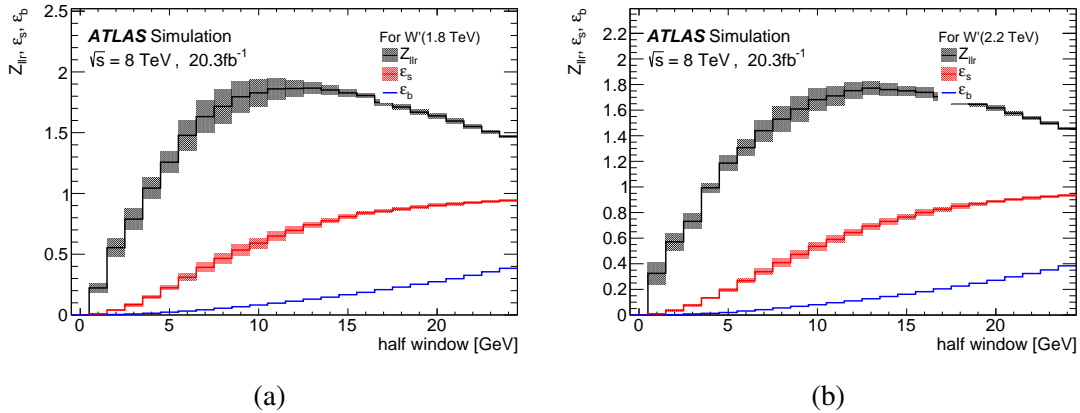


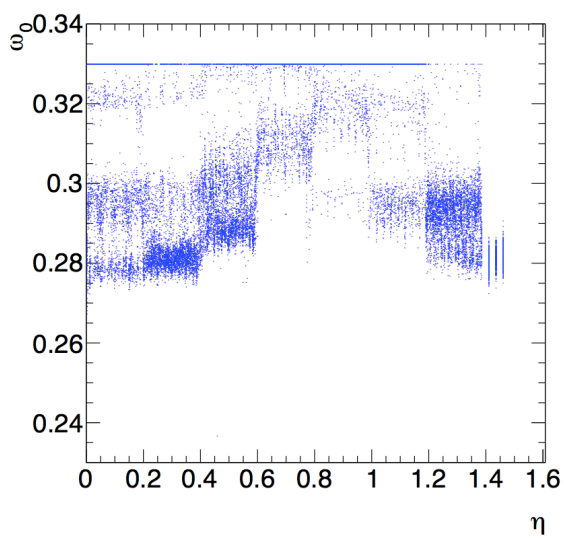
Figure B.1: (a), (b) show the background and signal efficiencies as well as the gain in significance with respect to the $60 < m_{JJ} < 110\text{GeV}$ mass window for the 1.8TeV and 2.2TeV W' mass points.

Appendix C

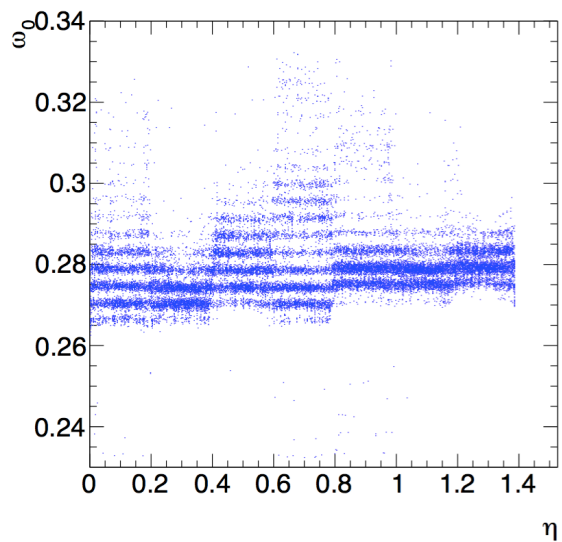
Electromagnetic Calibration

Figure C.1a shows the distribution of ω_0 for the barrel, side A, for low gain. The bug that was seen in chapter 6 and that was responsible for a discontinuity in slot 8, here seems to have the same effect in the first six slots. Figure C.1c shows the corresponding values of $M_{\text{phys}}/M_{\text{cal}}$. After applying the same correction used in chapter 6 one obtains the ω_0 distribution shown in figure C.1b. When using these values one gets the $M_{\text{phys}}/M_{\text{cal}}$ distribution in figure C.1d. Despite the distributions after the correction have some non-uniform appearance, there is a clear improvement.

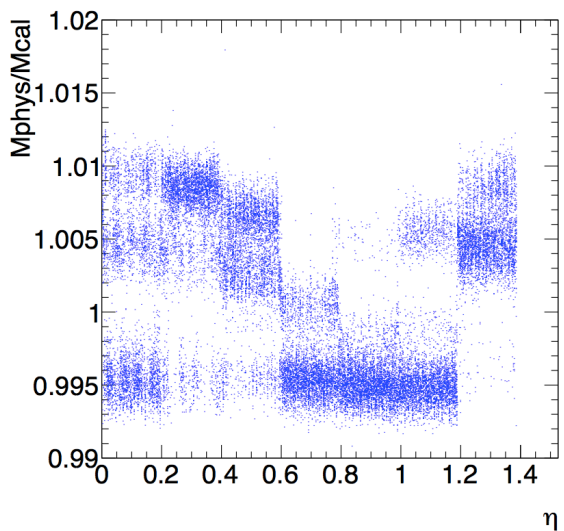
Figures C.2 show the same distributions but when the amplifiers work in medium gain. The channels for which ω_0 is not well calculated are also present in C.2a, after the correction, the distribution is more uniform in C.2b. The corresponding $M_{\text{phys}}/M_{\text{cal}}$ are shown in C.2c and C.2d.



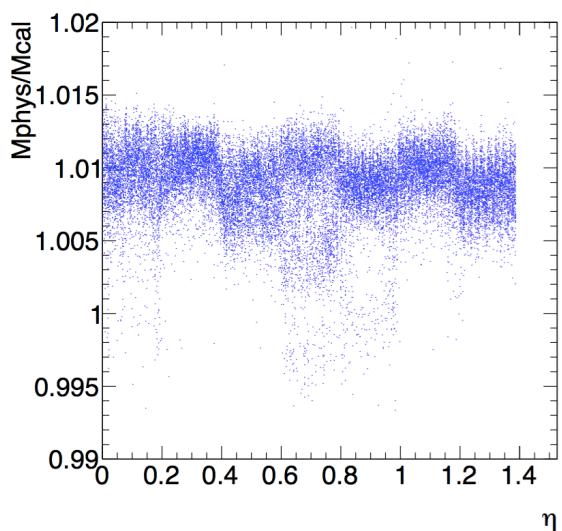
(a)



(b)

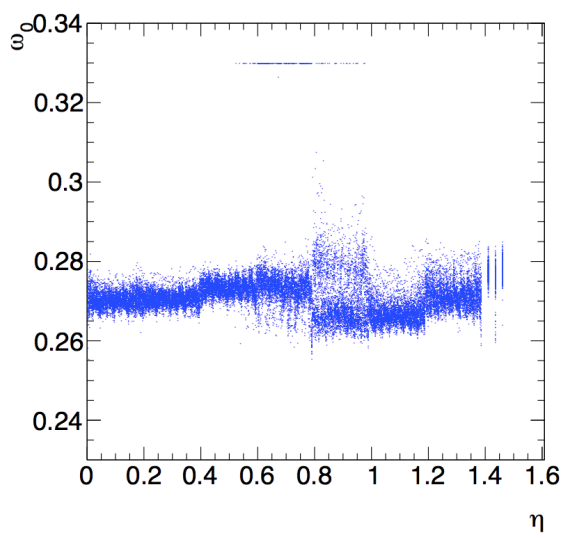


(c)

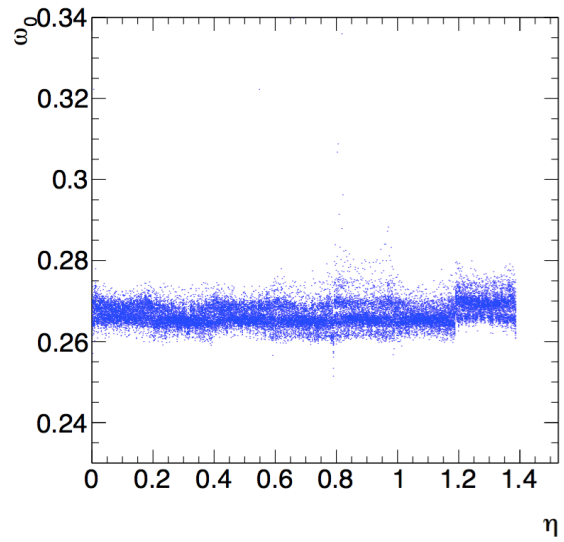


(d)

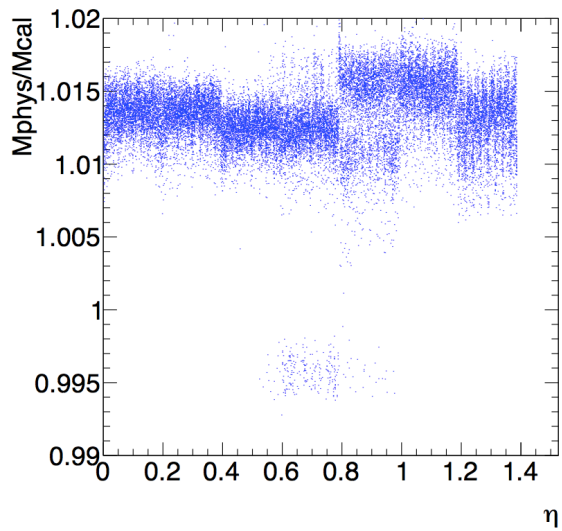
Figure C.1: Figures (a) and (b) show the ω_0 distributions for the side A of the barrel for low gain, before and after the correction respectively. Figures (c) and (d) show the corresponding distributions for $M_{\text{phys}}/M_{\text{cal}}$.



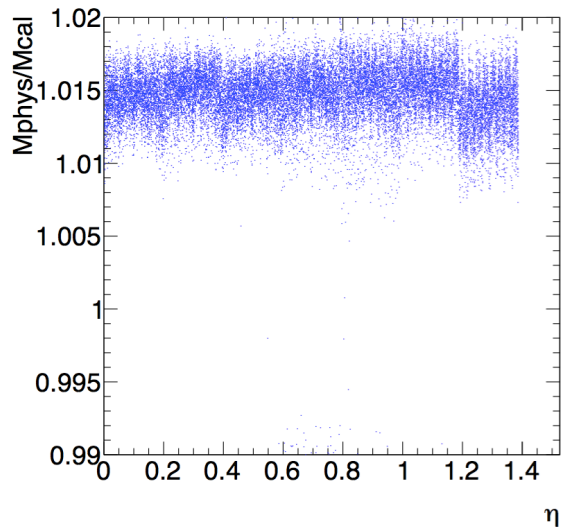
(a)



(b)



(c)



(d)

Figure C.2: Figures (a) and (b) show the ω_0 distributions for the side A of the barrel for medium gain, before and after the correction respectively. Figures (c) and (d) show the corresponding distributions for M_{phys}/M_{cal} .